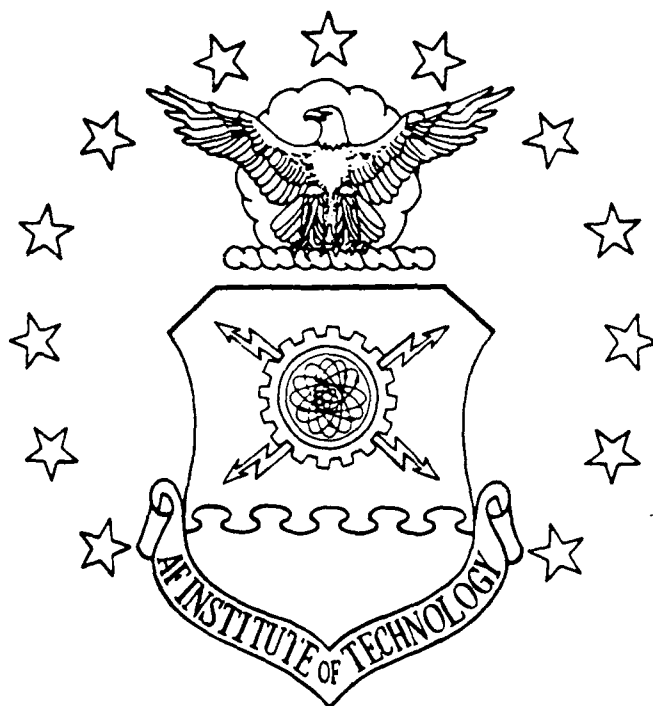DTIC
S ELECTE
DEC 14 1989
B D

MULTIPLEXED ROBOTIC TACTILE SENSOR
FABRICATED FROM
POLYVINYLIDENE FLUORIDE FILM

THESIS

Douglas G. Ford
Captain, USAF

AFIT/GE/ENG/89D-13

DEPARTMENT OF THE AIR FORCE

AIR UNIVERSITY

AIR FORCE INSTITUTE OF TECHNOLOGY

Wright-Patterson Air Force Base, Ohio

89 12 14 031

MULTIPLEXED ROBOTIC TACTILE SENSOR
FABRICATED FROM
POLYVINYLIDENE FLUORIDE FILM

THESIS

Douglas G. Ford
Captain, USAF

AFIT/GE/ENG/89D-13

DTIC
ELECTE
DEC 14 1989
S
B
D

AFIT/GE/ENG/89D-13

MULTIPLEXED ROBOTIC TACTILE SENSOR

FABRICATED FROM POLYVINYLIDENE FLUORIDE FILM

THESIS

Presented to the Faculty of the School of Engineering

of the Air Force Institute of Technology

Air University

In Partial Fulfillment of the

Requirements for the Degree of

Master of Science in Electrical Engineering

Douglas G. Ford, B.S.

Captain, USAF

December 1989

Acknowledgements

This project has been one of the most challenging technical ordeals in my Air Force career. Proper credit must first be extended to my advisor, Maj Edward S. Kolesar. His patience, technical wisdom, and impeccable writing skills have significantly enhanced the quality of this work. I also wish to thank the other members of my thesis committee, Colonel Irving LeBlanc, Colonel Charles Hatsell, Captain Keith Jones, and Captain Billy Hodges. A personal thanks is extended to Mr. Donald Smith and Mr. William Trop for their daily assistance with the equipment in the Cooperative Electronics Laboratory. Finally, I wish to thank Mr. Larry Callahan from the Wright Research and Development Center for his wire bonding assistance.

ii

Table of Contents

List of Figures

ix

List of Tables

Abstract

This research effort involved the design, fabrication
and evaluation of a multiplexed robotic tactile sensor
fabricated from polyvinylidene fluoride (PVDF) film. A
16x16 electrode array was designed, each electrode
encompassing a 250 μm x 250 μm square area, separated by a
distance of 150 μm. A resident analog multiplexer was
designed to assist in the acquisition of electrical signals
from the array. Inherent within the multiplexer were analog
transmission gates which provided a bidirectional flow of
charge to each electrode. This provided a means of
initializing the bias state of the PVDF film prior to the
application of a load.

Fundamental difficulties associated with coupling the
PVDF film to the electrode array (and the analog
transmission gates) prevented the successful fabrication of
a functioning tactile sensor. A previously designed 5x5
electrode array sensor was modified with external TTL
multiplexing circuitry. Characterization of the IC,
configured with a 25 μm thick PVDF film, was accomplished
using a circle, toroid, rectangle, and a hexagon over the
load range of 3 g to 100 g. Final results included the

development of an elementary pattern recognition algorithm.
Recommendations for solving the obstacles faced in this
research effort are discussed in the final chapter.

MULTIPLEXED ROBOTIC TACTILE SENSOR FABRICATED
FROM POLYVINYLIDENE FLUORIDE FILM

I. INTRODUCTION

Background

Robotic technology has matured to the point where pressure sensors positioned on a robotic extensor need to possess the tactile resolution of a human fingertip, reported to span 0.8 mm to 3.0 mm [1]. Based on a previous thesis by Captain Rocky Reston, it was shown that a robotic tactile sensor can be fabricated using a planar array of MOSFET amplifiers coupled to a piezoelectric polyvinylidene fluoride (PVDF) film [2]. This "first generation" tactile sensor used a 5x5 array of MOSFET linear amplifiers, fabricated in a host silicon wafer, to amplify the voltages generated in the PVDF film in response to an applied force (load). A three-dimensional plot of the discrete sensor element amplified voltages were used to represent the spatial distribution of the forces (loads) contacting the surface of the PVDF film.

When an external force (load) was applied to the 5x5 array discussed above, the coarse representation of a real

world object (toroid) could be discerned. To obtain a higher degree of spatial resolution, the array needs to be on the order of 16x16 elements confined to the same peripheral dimensions as the original sensor design (6 mm x 6 mm).

Problem Statement

This thesis entails the design, fabrication, and performance characterization of a multiplexed 16x16 MOSFET linear amplifier array that was coupled to a PVDF piezoelectric film patch to realize a robotic tactile sensor.

Scope

This effort is limited to the design, fabrication, and performance characterization of the 16x16 MOSFET tactile sensor array. The critical parameters include:

i)   coupling the PVDF film to the MOSFET amplifier array,

ii) establishing the electrode size and spacings, as characterized by measuring the degree of coupling (electrical and mechanical) between nearest-neighbor array elements when a given load is applied to a reference sensor element, and

iii) determining the linearity and time-invariant behavior of the MOSFET amplifier's DC operating point, which can be observed to result from the accumulation of charge on the gate electrodes [2].

The tactile sensor is fabricated from 25 μm, 40 μm, and 52 μm thick PVDF films. PVDF films thinner than 25 μm are too fragile to work with, while films thicker than 52 μm thick do not readily conform to the irregular surface topography of an integrated circuit (IC) [2:4-7]. Coupling the PVDF film to the array elements is accomplished with an electrically insulating adhesive, which provide a strong physical bond, yet minimizes charge transfer between the MOSFET amplifier array elements, as described below.

Assumptions

To establish an initial set of design constraints, three basic assumptions were made:

1. Electric field fringing effects between the electrodes in the sensor matrix are negligible. This can be verified experimentally by measuring the "coupling" between-nearest neighbor sensor elements.

2. The adhesive thickness, which bonds the PVDF film
    to the IC, is sufficiently thin such that the
    electrical effects of the PVDF film dominates.

3. IC's received from MOSIS function correctly,
    assuming a correct design. The implemented design
    incorporates a modular design philosophy; that is,
    should one circuit subsection fail (for instance, a
    Row Select Decoder), the entire experimental
    portion of the research could still be accomplished
    after replacing the flawed area with external
    circuitry.

Approach

The basic approach for this research effort consists
of the design, fabrication, and performance evaluation of a
piezoelectric tactile sensor utilizing a polyvinylidene
fluoride film (PVDF).

Design. The overall IC circuit design is shown in
Figure I-1. A 16x16 aluminum electrode array serves as a
spatial-dependent electrical contact to the PVDF film. At
the base of the array resides a bank of 16 linear MOSFET
amplifiers. The outputs of the 16 amplifiers serve as the
inputs to the 16x1 analog multiplexer.

The multiplexer configuration provides a 'raster scan' function to the 16x16 electrode array. With the first row initially selected (all other rows isolated), the voltage potential residing on the connected sensing electrode is passed to the input of the respective MOSFET amplifier at
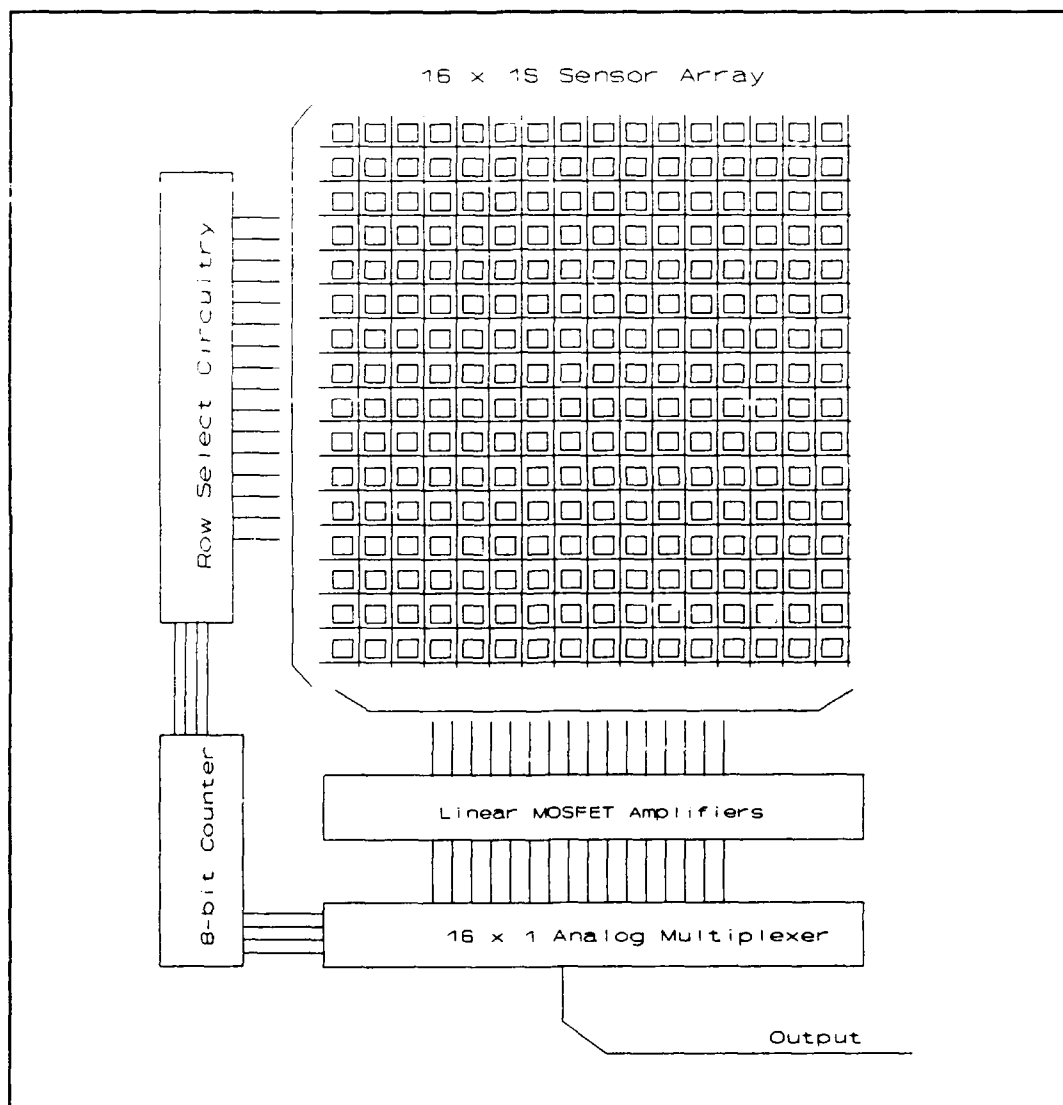
Figure I-1. Circuit design of the multiplexed 16x16 electrode array PVDF tactile sensor.

the base of each column. Employing time-division multiplexing, the analog multiplexer passes the MOSFET amplifier output to external data acquisition instrumentation for subsequent storage and processing.

Two complementary metal-oxide semiconductor (CMOS) transmission gates are electrically coupled to each sensing electrode. One transmission gate passes a voltage potential which establishes a charge on the PVDF film. The second transmission gate couples the charge generated by pressure applied to the PVDF film to the MOSFET amplifiers. Selection (or non-selection) of a transmission gate occurs with the appropriate logic level potential being applied at the gate of each transistor, as described in Chapter 4.

Tactile Sensor Fabrication. The tactile sensor is fabricated by accomplishing four basic steps:

1) neutralizing the charge on the PVDF film,

2) application of adhesive to couple the PVDF film to the sensing array,

3) compression curing to ensure a complete bond, and

4) AC/DC initialization state bias voltage application (in addition, a high-frequency, low-level sinusoidal potential was utilized to induce a quasi-equilibrium state in the PVDF film).

Performance Evaluation. Performance evaluation of the amplifier array occurred upon receipt of the fabricated IC's from MOSIS. Prior to mounting the PVDF film over the sensor

element array, the amplifier array was physically examined and electrically characterized.

The PVDF film was characterized for its piezoelectric activity and polarization prior to being attached to the IC. Once coupled to the amplifier array, a comprehensive three tier performance evaluation of the completed tactile sensor was accomplished. First, each sensor element was tested for proper operation over a range of AC/DC biasing conditions. Second, the degree of coupling between nearest-neighbor elements was accomplished. The third evaluation consisted of testing the entire sensor array to various load conditions. Loads spanning 1-100 g were applied to the tactile sensor area. Selected test load shapes included: rectangular, circular, toroidal, and hexagonal.

Order of Presentation

Chapter II provides a brief literature review of piezoelectric tactile sensor research accomplished over the past five years. The fundamental theory of piezoelectricity and piezoelectric materials are presented in Chapter III. Chapter IV includes pertinent design rationale and outlines the general approach and procedures discussed in this chapter. The test results and corresponding analysis are presented in Chapter V. A summary of the pertinent conclusions and recommendations are outlined in Chapter VI.

A comprehensive list of equipment and materials is presented in Appendix A.

II. Background

A robotic tactile sensor is an imaging device used to
gather information concerning the topography and force
levels that a computer controlled robot is experiencing.
While other imaging techniques exist (optical and acoustic),
tactile sensing is the only technique requiring physical
contact between a robotic manipulator and the environment
[3:208-211]. Coupled with optical imaging, tactile sensors
provide the information necessary for a robot to properly
grasp an object.

The design criteria for a general purpose tactile
sensor includes incorporating many sensing electrodes
(typically 64 to 256), high spatial resolution (1 mm center-
to-center spacing), the ability to conform to a contacted
surface, fast response time (100 Hz), and low hysteresis
[4:18]. In addition, the sensing of shear forces at the
interface between a robotic manipulator and a surface would
provide slip detection of an object. The imitation of human
tactile sensory capabilities is recognized as the final goal
of the research concerned with tactile sensors [5:243].

To achieve these attributes, four categories of tactile
sensors are now in the research phase: optical, piezoresis-
tive, piezoelectric, and capacitive [4:18]. This literature
review will be limited to a discussion of piezoelectric
tactile sensors. In particular, only those sensors

fabricated from polyvinylidene fluoride (PVDF) film will be addressed. The literature review provides a summary of current knowledge limited to the past five years. The material is presented in two distinct categories. The first category contains three representative samples of published research from several research facilities. The second category summarizes two theses which describe the research accomplished at the Air Force Institute of Technology (AFIT).

1. Representative Research

<u>University of Pisa, Italy</u>

In 1985, Paolo Dario and Danilo De Rossi published a report describing an advanced tactile sensor concept [6:52]. Using the results of previous research, the first attempt at simulating the biological sensing mechanisms of human touch was accomplished; that is, a two-level "skin" with an epidermal and an underlying dermal layer.

Construction of this "finger sensor" consisted of a non-conducting elastomer sandwiched between two PVDF film layers, as shown in Figure II-1. A resistive coating between the upper PVDF film and the elastomer facilitated the thermal sensing function. The upper surface of the dermal PVDF layer was attached to a rigid metal plate, and

the lower surface was coated with a non-conducting adhesive, which bonded the sensor to electrodes on a printed circuit board (PCB). The sensor consisted of an 8x16 array of circular electrodes, spaced 3 mm apart, and it possessed overall dimensions of 1x2 inches [7:200]. Minimum force (load) sensitivity for this device was 20 g, and it possessed a bandwidth of 100 Hz [7:185].
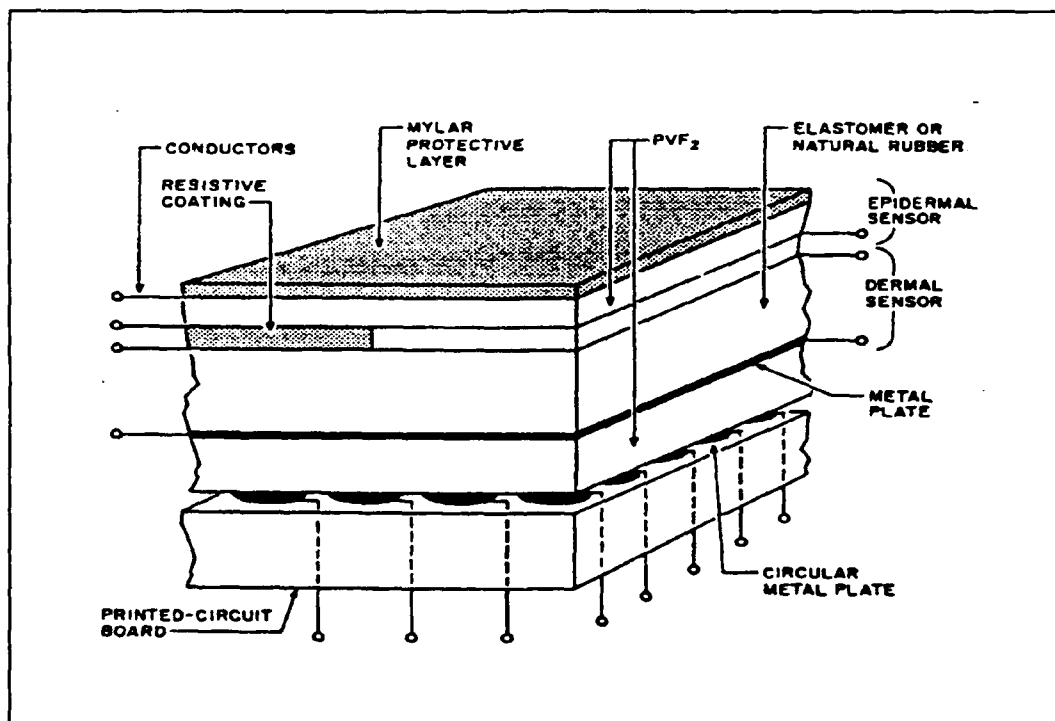
Figure II-1. Complex Tactile Sensor [7:200].

When a force (load) is applied to the top of the sensor, both PVDF layers are compressed, generating an output voltage at the appropriate PCB electrode. Pressure at the dermal PVDF layer provides capacitively-coupled charge to the circular plate electrodes on the PCB.

Dario's tactile sensor represents the first attempt at realizing a complex human-like tactile sensor. While this effort represents a potential general design for future sensors, improved spatial resolution and signal bandwidth must be realized.

Drexel University

In 1986, Kyung Park, developed a PVDF sensor using silver impregnated silicon rubber (SISR) to increase the sensitivity achieved with PVDF sensors [8:4-47]. The 8x8 PVDF planar sensing array consisted of circular sensing elements, each having a 2.1 mm diameter and a spatial resolution of 2.5 mm (Figure II-2). A layer of PVDF was sandwiched between two SISR layers. The application of a force on the sensor's surface resulted in an orthogonal force through the SISR, and it produced a longitudinal stretching of the PVDF film [8:4-52]. Increasing the compliance of the SISR produced increased sensor sensitivity [8:4-57].

Test results indicated that the sensor sensitivity was 3.2 times greater than a direct PVDF sensor (using 6 μm thick PVDF film) [8:4-68]. Since a rubber protective pad was placed over the sensor's surface, the resolution between elements was substantially reduced (depending on pad
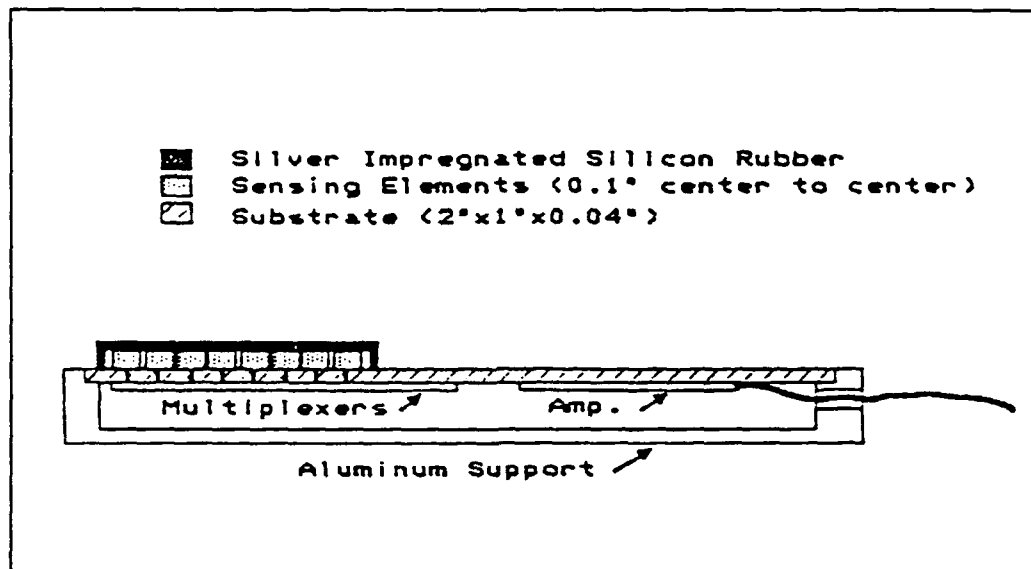
Figure II-2. Silver Impregnated Silicon Rubber Device [8:4-63]

thickness). For example, the ratio of crosstalk to transmitted pressure (with respect to adjacent sensor elements) was 1:1.9 for a 0.055" thick protective pad [8:4-59].

Based upon the experimental results for this sensor, SISR tends to increase overall sensitivity, but the protective rubber pad decreases the resolution.

Bonneville Scientific Laboratories

Grahn and Astle fabricated a tactile sensor array, and PVDF was used as an ultrasonic transmitter and receiver [9:4-5]. Construction of this device consisted of a PVDF film patch (with electrodes as shown), sandwiched between a

rigid substrate and silicone rubber membrane (Figure II-3).
As shown, the silicone rubber membrane's thickness can be
determined by the time required to traverse the rubber pad
and return to the sensing element's electrodes. When a
force is applied to the rubber surface, the time required
for the ultrasonic pulse to traverse the thickness of the
pad is reduced by a proportionate amount. Numerous arrays
were tested with a varying number of elements and spatial
separations. The fabrication of a sensor possessing a
0.5 mm spatial resolution with a linear sensitivity of 0.6 g
to 1200 g is considered feasible.
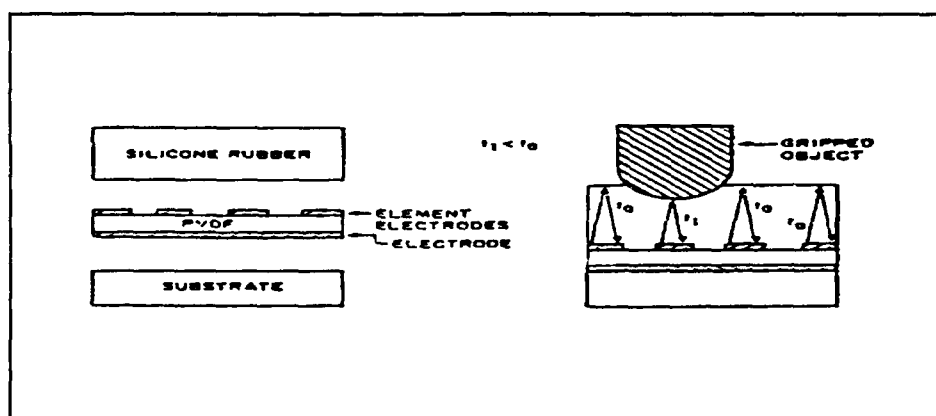
Figure II-3. Ultrasonic tactile sensor [9:4-5].

This sensor configuration represents an inexpensive
rcbotic force sensor concept due to the PVDF film's
conformal property and close acoustic match to the silicone
rubber. However, a great deal of signal processing must be
accomplished with this type of sensor.

2. AFIT Research.

Capt Pirolo

Captain David Pirolo conducted basic research on PVDF
tactile sensors for military applications in potentially
hazardous environments. Capt Pirolo's primary objective was
to characterize a 5x5 sensor array composed of discrete
(3 mm x 3 mm squares) sensor elements using two PVDF film
thicknesses [10:xvii]. A second goal was to determine which
two electrode configurations should be used in future AFIT
research.

Following extensive research and experimentation, Capt
Pirolo concluded that a discrete electrode configuration
(compared to a stripe design) coupled to a 40 μm thick PVDF
film was the optimum candidate [10:6.1].

Capt Reston

Capt Rocky Reston designed, fabricated, and tested a
robotic tactile sensor fabricated from PVDF film coupled to
a silicon host wafer containing resident amplification
circuitry, as shown in Figure II-4. The sensor was composed
of a 5x5 array (25 electrodes), with individual square pads
which measured 0.6 mm x 0.6 mm. Each electrode was
separated from its nearest neighbor by 0.6 mm. Four PVDF
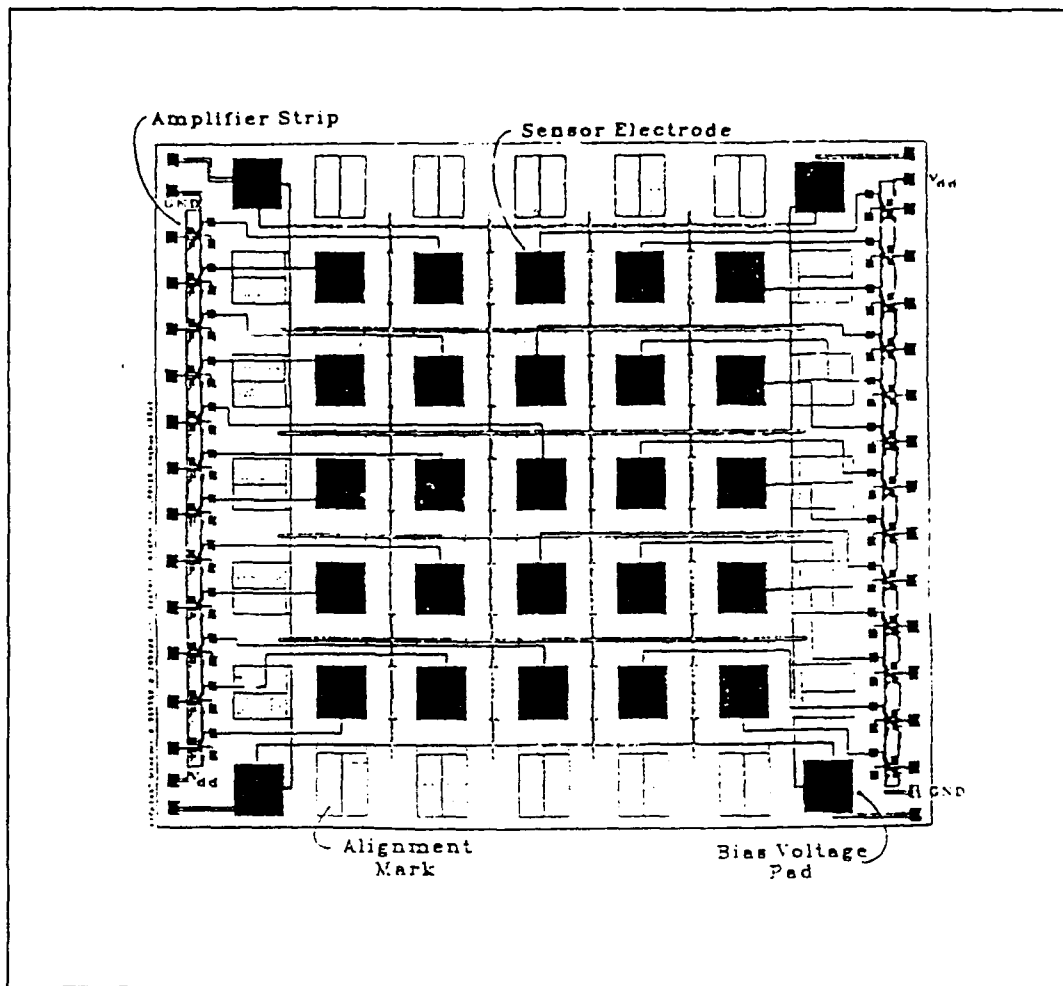
Figure II-4. Captain Reston's piezoelectric tactile sensor integrated circuit [2].

film thicknesses were used: 25 μm, 40 μm, 52 μm, and 110 μm [2:xiii].

Testing the design employed in this thesis effort was a nearly complete success. The 25 μm thick PVDF film configuration displayed the most promising tactile sensor performance (linear response spanning the 0.8 g - 76 g load range) [2:5-1]. In addition, the sensor displayed no observable coupling between nearest neighbors [2:5-1].

Difficulties associated with establishing a consistent bias voltage across the electrode array, as well as the adherence of the PVDF film to the electrode array were the most significant difficulties encountered.

SUMMARY

Like any new technology, the research facilities investigating the tactile sensor technology employ their own methodology for defining and fabricating tactile sensors (usually until an industry standard is defined). The papers discussed in this literature review represent a sample of the current PVDF tactile sensor research.

The main goal of tactile sensor research, as discussed above, is to simulate human touch. For AFIT, the obvious next step is to increase the electrode array density (still confined to the same spatial dimensions utilized in the Reston thesis), produce a suitable bond between the PVDF film and the sensor array, and provide a means for providing a constant voltage bias level across the array.

III. PIEZOELECTRIC EFFECT THEORY AND APPLICATIONS

This thesis utilizes polyvinylidene fluoride film (PVDF) (a piezoelectric polymer) to realize a robotic tactile sensor. To fully appreciate this material's performance characteristics, a basic understanding of piezoelectricity and piezoelectric devices is important.

Definition

Piezoelectricity is the natural ability of some materials to generate electricity when compressed, or change dimensions when exposed to an electric field. The best formal definition of the direct piezoelectric effect has been composed by Walter Cady in his book, **Piezoelectricity** [11:4]:

> electric polarization produced by mech-
> anical strain in crystals belonging to
> certain classes, the polarization being
> proportional to the strain and changing
> sign with it.

Piezoelectricity and piezoelectric devices have significantly contributed to modern electronic technology. Modern lifestyles would not be the same without piezoelectric devices. Communication, robotic, security, and other major electronic systems depend on the piezoelectric effect for efficient operation.

HISTORY

Although the piezoelectric effect has been known for over 200 years, formal credit for its discovery is attributed to Jacque and Pierre Curie. In 1880, the Curies' announced that certain crystals, when compressed in particular directions across two crystal surfaces, generated positive and negative charges on two other surface areas, and the amount of charge was found to be proportional to the applied pressure. This phenomenon is known as the direct piezoelectric effect [11:2].

After analyzing the Curies' paper, Lippman postulated that an equivalent form of thermodynamic laws for reversible processes may exist for this direct piezoelectric effect. Just prior to the end of 1881, the Curies' reported that this was indeed true. That is, applying external charge to the faces of crystals exhibiting the direct piezoelectric effect, a mechanical stress, originating from within, appeared on those crystal's surfaces. This characteristic of piezoelectric crystals is known as the converse piezoelectric effect [11:4]. By studying the piezoelectric quartz crystal, the Curies' discovered that if the external stress remained below certain levels, Hooke's law for elastic materials applied. In addition, they observed that the piezoelectric coefficients of direct and converse piezoelectric phenomenon were the same.

The Curies' discovery attracted others into the field of piezoelectric research. By 1894, Woldemar Voight, a crystallographer, had completed significant research in the field by determining that 20 of the 32 crystal classes possessed the piezoelectric effect [11:5]. Further significant research in piezoelectricity was not reported until World War I.

In 1916, Langevin conceived the idea of exciting quartz plates with a voltage signal to generate acoustic waves underwater [11:5]. These waves would travel through the water, and would be reflected after striking a submersed object. These reflected waves could then be received using a separate set of quartz plates. This system defined the basic principles of sonar. This discovery identified Langevin as the originator of the science of ultrasonics, commonly used today for applications in biology, chemistry, and industry [11:5].

In 1918, Walter Cady announced the development of a piezoelectric resonator. By employing both the direct and converse piezoelectric properties of quartz, an externally applied electric field was used to establish a mechanical resonance within the crystal lattice [11:6]. This discovery was heralded as a major breakthrough, especially in the field of communications, where the quartz resonator is used extensively as a frequency controlling device.

Following World War I, G.W. Pierce used the vibrating crystal phenomenon to design an acoustic interferometer. Used primarily for investigating gas and liquid properties, the interferometer uses the principle of optical diffraction caused by high-frequency compressional waves contained within the substance under test [11:6].

Researchers in recent history have developed new and exciting uses for piezoelectric devices. Of these, sensing transducers have been among the most significant. Transducers use the direct piezoelectric effect as a means for transforming mechanical motion into e'ectrical energy.

Piezoelectricity may best be described by considering an atomic description of the piezoelectric effect, followed by a macroscopic view of the piezoelectric constants.

PIEZOELECTRICITY

Crystallographers recognize 32 classes of crystals, 20 of which manifest piezoelectric properties [12:3]. These classes are based on points, lines, and planes (or combinations) of symmetry within the crystal. Eleven crystal classes demonstrate total symmetry about a single point. Crystal symmetry of this type is referred to as centrosymmetric, has no polar qualities, and does not manifest a piezoelectric effect [11:17]. All other crystal classes lack this center of symmetry, except for the enantiomorphous

hemihedral structure, as defined by Voight [11:20]. Figure
III-1 shows two crystal types, one with a center of
symmetry, and one without. When a crystal lacking a center
of symmetry is mechanically stressed due to an applied
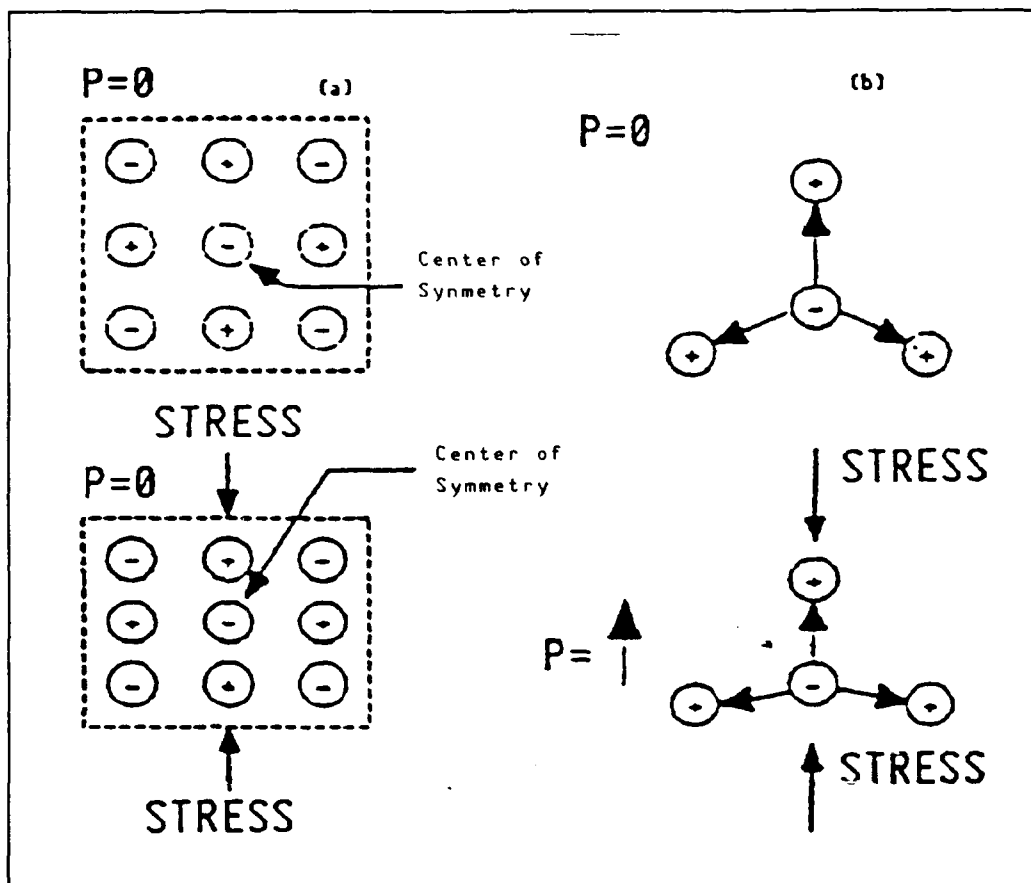
Figure III-1. Center of Symmetry for a Crystal
Structure. (a) With Center of Symmetry, (b) Without
Center of Symmetry. [2:2-4]

force, the crystal physically distorts, causing a polar-
ization of charge within the crystal lattice.

To fully comprehend the center of symmetry phenomenon,
the physics which describe the behavior of an electric
dipole can be utilized. Figure III-2 shows two point

charges of opposite polarity, separated by a small distance
(d). If an observation point (P) exists some distance (r)
from a midpoint between the two charges, a voltage potential
exists at (P) due to the charges (+Q) and (-Q), such that:

$$V_1 = \frac{+Q}{4\pi\epsilon r_1} \qquad (V) \qquad (1)$$

and

$$V_2 = \frac{-Q}{4\pi\epsilon r_2} \qquad (V) \qquad (2)$$

where

V_1 = potential voltage due to the positive
     charge (V)
V_2 = potential voltage due to the negative
     charge (V)
Q = charge (C)
ϵ = permittivity (F/m)
r_1 = distance measured from the point P
     to the positive charge (m)
r_2 = distance measured from the point P
     to the negative charge (m).

Using the principle of linear superposition, the voltage
potential at a point results from the summation of all
individual potential charges surrounding that point [13:29].
Consequently, for the situation in Figure III-2:

$$V = V_1 + V_2 = \frac{Q}{4\pi\epsilon} \left(\frac{1}{r_1} - \frac{1}{r_2} \right) \qquad (V). \qquad (3)$$

Since the distance between point charges is considered much
smaller than the distance to the point of interest (P), then
$r_1 \approx r_2 \approx r$. This approximation implies that:
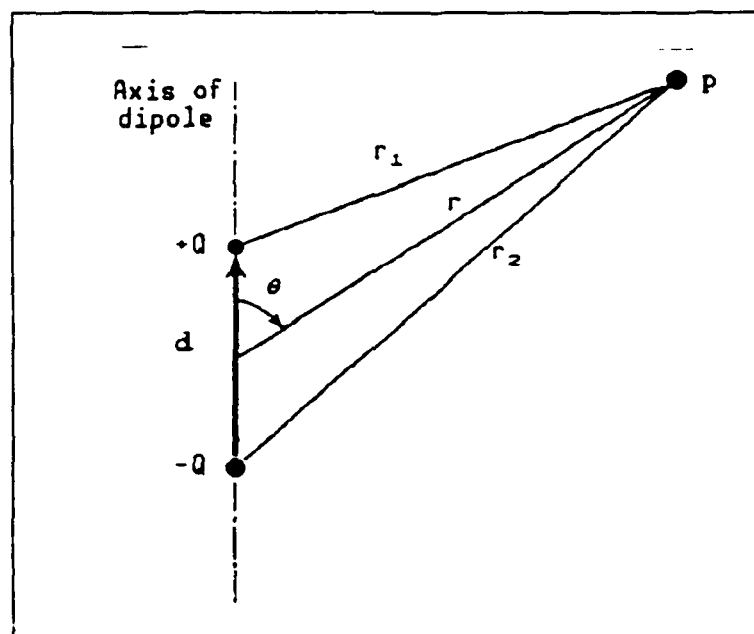
Figure III-2. Electric Dipole [13:35].

$$r_1 = r - \tfrac{1}{2}(d \cdot \cos\theta) \qquad\qquad (m) \quad (4)$$

and
$$r_2 = r + \tfrac{1}{2}(d \cdot \cos\theta) \qquad\qquad (m) \quad (5)$$

where θ is the angle between the dipole axis and the direction to point (P) measured with respect to the midpoint (d/2) of the dipole (along r). Substituting equations (4) and (5) into (3) yields the total potential at a distance r measured with respect to the electric dipole, such that:

$$V = \frac{Q}{4\pi\epsilon} \left(\frac{1}{[r - \tfrac{1}{2}(d \cdot \cos\theta)]} - \frac{1}{[r + \tfrac{1}{2}(d \cdot \cos\theta)]} \right) \quad (V) \quad (6)$$

which reduces to

$$V = \frac{Q}{4\pi\epsilon} \left(\frac{d \cdot \cos\theta}{r^2} \right) \qquad\qquad (V). \quad (7)$$

The dipole induced electric field ($\bar{E}$), is defined by the negative gradient of the corresponding potential voltage (V) [13:35]. Thus, $\bar{E}$ = -del(V), where del(·) is the gradient operator on the scalar potential V. In polar coordinates [8:36]:

$$\bar{E} = -del(V) = -\hat{r}\,\frac{\partial V}{\partial r} - \hat{\theta}\,\frac{1}{r}\,\frac{\partial V}{\partial \theta} \qquad (V/m) \qquad (8)$$

which, after substituting equation (7) into (8), yields:

$$\bar{E} = \hat{r}\,\frac{Qd \cdot \cos\theta}{2\pi\epsilon r^3} + \hat{\theta}\,\frac{Qd \cdot \sin\theta}{4\pi\epsilon r^3} \qquad (V/m) \qquad (9)$$

where
  Qd = dipole moment (C·m)
  $\hat{r}$ = unit vector in r direction
  $\hat{\theta}$ = unit vector in θ direction.

When several dipoles exist within a crystal and align along the same axis and direction, a polarized state is said to exist [13:59]. This net polarization ($\bar{P}$) of the crystal is defined as the sum of all individual dipole moments ($\bar{p} = q\bar{d}$) [13:61]. For example, a crystal with trigonal symmetry is shown in Figure III-3. At equilibrium (no external pressure), the net electric field within the structure is zero (Figure III-3a).

However, in Figure III-3b, when a sufficiently large pressure is applied to the external surface of the crystal, it causes a slight distortion of the crystal lattice. This

distortion changes the angle (θ) between the charges, creating a net polarization in the y-direction, such that:

$$\overline{P} = \overline{p}_1 + \overline{p}_2 + \overline{p}_3 \qquad (C/m^2) \qquad (10a)$$

$$= q(\overline{d}_1 + \overline{d}_2 + \overline{d}_3) \qquad (C/m^2). \qquad (10b)$$

Using rectangular coordinates, and with the distance between charges (d) defined to be one unit length,

$$\overline{p}_1 = q(0.0\hat{x} + 1.0\hat{y}) \qquad (C/m^2)$$

$$\overline{p}_2 = q(0.91\hat{x} - 0.43\hat{y}) \qquad (C/m^2)$$

$$\overline{p}_3 = q(-0.91\hat{x} - 0.43\hat{y}) \qquad (C/m^2).$$

This yields a net polarization for the stressed crystal as:

$$\overline{P} = q(0.0\hat{x} + 0.16\hat{y}) \qquad (C/m^2).$$

A similar effect arises when an electric field is applied to certain faces of a piezoelectric crystal (depending upon the crystal type and surfaces), as discussed below.

Positive and negative ions within the crystal structure align in the direction of the applied field, causing mechanical deformations in that direction. This is known as the converse piezoelectric effect [12:56]. Both the direct and converse piezoelectric effects may be predicted by using the appropriate piezoelectric coefficients.
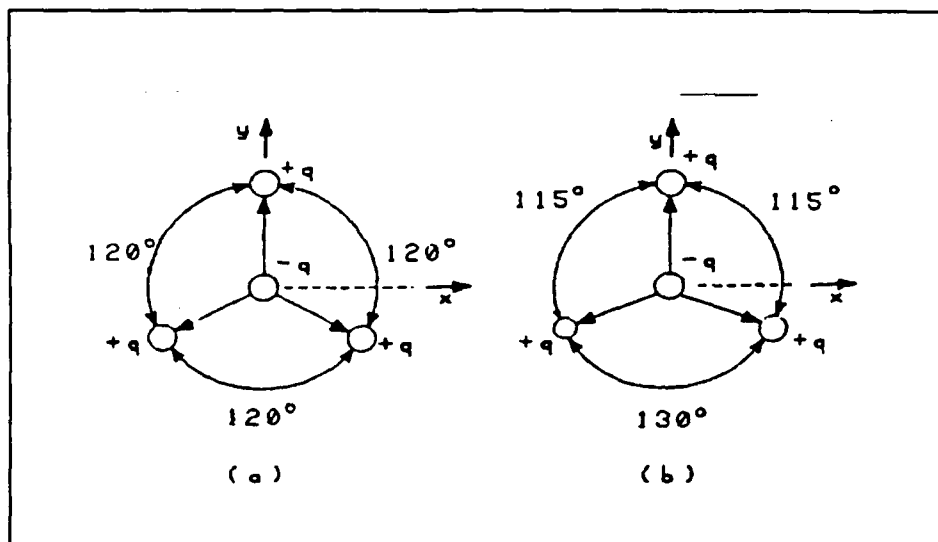
Figure III-3.   Trigonal Crystal Structure.   (a) Unstressed, (b) Stressed [10:2.9].

PIEZOELECTRIC EQUATIONS

The piezoelectricity effect is best described by a set of mathematical equations representing a macroscopic view of the relationships between a piezoelectric material's electro-mechanical properties. These equations are derived from a fundamental understanding of the physical properties acting on and within a non-piezoelectric elastic crystal, which include stress, strain, and polarization [11:177]. With a general knowledge of these basic properties, the effect of an electric potential acting on and within a piezoelectric crystal will complete the mathematical description of the piezoelectric effect. This electric field serves as the distinguishing feature between a piezo-electric and non-piezoelectric device.

In general, stress is the force per unit area acting on the surface of a body [11:45]. An externally applied pressure on a body will contain a normal component (stress) as well as a tangential component (shear) [11:46]. In piezoelectricity, stress refers to a stress system; that is, a combination of applied external mechanical forces and electric fields.

Being a symmetric tensor quantity, a stress system (hereafter referred to simply as stress) has six components: X_x, Y_y, Z_z, Y_z, Z_x, and X_y, which may be written as X_1-X_6, respectively. (The direction of the applied force is identified by the capital letter, while the subscript defines the direction of the normal to the surface upon which the force acts.) That is, X_1-X_3 defines the compressional stress components, while X_4-X_6 identify the shear effects [11:47;2:2-9;10:2.14]. Compressional and extensional stress components (X_1-X_3) are displayed in Figure III-4a and III-4b, respectively, while Figure III-4c shows the shear components (X_4-X_6).

Strain refers to the relative deformation that a crystal structure undergoes when stressed, and is, therefore, unitless [11:48;2:2-9;10:2.15]. Extensional strain refers to a relative expansion of the stressed crystal, while compressional strain exhibits the opposite extensional effect. Figure III-5 shows the effects of extensional strain on the equilibrium coordinates x, y, and
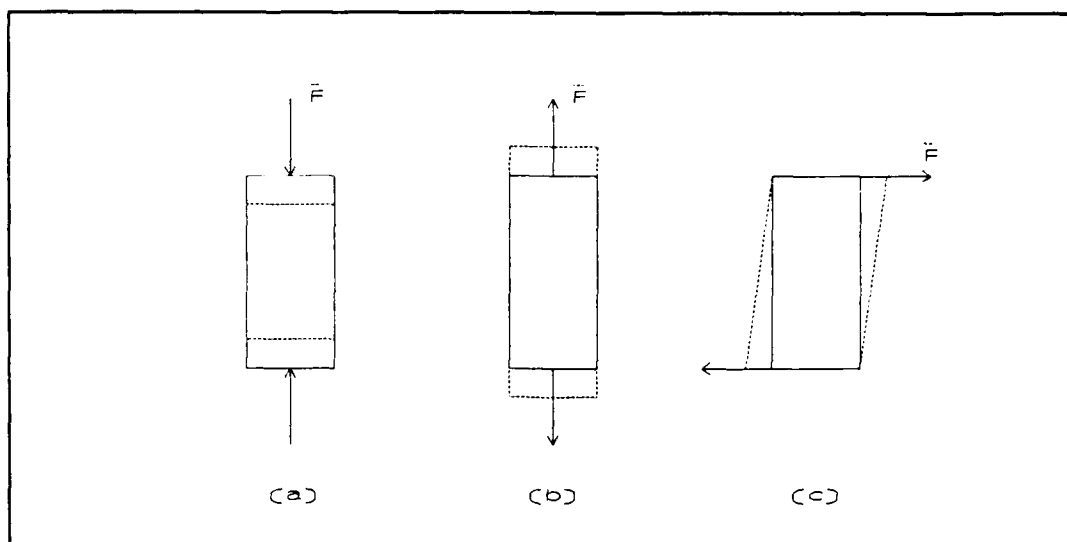
Figure III-4.   Stress system in a piezoelectric device; compressional stress (a), extensional stress (b), and shear stress (c).
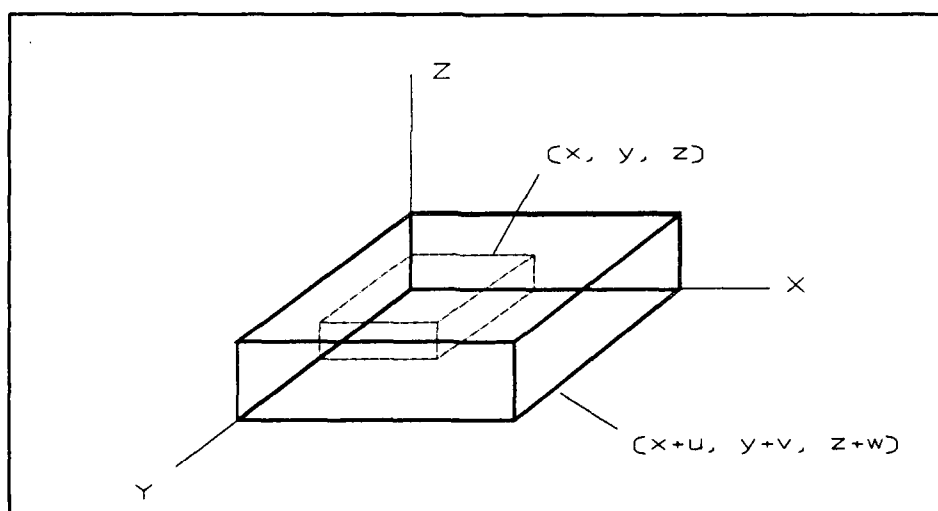
Figure III-5.   Piezoelectric Strain in the x-, y-, and z-direction [10:2.16].

z, displaced by distances u, v, and w.   The new coordinates will be x+u, y+v, and z+w.   Correspondingly, a crystal undergoing compressional strain would have coordinates x-u, y-v, and z-w.

III-12

Like stress, strain is also composed of six components x_x, y_y, z_z, y_z, z_x, and y_y. Strain is sometimes represented with the alpha-numeric notation, S_1-S_6; where S_1-S_3 represents extensional strain, and S_4-S_6 represents the shearing strain components [2:2-9].

Polarization caused by an applied stress has only three degrees of freedom, P_1, P_2, and P_3. This characteristic represents polarization in the x-, y-, and z-directions, respectively [2:2-10;15:2.18]. Figure III-6 shows the polarization (alignment of electric dipoles) in a piezoelectric device.
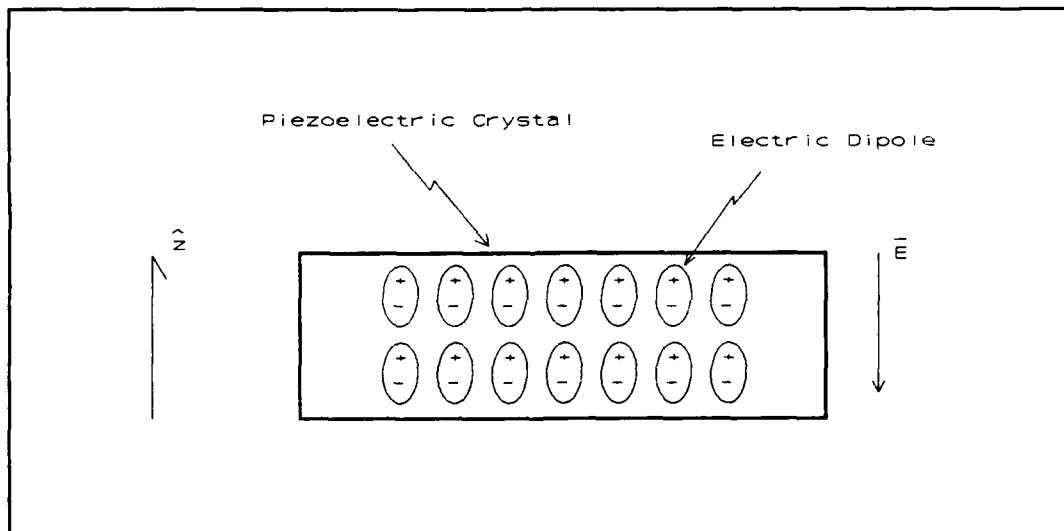
Figure III-6. Polarization of a piezoelectric device in the (+z)-direction.

RELATIONSHIP BETWEEN STRESS AND STRAIN

The six stress and three electric polarization components produce 18 possible electro-mechanical relationships

within a crystal [11:178]. These 18 relationships define the piezoelectric coefficients.

Non-piezoelectric Elastic Crystals. For a crystal with elastic properties, stress and strain behave linearly within the elastic limit [11:48;2:2-11]. Relating polarization and electric field to stress requires introducing the corresponding linear piezoelectric coefficients: stiffness and compliance. The stiffness coefficients, c_{ij}, relate stress (X) components to strain (S) components, such that [11:49]:

$$
\begin{aligned}
X_1 &= c_{11}S_1 + c_{12}S_2 + c_{13}S_3 + c_{14}S_4 + c_{15}S_5 + c_{16}S_6 \\
X_2 &= c_{21}S_1 + c_{22}S_2 + c_{23}S_3 + c_{24}S_4 + c_{25}S_5 + c_{26}S_6 \\
X_3 &= c_{31}S_1 + c_{32}S_2 + c_{33}S_3 + c_{34}S_4 + c_{35}S_5 + c_{36}S_6 \\
X_4 &= c_{41}S_1 + c_{42}S_2 + c_{43}S_3 + c_{44}S_4 + c_{45}S_5 + c_{46}S_6 \quad (N/m^2) \quad (11a)\\
X_5 &= c_{51}S_1 + c_{52}S_2 + c_{53}S_3 + c_{54}S_4 + c_{55}S_5 + c_{56}S_6 \\
X_6 &= c_{61}S_1 + c_{62}S_2 + c_{63}S_3 + c_{64}S_4 + c_{65}S_5 + c_{66}S_6
\end{aligned}
$$

or in matrix notation (denoted in bold text):

$$
\mathbf{X} = \mathbf{cS} \qquad (N/m^2). \qquad (11b)
$$

Similarly, stress (X) can be described in terms of strain (S) [11:49], such that:

$$
\begin{aligned}
S_1 &= s_{11}X_1 + s_{12}X_2 + s_{13}X_3 + s_{14}X_4 + s_{15}X_5 + s_{16}X_6 \\
S_2 &= s_{21}X_1 + s_{22}X_2 + s_{23}X_3 + s_{24}X_4 + s_{25}X_5 + s_{26}X_6 \\
S_3 &= s_{31}X_1 + s_{32}X_2 + s_{33}X_3 + s_{34}X_4 + s_{35}X_5 + s_{36}X_6 \quad (12a)\\
S_4 &= s_{41}X_1 + s_{42}X_2 + s_{43}X_3 + s_{44}X_4 + s_{45}X_5 + s_{46}X_6 \\
S_5 &= s_{51}X_1 + s_{52}X_2 + s_{53}X_3 + s_{54}X_4 + s_{55}X_5 + s_{56}X_6 \\
S_6 &= s_{61}X_1 + s_{62}X_2 + s_{63}X_3 + s_{64}X_4 + s_{65}X_5 + s_{66}X_6
\end{aligned}
$$

where s_{ij} is called the compliance coefficient (which relates strain (S) to stress (X)), and the strain (S) is a unitless quantity. Matrix notation yields:

$$S = sX \qquad \text{(unitless)}. \qquad (12b)$$

Relating the stiffness coefficients to the compliance coefficients yields:

$$c_{ij} = S_{ij}/D \qquad (13a)$$

where c_{ij} are the stiffness coefficients, S_{ij} is the cofactor of equation 12a with respect to s_{ij}, and D is the determinant of the compliance coefficients of the same equation [11:49]. For example, the stiffness coefficient c_{11} would require calculating the cofactor S_{11}:

$$S_{11} = \begin{vmatrix} s_{22} & s_{23} & s_{24} & s_{25} & s_{26} \\ s_{32} & s_{33} & s_{34} & s_{35} & s_{36} \\ s_{42} & s_{43} & s_{44} & s_{45} & s_{46} \\ s_{52} & s_{53} & s_{54} & s_{55} & s_{56} \\ s_{62} & s_{63} & s_{64} & s_{65} & s_{66} \end{vmatrix}. \qquad (13b)$$

The polarization ($\bar{P}$) in an elastic crystal is given by:

$$\begin{aligned} P_1 &= \epsilon_{11}E_1 + \epsilon_{21}E_2 + \epsilon_{31}E_3 \\ P_2 &= \epsilon_{12}E_1 + \epsilon_{22}E_2 + \epsilon_{32}E_3 \\ P_3 &= \epsilon_{13}E_1 + \epsilon_{23}E_2 + \epsilon_{33}E_3 \\ P_4 &= \epsilon_{14}E_1 + \epsilon_{24}E_2 + \epsilon_{34}E_3 \\ P_5 &= \epsilon_{15}E_1 + \epsilon_{25}E_2 + \epsilon_{35}E_3 \\ P_6 &= \epsilon_{16}E_1 + \epsilon_{26}E_2 + \epsilon_{36}E_3 \end{aligned} \qquad (C/m^2) \qquad (14a)$$

or in matrix notation:

$$P = \epsilon E \qquad (C/m^2) \qquad (14b)$$

where ϵ is the material's dielectric coefficient (a tensor quantity), and E is the applied electric field [2:2-11].

The above relations describe non-piezoelectric devices. Piezoelectric devices utilize not only the above equations, but include additional terms generated from the piezoelectric effect. These additional terms arise from the fact that a mechanical strain generates an electric polarization, and an externally applied electric field generates a mechanical stress [11:183;2:2-11].

Piezoelectric Crystals. Applying an electric field to a piezoelectric crystal causes a mechanical distortion; that is, the converse piezoelectric effect. For practical applications, which consider the materials to be within the elastic limit, the linear mathematical relationship for the strain may be expressed as:

$$
\begin{aligned}
S_1 &= d_{11}E_1 + d_{21}E_2 + d_{31}E_3 \\
S_2 &= d_{12}E_1 + d_{22}E_2 + d_{32}E_3 \\
S_3 &= d_{13}E_1 + d_{23}E_2 + d_{33}E_3 \\
S_4 &= d_{14}E_1 + d_{24}E_2 + d_{34}E_3 \\
S_5 &= d_{15}E_1 + d_{25}E_2 + d_{35}E_3 \\
S_6 &= d_{16}E_1 + d_{26}E_2 + d_{36}E_3
\end{aligned}
\qquad \text{(unitless)} \qquad \text{(15a)}
$$

or in matrix notation:

$$
S = dE \qquad\qquad \text{(unitless)} \qquad \text{(15b)}
$$

where E is the applied electric field, S is the resulting strain, and d is the piezoelectric strain coefficient [12:56].

A similar relationship may be expressed when an applied mechanical stress causes an induced electric field, such that:

$$
\begin{aligned}
E_1 &= g_{11}X_1 + g_{21}X_2 + g_{31}X_3 \\
E_2 &= g_{12}X_1 + g_{22}X_2 + g_{32}X_3 \\
E_3 &= g_{13}X_1 + g_{23}X_2 + g_{33}X_3 \\
E_4 &= g_{14}X_1 + g_{24}X_2 + g_{34}X_3 \\
E_5 &= g_{15}X_1 + g_{25}X_2 + g_{35}X_3 \\
E_6 &= g_{16}X_1 + g_{26}X_2 + g_{36}X_3
\end{aligned}
\qquad \text{(unitless)} \qquad (16a)
$$

or in matrix notation:

$$
\mathbf{E} = \mathbf{g}\mathbf{X} \qquad\qquad (16b)
$$

where $\mathbf{X}$ is the applied stress, g_{ij} is the piezoelectric voltage coefficient, and $\mathbf{E}$ is the resulting electric field [14:34]. This relationship defines the direct piezoelectric effect.

The induced electric field causes an additional polarization to occur within the crystal's structure. This second (induced) polarization component adds to the polarization effect caused solely by the dielectric constant (equation 14). For practical applications, a linear relationship describes this induced polarization as:

$$
\begin{aligned}
P_1 &= e_{11}S_1 + e_{12}S_2 + e_{13}S_3 + e_{14}S_4 + e_{15}S_5 + e_{16}S_6 \\
P_2 &= e_{21}S_1 + e_{22}S_2 + e_{23}S_3 + e_{24}S_4 + e_{25}S_5 + e_{26}S_6 \\
P_3 &= e_{31}S_1 + e_{32}S_2 + e_{33}S_3 + e_{34}S_4 + e_{35}S_5 + e_{36}S_6
\end{aligned}
\quad (C/m^2). \quad (17a)
$$

Matrix methods allow the prior result to be represented as:

$$
\mathbf{P} = \mathbf{e}\mathbf{S} \qquad (C/m^2) \qquad (17b)
$$

where the e_{ij} terms are the piezoelectric stress coefficients that relate strain **S**, to polarization **P** [12:55]. The total polarization in a piezoelectric crystal is, by superposition, (in matrix form):

$$\mathbf{P} = \epsilon\mathbf{E} + \mathbf{eS} \qquad (C/m^2). \qquad (18)$$

The piezoelectric coefficient equations (rewritten here for convenience) may be manipulated to explicitly yield relationships between the polarization and electric field to stress. That is:

$$\mathbf{X} = \mathbf{cS} \qquad \text{from equation (11b)}$$
$$\mathbf{S} = \mathbf{sX} \qquad \text{from equation (12b)}$$
$$\mathbf{P} = \epsilon\mathbf{E} \qquad \text{from equation (14b)}$$
$$\mathbf{S} = \mathbf{dE} \qquad \text{from equation (15b)}$$
$$\mathbf{E} = \mathbf{gX} \qquad \text{from equation (16b)}$$
$$\mathbf{P} = \mathbf{eS} \qquad \text{from equation (17b).}$$

By eliminating **S** from equations 11b and 14b, and 12b and 13b yields:

$$\mathbf{P} = \mathbf{esX} \qquad (18)$$
$$\mathbf{X} = \mathbf{cdE} \qquad (19)$$

but since **es=d** and **cd=e** [12:57], then:

$$\mathbf{P} = \mathbf{dX} \qquad (20)$$
$$\mathbf{X} = \mathbf{eE} \ . \qquad (21)$$

Combining and rearranging equations 11 through 21 yield the piezoelectric crystal equations (in matrix form). The direct piezoelectric effect can be represented as:

$$P = dX + \epsilon E \qquad (C/m^2) \quad (22)$$

and the converse piezoelectric effect as:

$$S = sX + dE \qquad (unitless). \quad (23)$$

Similarly, a piezoelectric relationship between impressed stress and the electric field is:

$$E = -gX + P/\epsilon \qquad (V/m). \quad (24)$$

Equations 22 and 23 represent the two fundamental piezoelectric equations that relate strain and polarization in terms of stress and electric field. Equation 24 is a supplemental equation specifically relating an applied stress with the corresponding resultant electric field.

One additional term which deserves attention is the coupling factor (k). The coupling factor measures the interchange between the electrical and mechanical energies within a material [14:179]. The principle use of k is realized when applying piezoelectric devices to mechanical systems [11:759]. The coupling factor ranges in value from zero (no piezoelectric effect) to nearly unity [12:2-12]. In addition, the coupling factor squared represents the

ratio of total transformed energy to total input energy [14:390].

PIEZOELECTRIC MATERIALS

Piezoelectric devices can be classified into three categories: single crystal, poled ceramics, and piezoelectric polymer films.

Single Crystal. Several significant single crystal piezoelectric materials have been extensively studied. Quartz and rochelle salt are the two most common single crystal forms discussed.

Quartz, the 'original' piezoelectric crystal, is actually the primary single crystal piezoelectric device used today. Quartz, synonymous with crystalline silicon dioxide (SiO_2), is found in two forms: α- and β-quartz. The α-quartz form has a trigonal crystalline structure and exists below the Curie temperature of 573°C. The β-quartz form is found to exist above the Curie temperature, has a hexagonal centrosymmetric structure, and therefore, is not piezoelectric. Although quartz has a coupling factor of only 0.1 [2:2-14], it is the primary piezoelectric crystal useable for frequency control in the communications field due to its favorable mechanical, electrical, chemical, and thermal properties.

Rochelle salt is another piezoelectric crystal which has been studied extensively. Although rochelle salt has a coupling factor of 0.9, it is extremely environmentally sensitive [2:2-13]. That is, any change in humidity or temperature will cause a significant change in the piezo-electric activity. This behavior is due to the fact that rochelle salt has a high concentration of water molecules within it's structure. Rochelle salt devices have been used for low-frequency transducer applications in tightly controlled environments [2:2-14].

Ceramics. Ceramic piezoelectric devices have all but replaced single crystal devices. A ceramic is a composite of several crystal structures with a dipole in each unit cell which is oriented in a random fashion [15:123]. The ceramic may be transformed into a piezoelectric state by applying a strong electric field across two of the ceramic surfaces, at an elevated temperature, causing a preferential alignment of the dipoles within the crystal. If the temperature is then decreased with the electric field still applied, the electric dipoles will be locked into position [15:123]. Ceramics with a Perovskite crystal structure (Figure III-7) tend to possess significant piezoelectric activity [14:22].
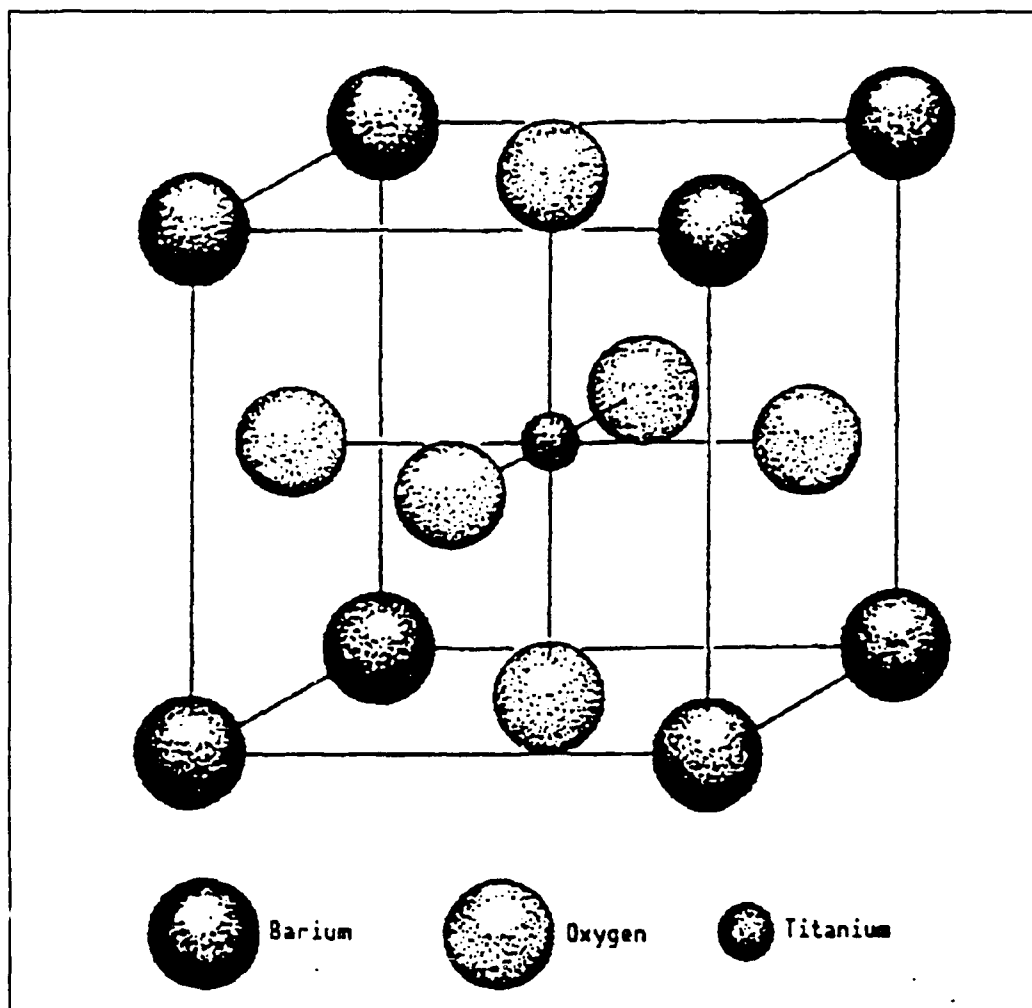
Figure III-7. Perovskite Structure [2:2-16].

Organic Polymers. Organic polymers are classified as materials which contain closely linked carbon and hydrogen atoms [16:137]. These polymers are usually not piezo-electric in their natural state. Of the known piezoelectric polymers, polyvinylidene fluoride (PVDF) has been reported to possess the highest level of piezoelectric activity [17:8].

PVDF, a polymer with a large molecular weight, is composed of the repeat unit (CH_2-CF_2), and is found in two forms, the α- and β-phases [17:26].

When PVDF is synthesized, typically from a melt extrusion technique (although a solution phase is sometimes used), the α-phase of the PVDF polymer is formed as illustrated Figure III-8a. In order to make PVDF piezo-electric, the polymer chain must be oriented (Figure III-8b) by stretching it either uniaxially (x-direction) or biaxially (x- and y-directions) at an elevated temperature [17:28]. After mechanical stretching, the PVDF film is poled. The external electric field aligns the β-phase crystallites normal to the polymer chains, as shown in Figure III-9 [16:29].

PVDF possesses several advantages compared to other piezoelectric materials. While most piezoelectric materials are restricted to a certain frequency range, PVDF exhibits its piezoelectric activity over a very wide range (DC to GHz) [17:55]. In addition, PVDF can be exposed to large electric fields due to its higher dielectric constant of 30 V/micron [17:51]. An additional advantage of PVDF is the physical property attributable to its thinness and flex-ibility; that is, it can be fastened to vibrating structures without causing significant mechanical distortion.

There are two major disadvantages of PVDF compared with other piezoelectric materials. First, it has a small
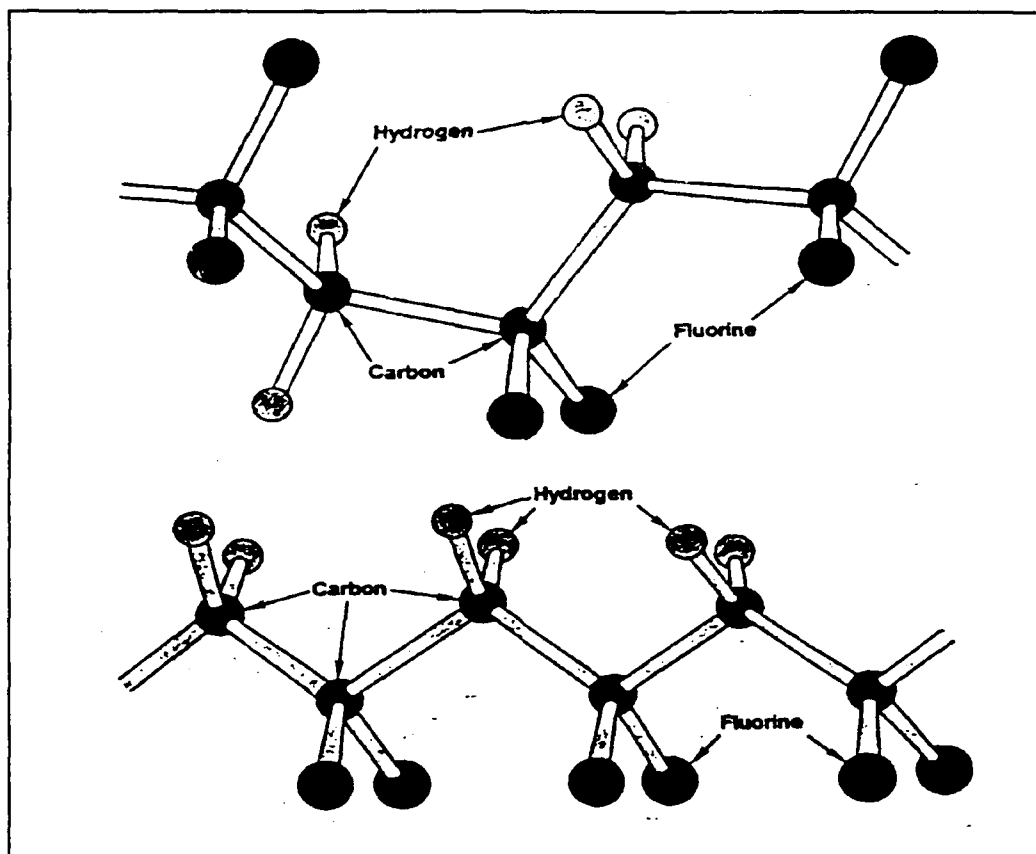
Figure III-8. Polyvinylidene fluoride (a) before poling, and (b) after poling [9].

coupling coefficient (≈ 0.19), indicating a small electro-mechanical energy transfer efficiency [2:2-18;10:2.25-2.26]. A second limitation is its maximum operating temperature ($80°C$ to $120°C$); that is, mechanical relaxation reduces the piezoelectric activity when the temperature exceeds $80°C$ [16:51]. Nevertheless, PVDF possesses a sufficient class of advantages that makes it attractive in many engineering applications.
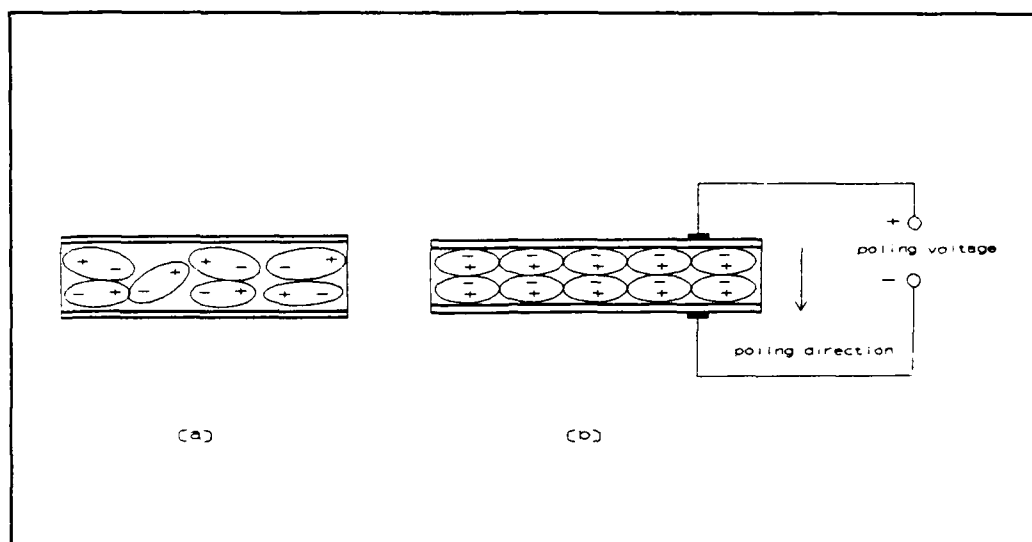
Figure III-9. β-phase PVDF crystallites (a) before poling, and (b) after poling [16:29].

SUMMARY

Piezoelectricity has been known since the beginning of documented history. It was initially defined as the generation of an electric field within a crystal when an external force was applied, and conversely, mechanically distort the device when an electric field is applied. Only within the past century has the underlying causes of piezoelectricity been understood in even the basic sense.

With the fundamental atomic view of piezoelectricity described by an electronic dipole, scientists have developed equations to describe piezoelectricity in terms of stress, strain, and an electric field. Subsequent research has led

to the development of man-made piezoelectric materials, such as ceramics and organic polymers.

With the fundamental characteristics of piezoelectric PVDF film explained, the operating principle behind the PVDF tactile sensor can be fully appreciated. Chapter IV focuses on the design criteria, fabrication techniques, and testing methodology used to yield a functioning tactile sensor.

IV. Design and Performance Evaluation

This Chapter discusses the piezoelectric tactile sensor integrated circuit design, fabrication, and performance evaluation. Experimentally motivated circumstances dictate that this chapter be divided into two parts. The first section deals with the original design considerations of the tactile sensor, while the second provides a detailed account of the design changes which occurred during the performance evaluation phase.

1. Integrated Circuit Design

The overall design of the robotic tactile sensor was accomplished using AFIT computer aided design (CAD) tools. In particular, the integrated circuit layout was implemented using MAGIC, a VLSI circuit layout program [19:125]. The output file produced by MAGIC formulated a Caltech Intermediate Form (CIF) plot [19:9]. This CIF plot was electronically transmitted to the Metal Oxide Semiconductor Implementation Service (MOSIS) for fabrication [20:15]. To obtain the fastest turn-around time from MOSIS, the 2 μm, N-well, double-level metal design rule technology was used.

The fundamental design of the integrated circuit (IC) used in this project was based on Capt Reston's previous thesis design (Figure II-4) [2]. As depicted in

Figure II-4, each sensing electrode is connected to a discrete linear amplifier, where the output signal is coupled to external data acquisition equipment.

Since the number of sensing electrodes in this project was increased from 25 electrodes to 256 electrodes, a more efficient means of acquiring the output signals was devised. A resident analog multiplexer was incorporated into the design to facilitate acquiring the output data, as well as reducing the number of external connections.

The circuit designed for this project is illustrated in Figure IV-1, and may be separated into three distinct functional blocks:

          1) the 16x16 electrode array,

          2) linear amplifiers, and

          3) control circuitry.

Section I: Electrode Array

One of the design criteria for this project stipulated that the 16x16 array must be confined to the peripheral IC die dimensions of approximately 6 mm. To accommodate this constraint, each electrode was sized to be 250x250 μm square, with an edge-to-edge separation of 150 μm between elements, which resulted in a total array area of 640x640 μm.

The 16x16 electrode array provides the 256 electrical contacts necessary to couple the electrical signals generated by the overlaying piezoelectric PVDF film to the linear amplifiers on the tactile sensor. Additionally, each electrode must provide a path to remove stored charge residing on the piezoelectric film [2:5-2].
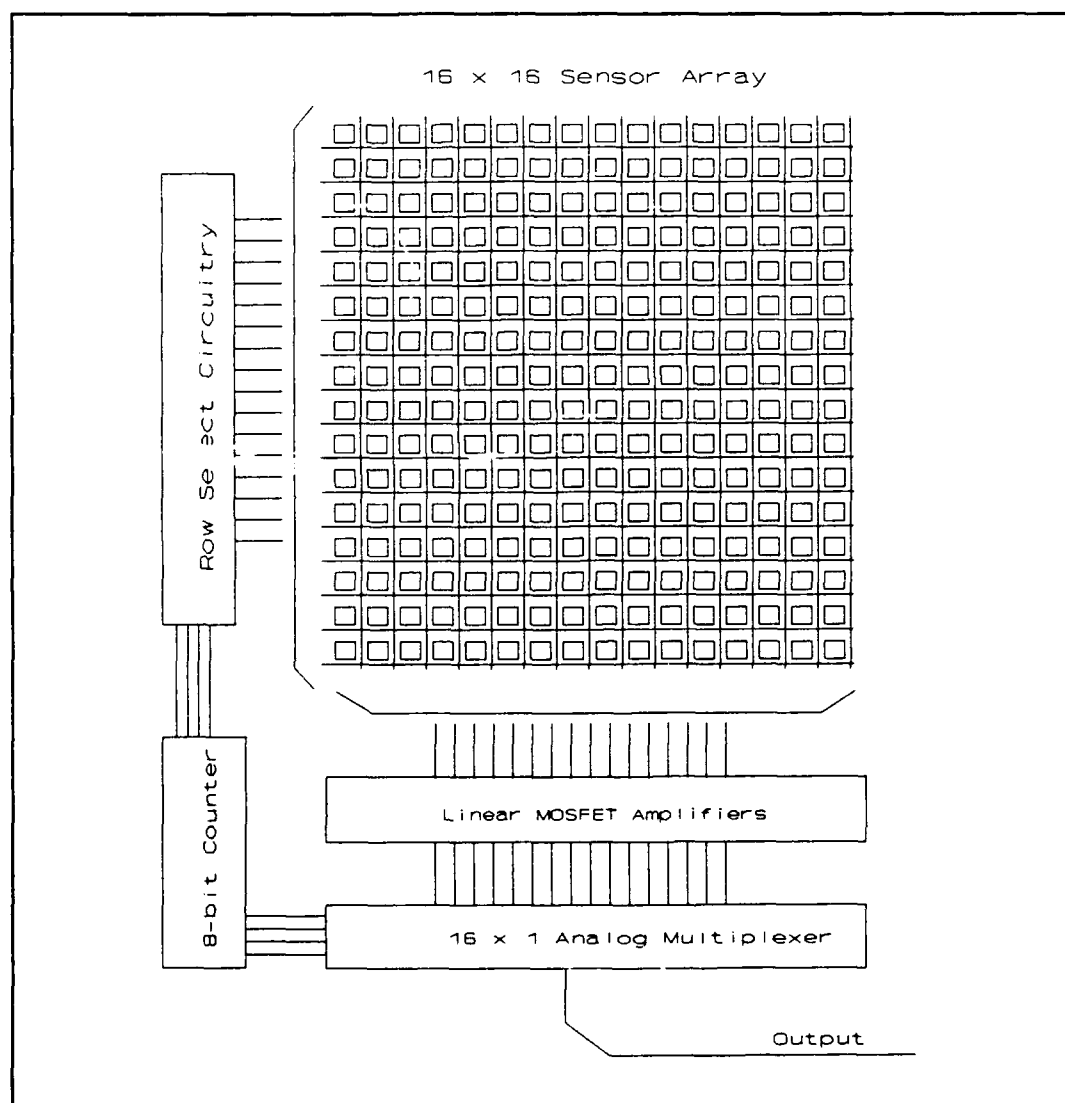
Figure IV-1. Circuit diagram of the 16x16 electrode array PVDF tactile sensor.

To accomplish this bidirectional transfer of charge, two complementary metal-oxide semiconductor (CMOS) transmission gates are electrically coupled to each sensing electrode. Selection (or non-selection) of a transmission gate occurs with the appropriate logic level potential that is applied at the gate of each transistor (Figure IV-2).

As Figure IV-2 illustrates, when the top transmission gate is selected, an electrical signal generated from the PVDF film passes to a MOSFET amplifier. The lower transmission gate is, at this time, turned-off. Likewise, when the sensing electrode is not selected to provide an output signal, the lower transmission gate provides a path to a common biasing point to initialize (establish) the charge state of each sensor element. Simultaneous
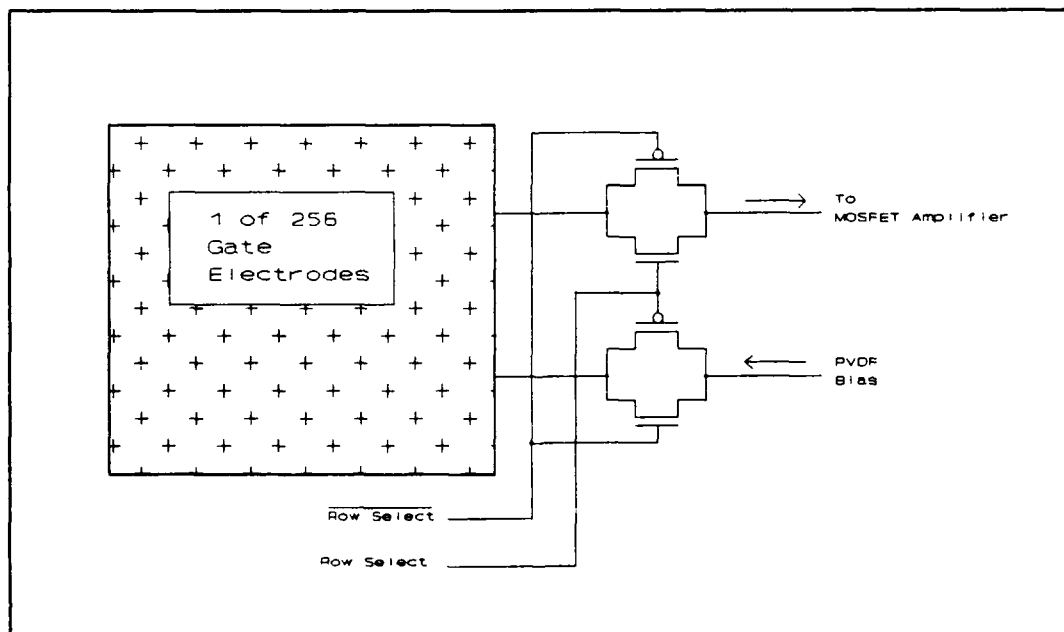
Figure IV-2. Bidirectionality of charge flow through the transmission gates.

selection of transmission gates is prevented by connecting opposite type (NMOS or PMOS) transistors to each control line.

Each transmission gate must either pass a low-level analog signal with minimum distortion (when selected), or totally block a signal (when not selected). The optimum dimensions of the transmission gate transistors were determined by extensive SPICE simulations. Selecting the best transistor configuration for use in this design was based on 2 factors: overall physical dimensions, and the degree of signal attenuation when the transmission gate is either "on" or "off". (Physical dimension was an important consideration because of the limited surface area between individual electrodes). Table IV-1 depicts a summary of the SPICE analysis results for various transistor dimensions.

Table IV-1. Spice simulation results for determining the transmission gate dimensions.

Transistor Gate Dimension (μm) (N-type/P-type)		Attenuation (dB)	
Length	Width	On	Off
2	4/8	10^{-3}	290
3	4/8	150	170
* 3	8/16	8×10^{-3}	300
3	10/20	10^{-9}	300
3	12/24	10^{-9}	290
4	8/16	100	300

* Selected transistor size

Section II: Amplifiers

The basic amplifier design for this project was based on the design reported in the previous thesis [2]. To achieve amplification of the input signal, two inverting amplifiers were placed in series as shown in Figure IV-3.
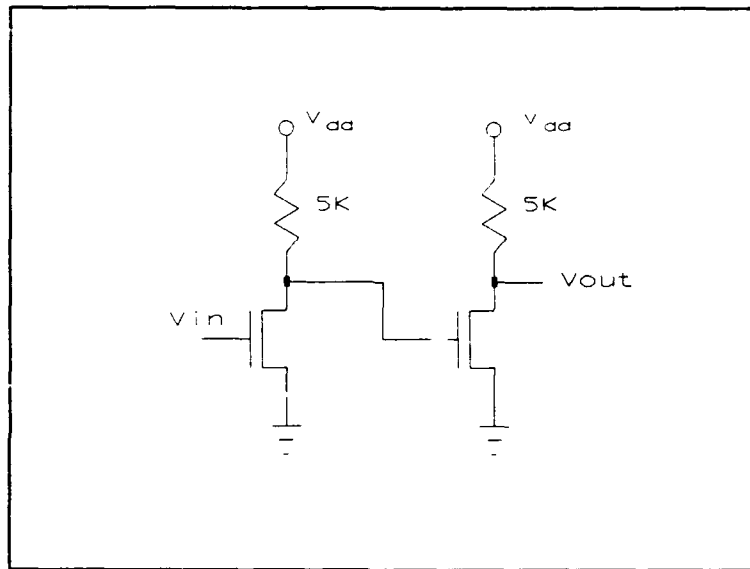
Figure IV-3.   Schematic diagram of the sensor linear amplifier [2].

Determining the operating characteristics of the amplifier required the prediction of voltages generated from the piezoelectric film. The voltage generated by the PVDF film is related to it's thickness and area as [13:70]:

$$V = (qt)/(\epsilon A) \qquad\qquad (V)$$

where

q = charge generated by the piezoelectric film (C)
t = PVDF film thickness (m)
ϵ = $\epsilon_r \epsilon_o$ permittivity of the PVDF film (F/m)
A = surface area of the PVDF film (m^2).

The minimum voltage generated by the piezoelectric film would originate from the thinnest film (25 μm) sustaining a load of 1 g (0.01 N). From the piezoelectric film specifications found in Appendix B, d_{33} is 16 pC/N, and ϵ_r = 11, so that the charge q = 0.16 pC. With the load distributed over the 250x250 μm electrode surface area, the voltage generated would be approximately 0.65 V.

A maximum signal would be achieved with the thickest film (110 μm) sustaining a load of 100 g (1 N). Assuming a linear output response, this load would produce an output voltage of 289 V.

It is readily apparent that the voltage potential generated by the PVDF film will exceed the limits of the 10 V power supply. To accommodate the range of voltages predicted, the amplifier must be biased to its operating point by applying a voltage potential to the upper (metalized) surface of the PVDF film. The polar properties of the PVDF film (due to the dipole moment), allowed direct charge transfer from the metal surface of the PVDF film to the input of the corresponding linear MOSFET amplifier [2:3-8;13:35-37].

SECTION III: Control Circuitry

The control circuitry was designed to provide a 'raster scanning' function to the electrode array, so that the circuit's output could be represented by a time-division multiplexed analog signal.   The control circuitry is composed of one eight-bit counter (incrementer), two 4-bit decoders, one 16x1 analog multiplexer, and two banks of driver circuits, as shown in Figure IV-4.
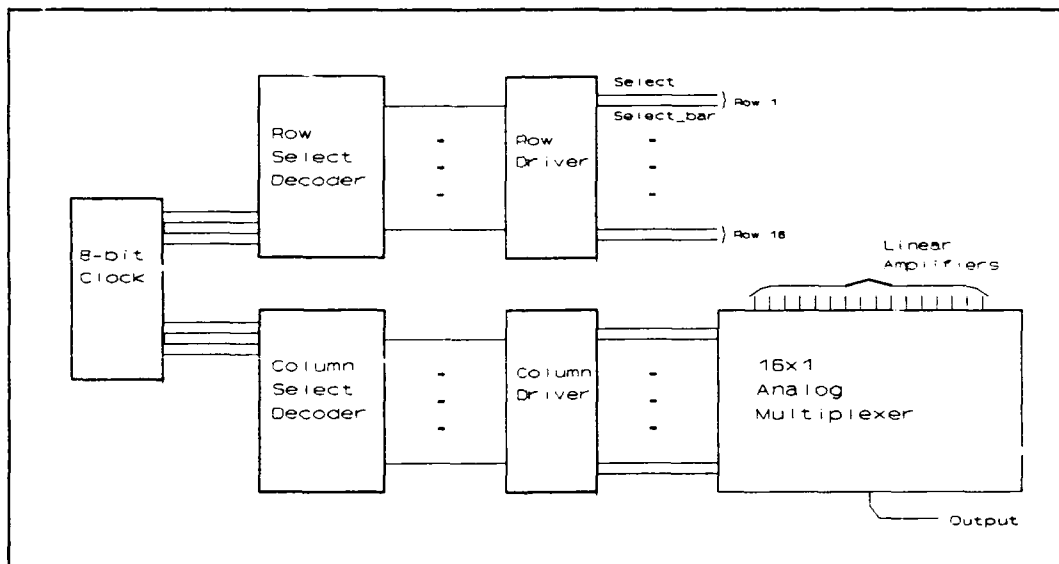
Figure IV-4.   Schematic diagram of the 16x16 electrode array control circuitry.

The eight-bit counter is the mainstay of the overall circuit.   The counter is controlled by an external square wave clock signal, and it includes a reset capability.   The four least-significant bits serve as the control input for one 4-bit decoder (Column Select Decoder), while the four

most-significant bits function as the control input for the second 4-bit decoder (Row Select Decoder). This architecture allows each column to be selected (scanned) once per row, for each of the sixteen rows.

Each decoder employs negative logic, such that a selected output line contains a logic '0', while all other control lines furnish a logic '1'. In addition, each decoder's sixteen output lines are fed into buffer circuits (dual-cascade inverters per line), which serve as drivers for individual control of column and row select circuits.

As discussed above, the output of the Column Select Decoder serves as the input to a driver (buffer). The buffer's output lines are connected to the controlling inputs of a bank of sixteen transmission gates (Figure IV-5). The transmission gate inputs connect to one of 16 MOSFET amplifier outputs. The 16 transmission gate outputs are electrically connected, and serve as a common output line.

Row selection occurs in much the same fashion. The Row Select Decoder is connected to a buffer/driver, which controls the transmission gates on each row, as shown in Figure IV-6. Selection of rows begins with the uppermost row, and proceeds to the lowermost row, as a function of time.
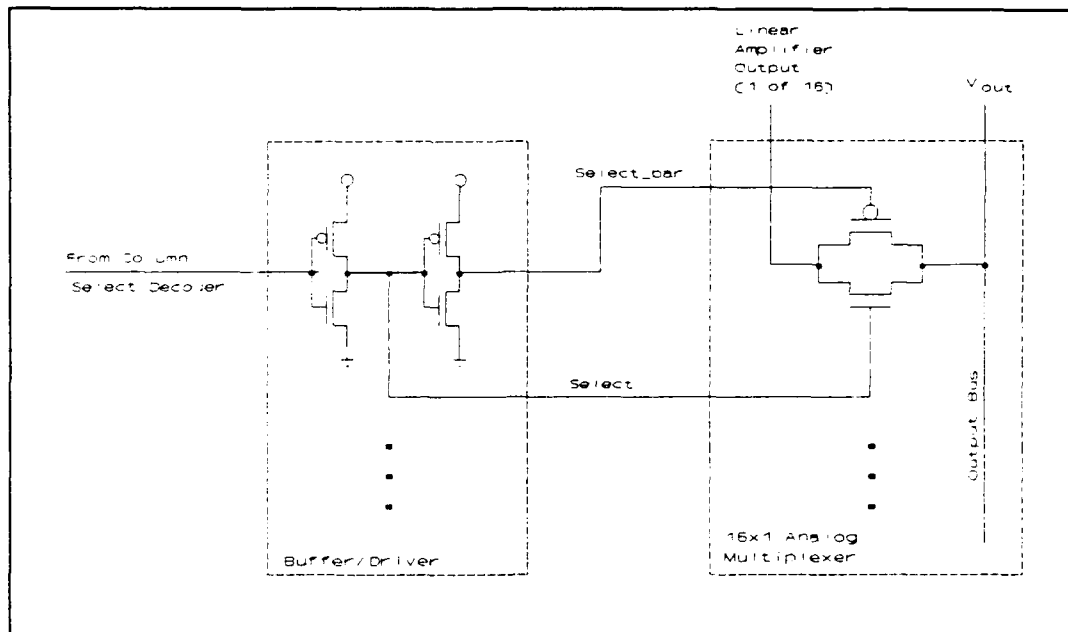
Figure IV-5.   Schematic of the column select circuitry.
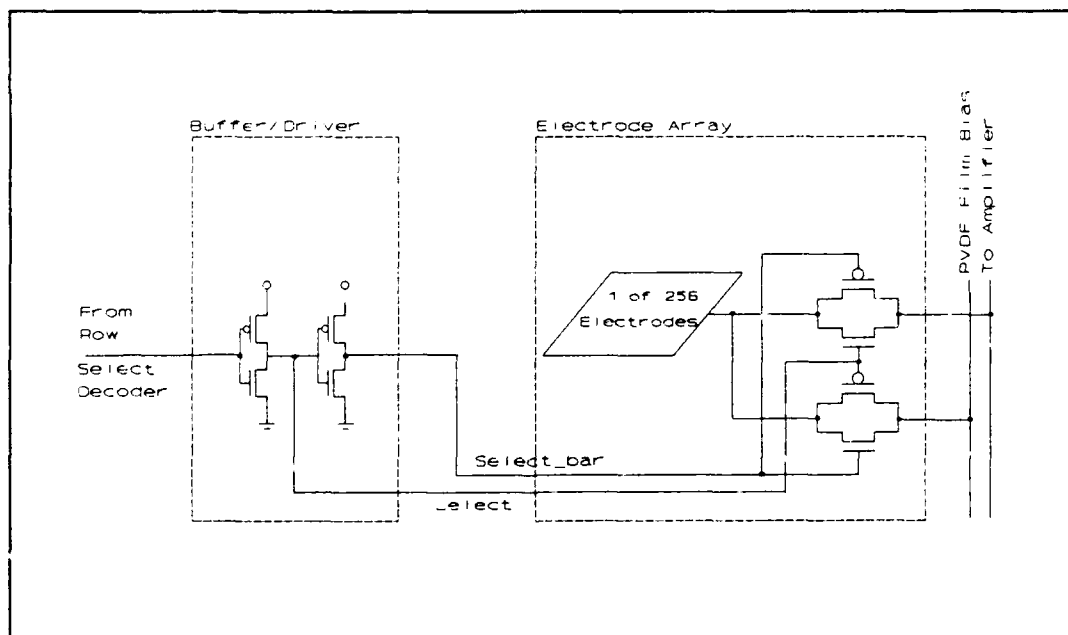
Figure IV-6.   Schematic of the row select circuitry.

Accurate operation of the overall circuit required an optimum transistor design. This was accomplished by extensive SPICE simulations of the circuit for various transistor gate widths and lengths, as discussed below. To be precise, the circuit was simulated from one channel of the Row Select Decoder, through the driver circuit, to the corresponding row in the electrode array, as depicted in Figure IV-7. In addition, the ability of the electrode transmission gate to pass an analog signal to the amplifier was also simulated.

The transistor dimensions deemed to possess the most desireable functional characteristics are displayed in Table IV-2. The transistors described in the table, correspond to
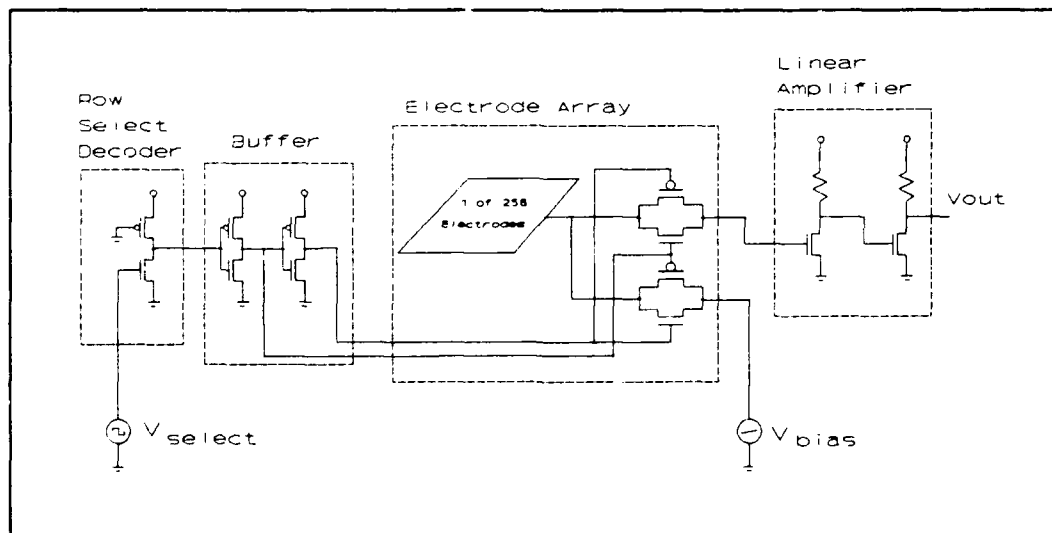
Figure IV-7. Schematic of SPICE simulated array control circuitry.

each transistor illustrated in Figure IV-7. The decoder was
obtained from AFIT's CAD standard cell library, and was,
therefore, not redesigned. The decoder's transistor sizes
used for the SPICE simulation are also included in the Table
IV-2.

Table IV-2. Transistor dimensions for the tactile sensor
circuitry.

Circuit	Type	Gate Length (μm)	Gate Width (μm)
Driver	n	6	10
	p	6	20
Electrode	n	3	8
	p	3	16
Amplifier	n	4	12
Decoder	p	2	4
	n	2	30

Figure IV-8 shows the SPICE output model for a 5 V_{p-p}
sinusoidal voltage applied to one electrode (channel) of the
designed circuit. Four signals are identified in the
Figure: a clock signal, the sinusoidal signal before and
after the analog transmission gate, and the amplifier output
signal. For the transistor dimensions used, the degree of
signal distortion through the analog transmission gate is
minimal, and the MOSFET amplifier's output exhibits the
desired characteristics. Additional simulations, using
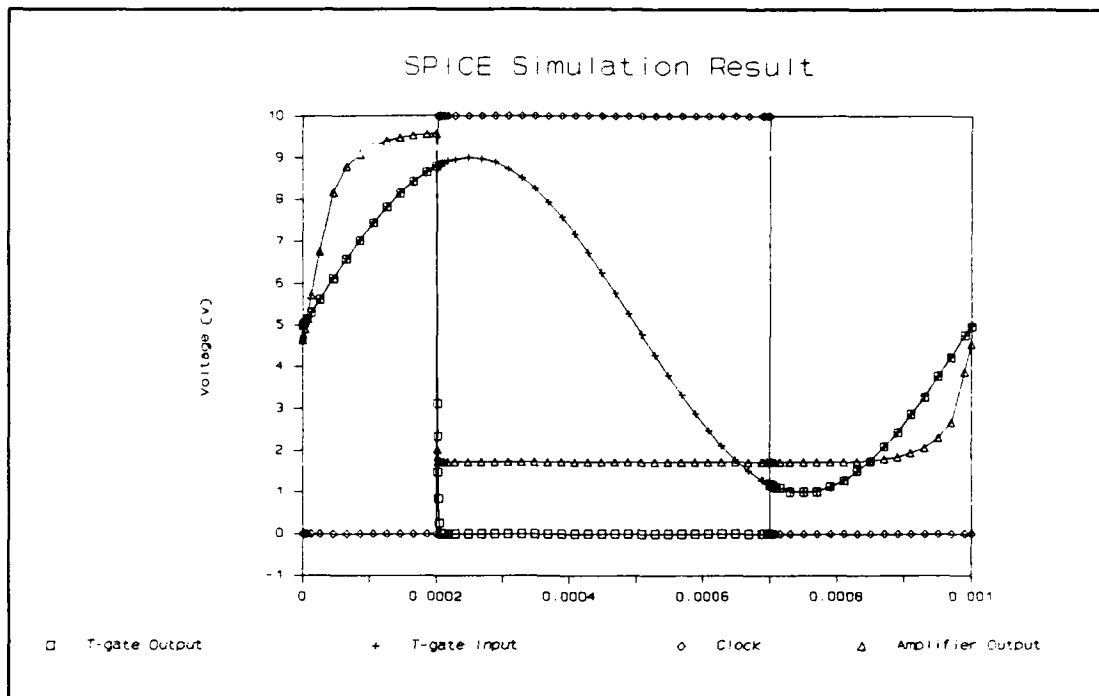
Figure IV-8. SPICE simulation output for the designed 16x16 electrode array control circuitry.

other transistor dimensions, either would not simulate, or would distort the 5 V_{p-p} sinusoidal signal.

Modular Design

The circuit designed for this project incorporated a modular design approach. That is, sufficient flexibility was designed into the circuit, such that if one section of the circuit should malfunction, that section could be selectively removed without loss of the overall experiment.

For instance, should the multiplexer not function as designed, all multiplexer connections to the array could be severed, and this function could be replaced by

corresponding external TTL circuits. Selection of

individual electrodes, via the transmission gates, must

function in order to complete a successful experiment.

MOSIS CIF Submission

The circuit submitted for fabrication is shown in

Figure IV-9. The 16x16 electrode array encompasses the vast

majority of the surface area of the IC. The clock and

associated control circuitry are located in the lower left

corner of the figure. Surrounding three sides of the

electrode array are alignment pads, enabling alignment of a

weighted test probe over a single electrode when the array

is covered with the PVDF film.

Test Probe

Properly characterizing the PVDF tactile sensor's

sensitivity to load and pattern resolution capabilities,

required loads ranging from 1 g to 100 g using a variety of

test shapes. Since one electrode is 250x250 μm square, a

more elaborate probe alignment tool was deemed necessary

(compared to that used in the previous thesis) [2:3-10].

While the same Micromanipulator IC microprobe alignment arm

was used, a triangular metal block (one edge resting

slightly against the alignment arm) was affixed to the
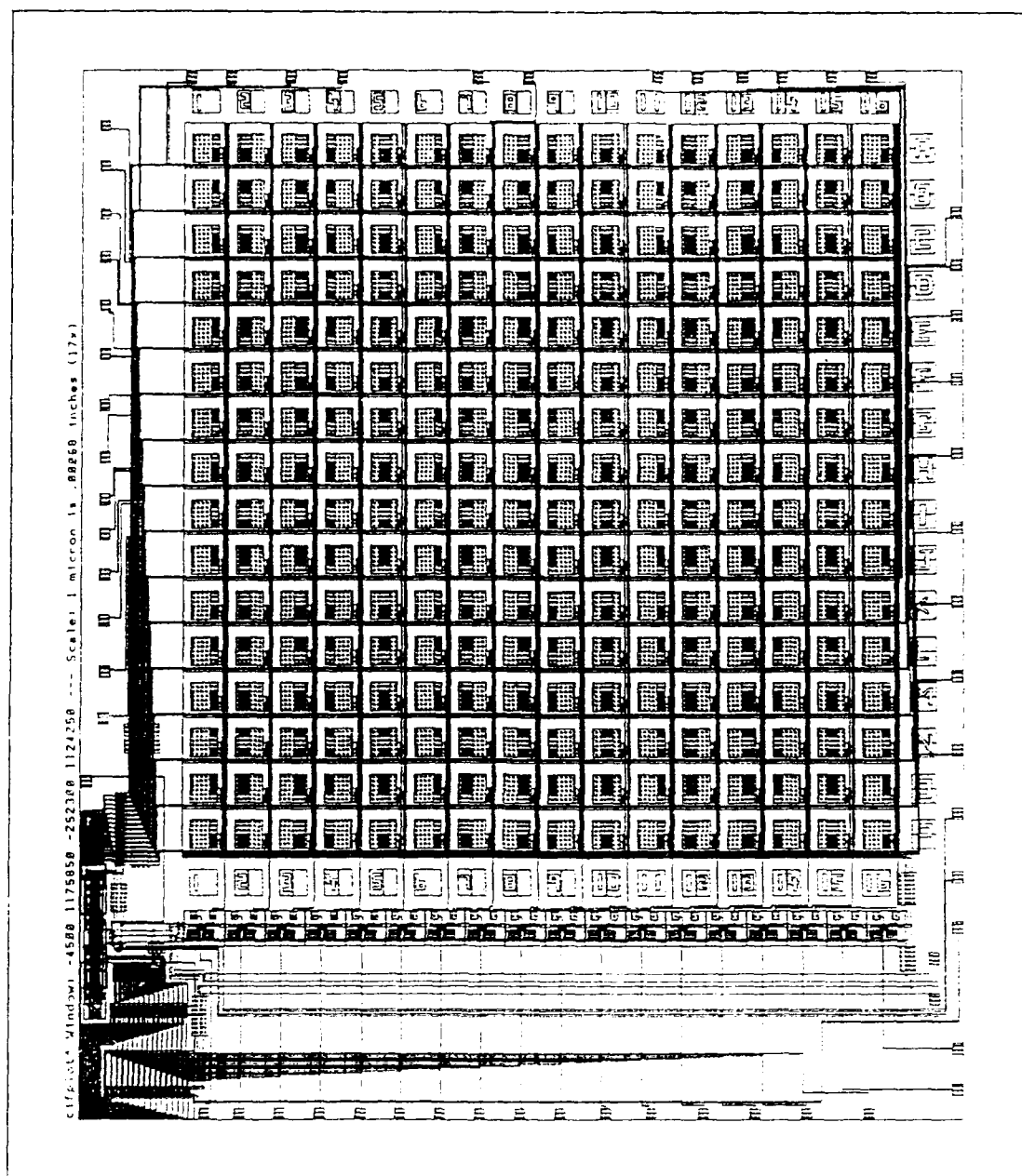
Figure IV-9. Caltech Intermediate Form (CIF) plot of the designed circuit.

subassembly. This prevented lateral movement, so the probe arm could only move in the vertical direction. Lateral adjustment was accomplished by adjustment screws in the base of the alignment arm.

A probe assembly and weights were also designed, which easily attach to the microprobe alignment arm. A total of four probe arms were designed. Three of the probe arms had square tips, and they were designed to cover one, four, and nine electrodes. The fourth probe was threaded to accommodate the various shapes: round, toroidal, hexagonal, and rectangular. In addition, a complete set of weights (10, 25, and 50 g) was designed in order to obtain any weight within the required range of 1 g to 100 g. The drawings for the probe arm and attachments are shown in Appendix C.

Test Protoboard

An IC protoboard was used extensively during the IC performance evaluation as a means to supply and receive signals. Referring to the pinout diagram of the fabricated IC (Figure IV-10), V_{dd} was applied to pins 18 and 59, while electrical ground was connected to pins 17 and 58. The clock signal was input to pin 61, system reset was assigned pin 62, the PVDF film bias was connected to pin 63, and the array's multiplexed output signal was taken from pin 60.
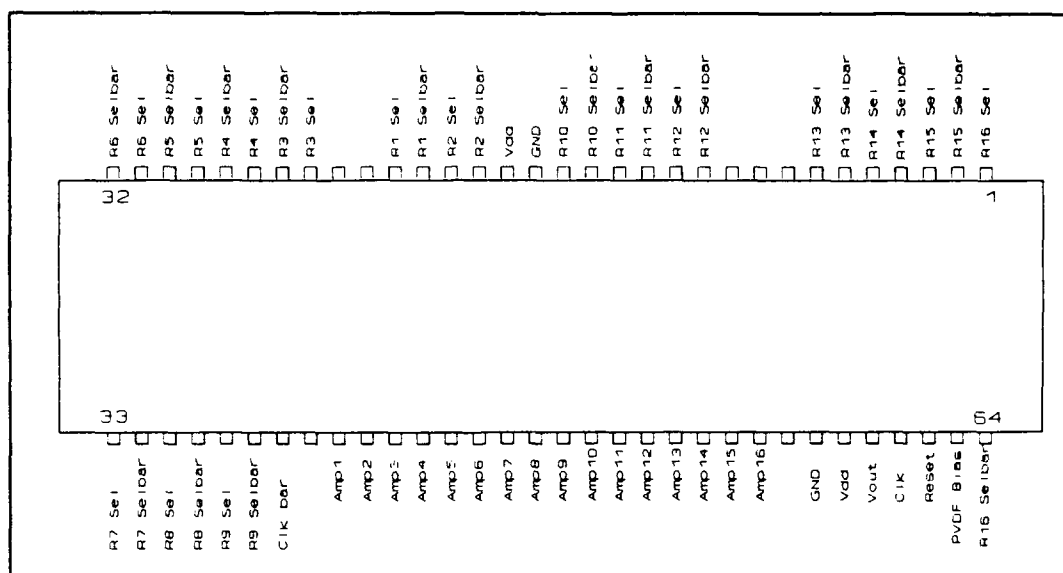
Figure IV-10. Pinout diagram of the fabricated IC.

In the event of circuit malfunction, several IC pins were available for use as external control inputs to the electrode array. For example, pin 7 (R13 Sel) and pin 8 (R13 Selbar) input the controlling voltages necessary for selection (or non-selection) of Row 13. Pin 41 (Amp1) provided a discrete output connection for the first column's MOSFET amplifier.

PVDF Film Preparation

A method of preparing the PVDF film for use on the tactile sensor was developed. The PVDF film used in this thesis varied in thickness from 25 μm to 110 μm, and was either metalized or unmetalized on both surfaces. In

addition, the film had to be cut into squares which covered

the entire electrode array (0.65 mm x 0.65 mm).

Since the PVDF film must be unmetalized on one surface

(the surface contacting the array), a means to either

deposit a thin metal film on the unmetalized PVDF, or to

remove the metal from one side of the metalized film, was

developed. The evaporation of aluminum onto the unmetalized

PVDF film yields a less than satisfactory result [10:6.2].

Therefore, removal of the aluminum from one of the metalized

surfaces was accomplished.

Prior to metal removal, the polarity of the PVDF film

must be determined. This was accomplished using the

instrumentation configuration shown in Figure IV-11. A

glass microscope slide was partially metalized with aluminum

by thermal evaporation. A sample of PVDF film was attached

to the metalized slide with silver paint. A strip of copper

tape was placed near the PVDF film, parallel to the

metalized/unmetalized border. A 1-mil diameter bond wire

provided an electrical connection between the copper tape

and the top surface of the PVDF film. The V_{source} of an

electrometer was used to supply a voltage potential (2 V) to

one surface of the film. Correspondingly, V_{in} of the

electrometer was connected to the opposite side of the PVDF

film.

Proper orientation of the PVDF film was determined when

the measured voltage was slightly greater than the voltage
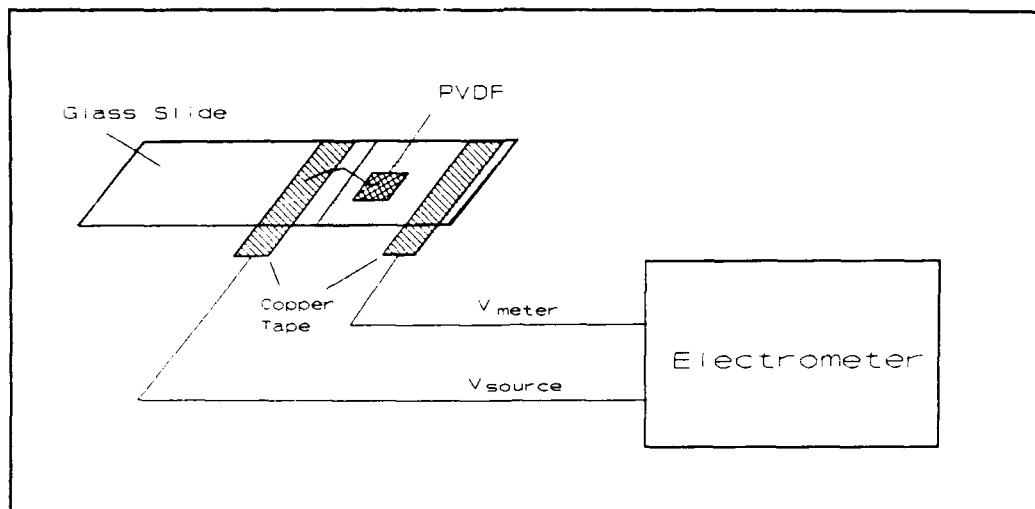
Figure IV-11. Instrumentation configuration for characterizing the PVDF film.

applied ($\approx$ 2.12 V). A mark using indelible ink was placed on the V_{source} side of the PVDF film, indicating that the opposite side must have its aluminum etched.

The procedure used for removing metal from one surface of the metalized PVDF film was:

1) A PVDF sample was placed on a glass slide (marked side down), which has a thin film of isopropyl alcohol on its surface. The alcohol helps prevent the film from moving.

2) The PVDF film's surface was gently rubbed with a cotton swab dipped in concentrated ferric chloride; care was taken not to etch beyond the film's border. A noticeable discoloration of the film occurs when the metal is removed. Finally, the film was thoroughly rinsed in deionized water to remove the remaining ferric chloride, and then it was dried with nitrogen.

3) A grid of squares, with each square slightly larger than the electrode array, was drawn on a piece of paper. A drop (or two) of isopropyl alcohol was used to attach the paper to the PVDF film, ensuring that the grid covered the etched area of the film.

4) A glass slide was then placed over, and aligned with the grid lines. Using the slide as a straight edge, the film was cut into 0.65 mm squares. The PVDF film squares were then stored for later use.

Tactile Sensor Fabrication

Upon completion of the PVDF film characterization, the film was then attached to the microchip's electrode array, forming a tactile sensor. Several different types of nonconductive adhesives were evaluated including acrylic, silicon, urethane, and others, as discussed in Chapter V. Fabrication of the tactile sensor was accomplished using the following procedures:

1) One drop of adhesive was applied to the surface of the electrode array using a 3 cc syringe. One drop provides sufficient adhesive to cover approximately 3/4 of the electrode's surface area (centered at the midpoint of the array). The adhesive flows over the complete array when th PVDF film is applied.

2) A thin film of cellophane ($\approx$25 μm thick) was then applied over the PVDF film to assist the PVDF film in conforming to the topography of the electrode array. Silicon oil was used to coat the surface to prevent bonding between the cellophane and any excess adhesive oozing from beneath the PVDF film.

3) A glass square was then positioned over the cellophane sheet, centered on the electrode array, and compressed using a metal binding clip. The glass square was cut from a glass microscope slide (using a diamond scribe), each side having a length of 0.7 mm. The metal binding clip was carefully centered over the glass slide so that equal pressure was applied over the surface of the glass square.

The complete assembly is displayed in Figure IV-12. The binder clip exerts pressure onto the glass square. The pressure is then transferred through the square, and onto the cellophane and PVDF film. This arrangement compresses the PVDF film onto the electrode array, ensuring uniform conformity to the electrode array's surface.

4) A 1-mil diameter wire, bonded to Pin 2 (within the cavity of the IC package), provided the electrically conductive path between the external bias circuits and the metalized surface of the PVDF film. Silver paint was used to connect the wire onto the surface of the PVDF film.
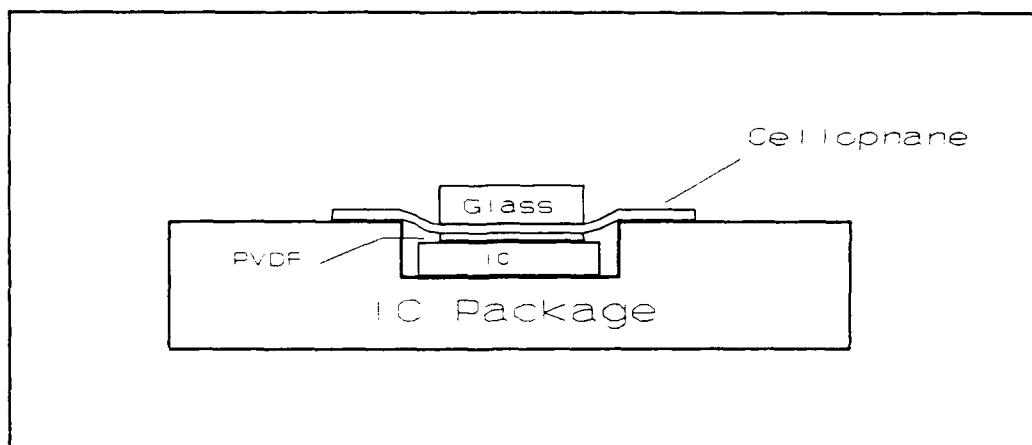
Figure IV-12. Coupling the PVDF film to the electrode array using the compression block technique.

2. Performance Evaluation Procedures

A performance evaluation plan was designed to provide a logical set of procedures which evaluates all aspects of the PVDF tactile sensor. While this philosophy was maintained throughout the entire testing phase of this project, technical problems forced the implementation of a "real time" test plan. Therefore, the tests discussed below reflect the sequence of events leading to the performance evaluation of a multiplexed tactile sensor.

16x16 Electrode Array IC Performance Evaluation Procedure

Performance evaluation of the integrated circuit was composed of two separate subtests. The first test entailed

characterizing the linear MOSFET amplifiers. The second subtest evaluated the functional and operating properties of the multiplexing control circuits. It should be noted that prior to the application of power to the IC, a 10 KΩ resistor was placed in series between the source and the $+V_{dd}$ input to the IC. Then V_{dd} was slowly increased to the operating voltage. This action slowly discharged any residual static charge residing within the chip, preventing any potential power-up damage.

MOSFET Amplifiers. Testing the amplifiers was accomplished in two steps. The first evaluation measured the resistor values using the electrometer, and the second determined the DC operating characteristics using the semiconductor parameter analyzer.

The amplifier resistors were evaluated using the instrumentation configuration shown in Figure IV-13. With the Keithley Model 617 electrometer on the "ohms" setting, one probe was placed on the V_{dd} electrode, while the second probe was placed on the test pad corresponding to the resistor under test. Several resistors from numerous IC's were tested to ensure uniform results.

The entire MOSFET amplifier was characterized using the Hewlett Packard Model HP 4145A Semiconductor Parameter Analyzer. The instrumentation configuration for the amplifier test is shown in Figure IV-14. The HP 4145A controls were adjusted so that the transistor gate voltage
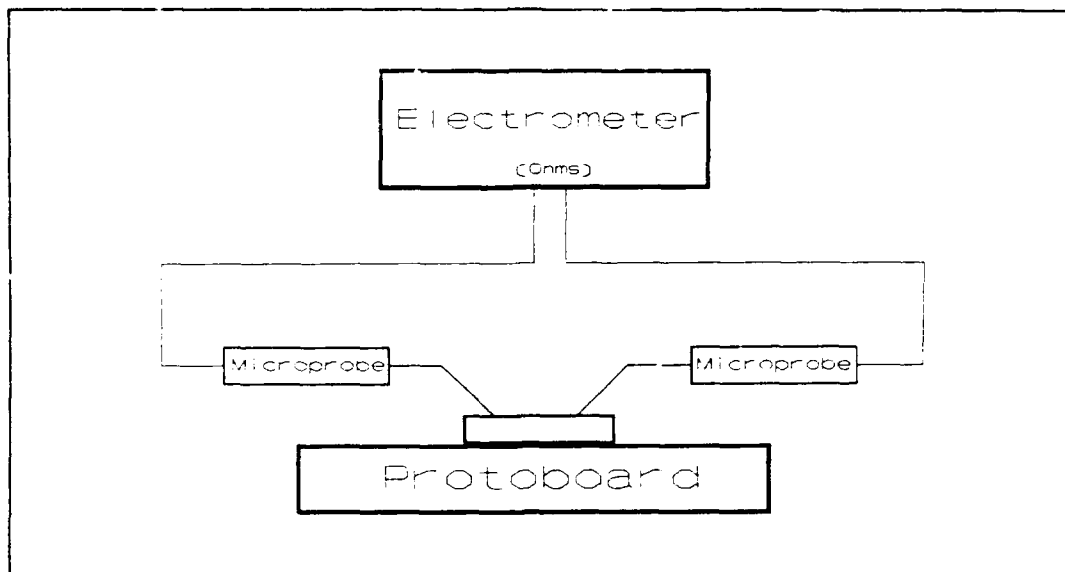
Figure IV-13. Instrumentation configuration for the MOSFET amplifier resistor tests.
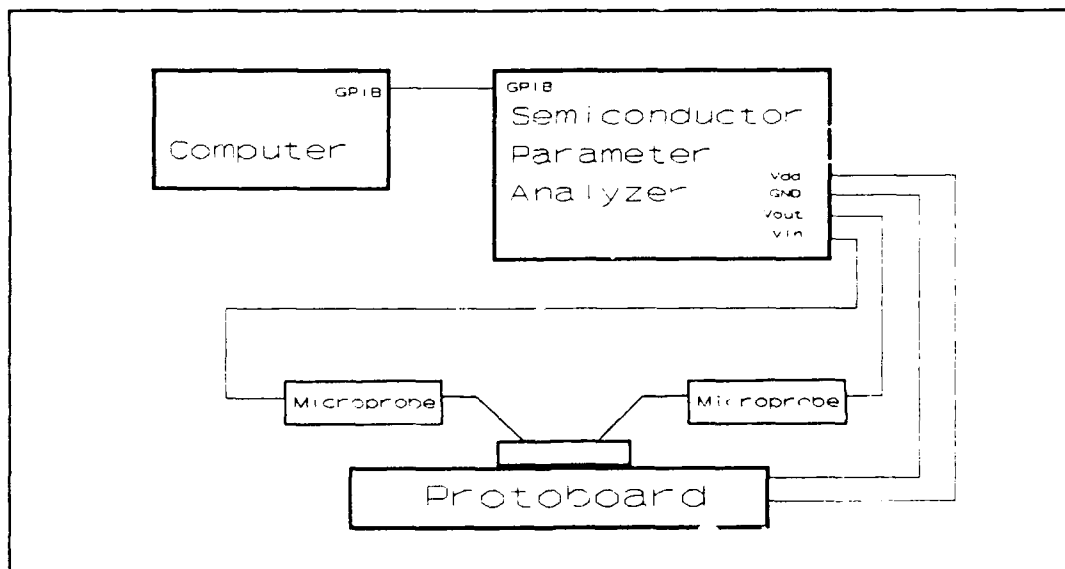
Figure IV-14. Instrumentation configuration for the MOSFET amplifier tests.

swept the entire supply voltage range of 10 V. The computer

program used to transfer the display graphic from the

HP 4145A to the Zenith 248 PC (via the GPIB interface) is

summarized in Appendix E.

Multiplexing Circuit. Once the basic amplifier

operating characteristics were known, the second series of

performance evaluations were initiated. The multiplexing

circuit, which controls the scanning of the electrode array,

was evaluated in two steps. Implementation of the first

step ensured proper sequencing of the electrode array, while

the second step measured the degree of isolation between

electrodes.

The instrumentation configuration used to determine the

control voltage characteristics of the circuitry is shown in

Figure IV-15. The digital oscilloscope (with high impedance

probe) measured the controlling voltage signals.

In general, verification of proper row control circuit

operation was accomplished by observing the oscilloscope

display for the appropriate control signal timing pulses.

A 256 Hz clock signal was input into the circuit. The

oscilloscope's timebase was set to 103 ms/div. This timing

configuration, divided the oscilloscope's display into 16

sections, each section corresponding to one electrode array

row. Placing the oscilloscope's probe on an appropriate

"Row Select" bonding pad surrounding the IC (See Figure
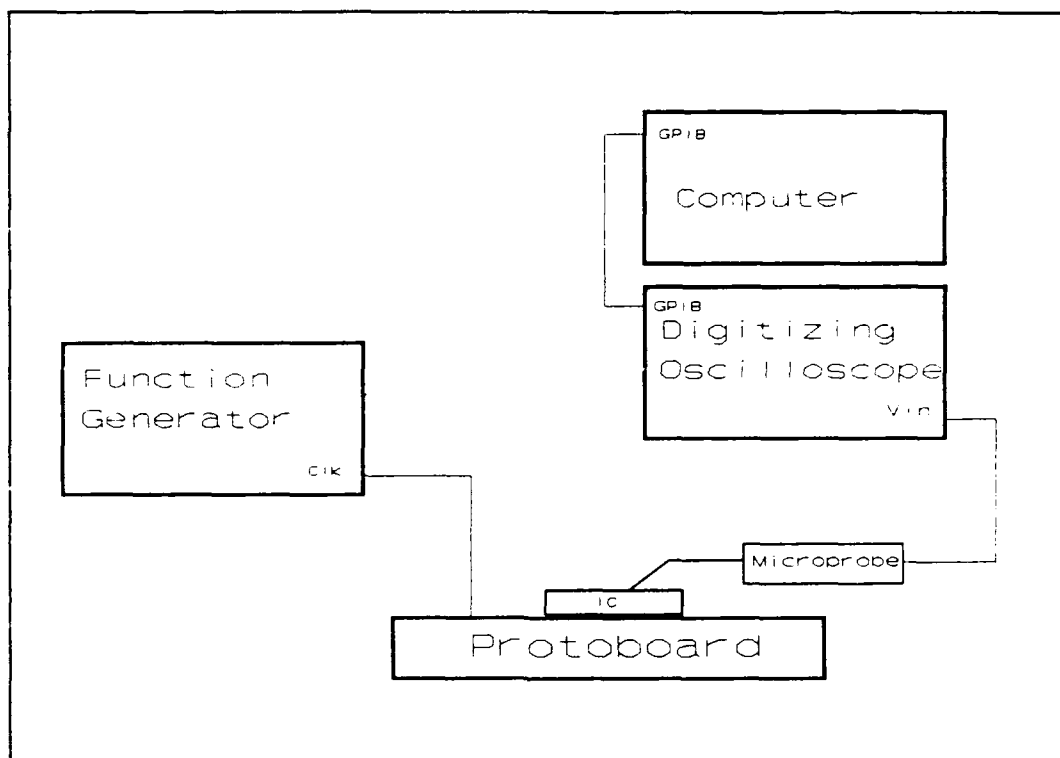
Figure IV-15.   Instrumentation configuration for the
control circuitry tests.

IV-9), produced a voltage pulse indicating proper timing of

the row control circuitry.   Proper timing of the row select

circuitry was determined by: 1) verifying the proper

selection sequence, and 2) ensuring the time duration of

each selected row was correct.

Verification of the column select circuitry performance

was accomplished by applying a 5 V potential to the input of

a MOSFET amplifier and observing the response on the

digitizing oscilloscope (HP 54100).   As the oscilloscope

timebase was set to scan the amplifier bank outputs, a

distinct pulse would occur at the site of the appropriate

amplifier.   The location and duration of this pulse was

recorded and compared to ensure proper operation. This procedure was repeated for each of the 16 amplifiers.

At this point, characterization of the control circuitry ceased. Only one IC was found to be functioning properly, only to be lost (permanently) due to a static discharge. No other IC was found to function properly with any degree of regularity. Systematic troubleshooting provided no satisfactory solutions as to why the control circuitry failed.

Modified 16x16 Electrode Array Circuit

Because of the modular design approach used in the design of the integrated circuit, a major modification was incorporated so that the experimental process could proceed. Specifically, all conducting paths leading from the row select circuitry to the electrode array were severed using a Micromanipulator Ultrasonic Cutter (an accessory of the Micromanipulator probing station), thereby isolating the array from any CMOS control circuitry. A replacement TTL circuit was then fabricated using an equivalent design. The TTL control circuitry was realized using two, 4-bit counters (74161), one, 4x16 decoder (74154), one, 2-input NAND gate (7426) IC, one, 2-input NOR gate IC (7428), and three, hex inverter (7404) integrated circuits. A block diagram for the completed circuit is shown in Figure IV-16.
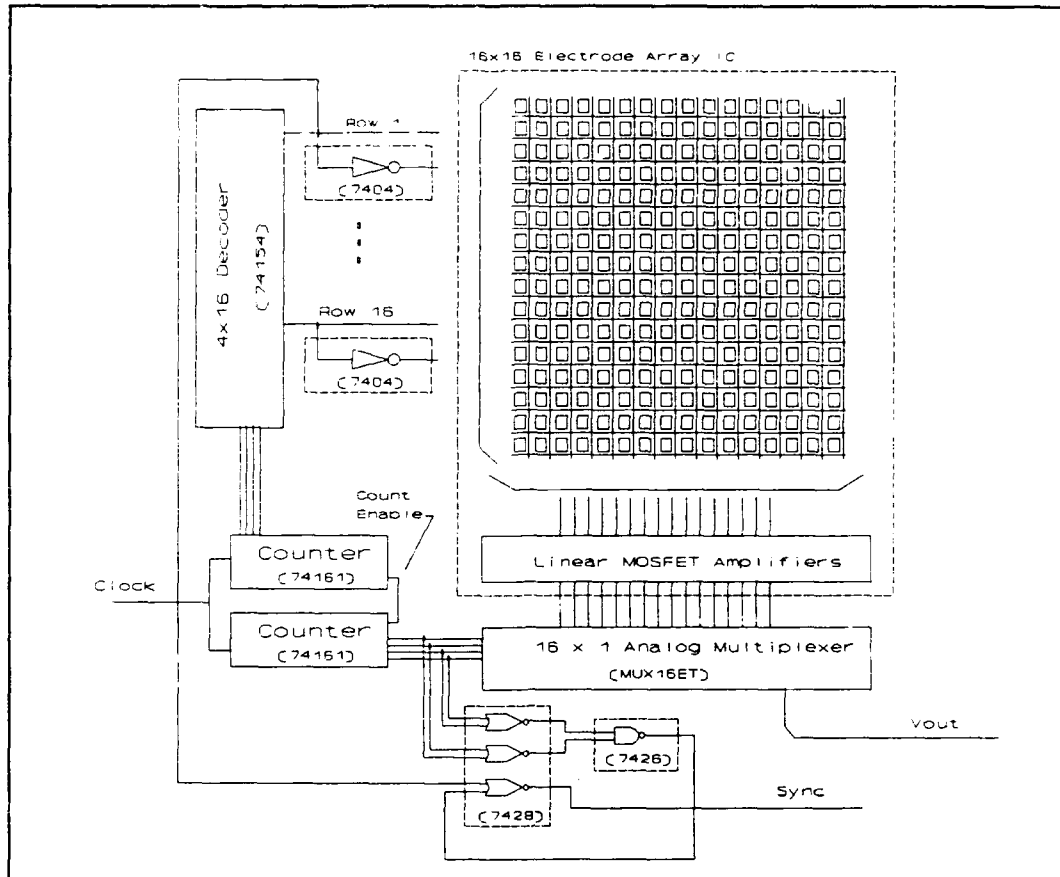
Figure IV-16. Block diagram of the equivalent TTL controlling circuitry.

The TTL row select circuitry was coupled to external pins on the IC since the electrode array was still useable. In addition, the MOSFET amplifier outputs were directly coupled to the external 16x1 FET analog multiplexer.

Evaluating the extent of isolation between electrodes was accomplished using two micromanipulator probes, as shown in Figure IV-17. One probe carried a voltage potential ranging between 0 and V_{dd}, and it was positioned on a "selected" electrode. The second probe was connected was moved sequentially to the remaining nearest neighbor
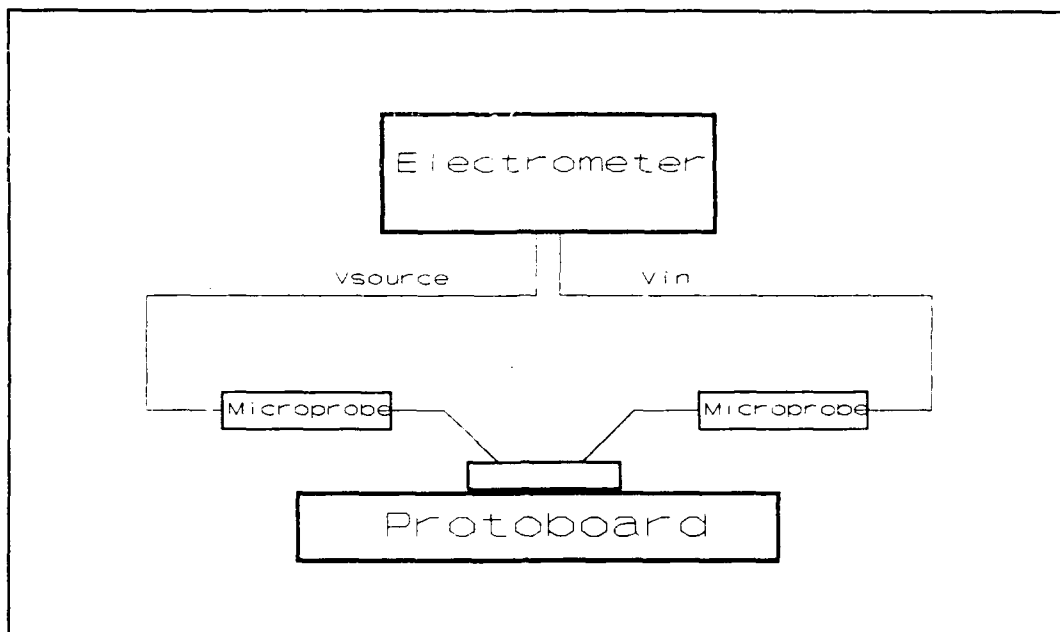
Figure IV-17. Instrumentation configuration used to measure the electrode crosstalk.

electrodes. The electrometer display was observed to ensure that no crosstalk occurred between electrodes.

A voltage potential was then connected to the PVDF film bias electrode (pin 63 in Figure IV-9), and a probe was used to contact the surface of a "selected" electrode. The voltage was then increased from 0 to V_{dd}, to ensure there was no change in the measured voltage on the "selected" electrode. This measurement determined the maximum value of PVDF film initialization/bias voltage which could be applied to the array circuit.

Charge Coupling. Once characterization of the TTL control circuitry was completed, coupling the PVDF film to the electrode array was accomplished. This process involved a two-step procedure.

The first process entailed coupling the output of a biased piece of PVDF film to the electrode array to ensure proper piezoelectric behavior. The instrumentation configuration illustrated in Figure IV-18 was used to accomplish this test.
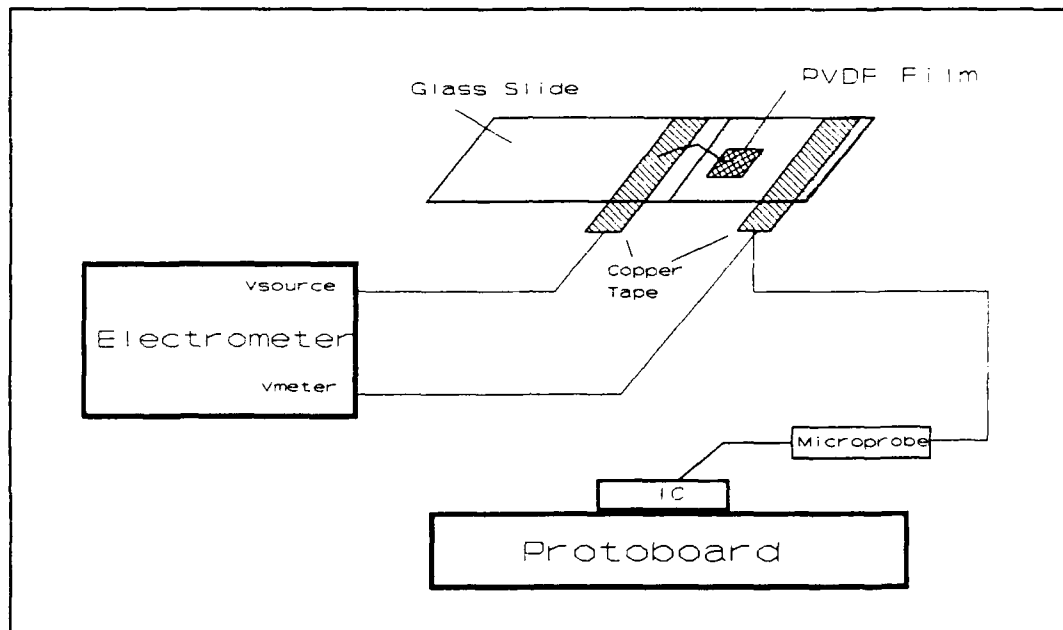
Figure IV-18. Method used to probe and couple the PVDF film to the electrode array.

With a bias voltage ranging between 0-10 V applied to the top surface of a PVDF film square, a second probe was used to transport the charge from the film's lower surface to a pad in the electrode array. When the probe touched the surface of a "selected" electrode, ideally, no charge would be lost. However, in this experiment, the stored charge immediately dropped to zero, indicating a serious circuit

anomaly. An explanation of this behavior will be discussed in Chapter 5.

Failure of this one test alone, guaranteed that the array circuit configuration designed for this project, would not produce a functioning tactile sensor. At this point, all testing of the designed circuit ceased. To show that the basic philosophy of constructing a multiplexed tactile sensor was valid, further experimentation was accomplished using the 5x5 electrode array tactile sensor designed by Capt Reston [2].

Multiplexed 5x5 Array

As previously mentioned, each of the 25 electrodes on Reston's design served as a direct input to the gate contact of a linear MOSFET amplifier. The pinout diagram for the IC is displayed in Figure IV-19. External TTL circuits were used to convert the MOSFET amplifier outputs into a time division multiplexed signal train.

The TTL design employed is shown in Figure IV-20. This is the same basic design that is shown in Figure IV-16. This circuit, however, couples the output of each MOSFET amplifier directly to an input of an analog multiplexer. The additional multiplexer was necessary since each multiplexer can have only sixteen analog inputs.
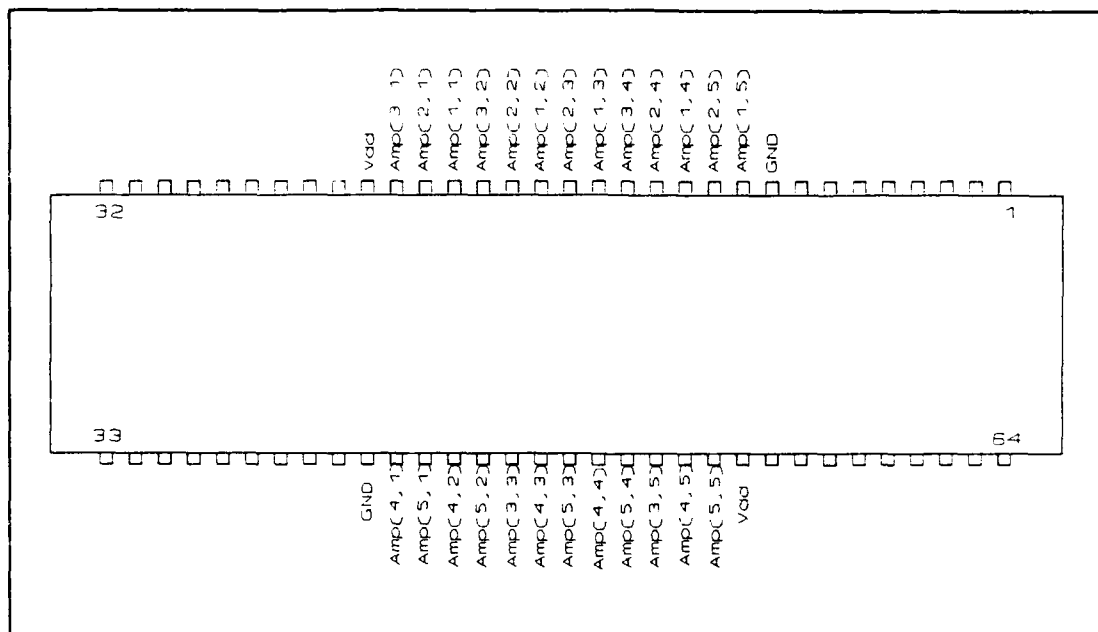
Figure IV-19. Pinout diagram of the 5x5 electrode array IC.

A combinational logic circuit also provided the synchronization (trigger) pulse to the digitizing oscilloscope. A logic 1 occurred whenever the electrode in the top left corner was selected, otherwise the output was a logic "0".

Three separate voltage sources were necessary to ensure proper circuit operation. Operation of the TTL circuit was limited to a maximum of 5 V. The MOSFET amplifiers used in the 5x5 array circuit were previously characterized for a 10 V bias [2], and the two analog multiplexers required a supply voltage of 15 V, to provide a linear output.

Testing the TTL control circuitry was accomplished by inserting a 5 V potential on one electrode. The two multiplexer outputs were displayed on the digitizing
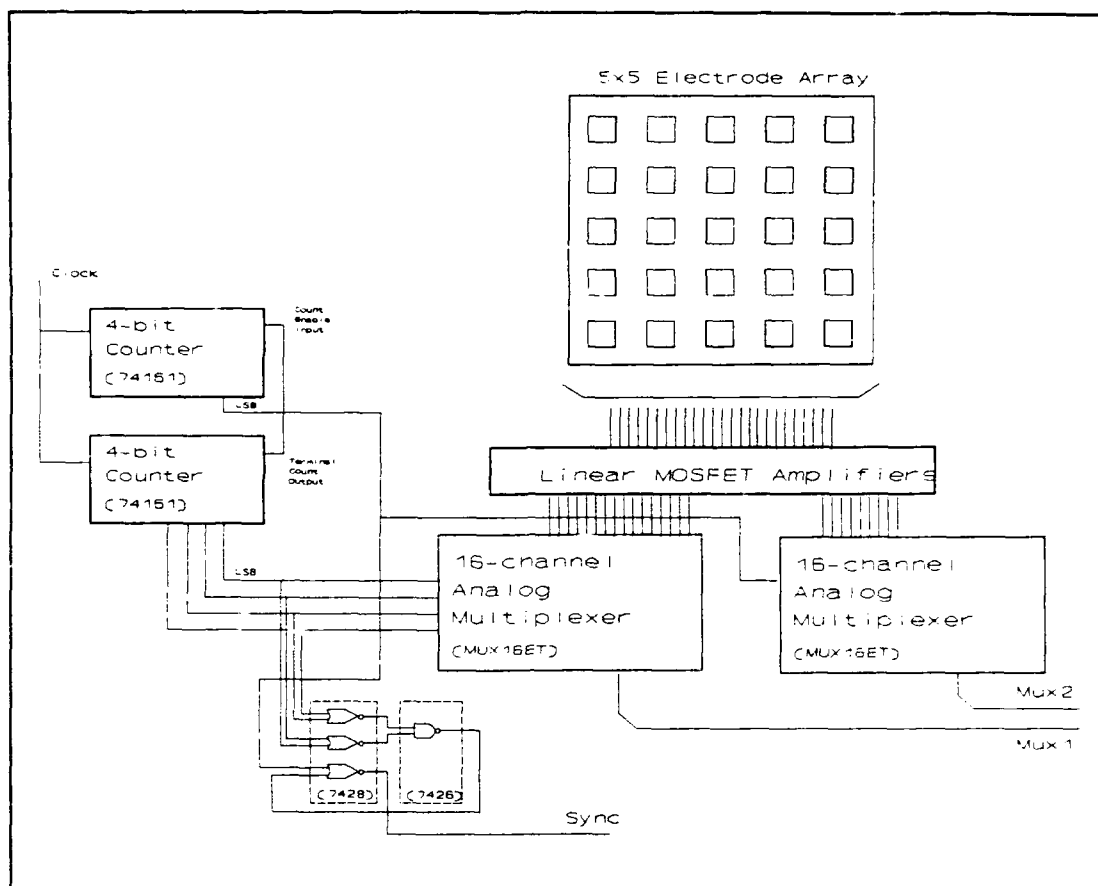
Figure IV-20. Multiplexed 5x5 electrode array.

oscilloscope. With the timebase adjusted such that the response of the 25 electrodes could be displayed, a 5 V input signal was used to differentiate the electrode under test from the remaining 24. All 25 electrodes were tested in this fashion.

Multiplexed 5x5 Electrode Tactile Sensor

Fabrication of the 5x5 tactile sensor followed the procedures described in the section entitled "Tactile Sensor

Fabrication." The fabricated sensor was then inserted in a protoboard which contained the supplementary TTL multiplexing circuit. Biasing the amplifiers into their linear region was accomplished by applying a 5 V potential to the metalized surface of the PVDF film. A second voltage potential was momentarily applied to each amplifier input, as discussed in Chapter V. This voltage served to "precharge" each amplifier, thereby establishing a nearly uniform charge over then entire 5x5 array.

Individual Electrode Response. This test characterized the voltage generated by the PVDF film when a load was applied. A weighted probe (with contacting surface area equal to that of one electrode) was positioned over a single electrode. The probe, containing a range of weights ranging between 5 g and 100 g, was slowly lowered onto the electrode. The voltage gen ated by the PVDF film was then recorded. In addition, the voltage on neighboring electrodes was also measured to determine the degree of coupling between electrodes.

Data Acquisition and Reduction

Data Acquisition. The instrumentation configuration used to acquire data for this circuit is shown in Figure IV-21. The BASIC computer program code (HPOSC1A.BAS), listed in Appendix E, was used to acquire the sensor's

response as displayed on the digital storage oscilloscope.
The program was written such that each time the program was
executed, the array would be scanned, and the individual
electrode responses would be averaged eight times. This
averaging technique tended to reduce the inherent noise, and
it yielded a more uniform response.
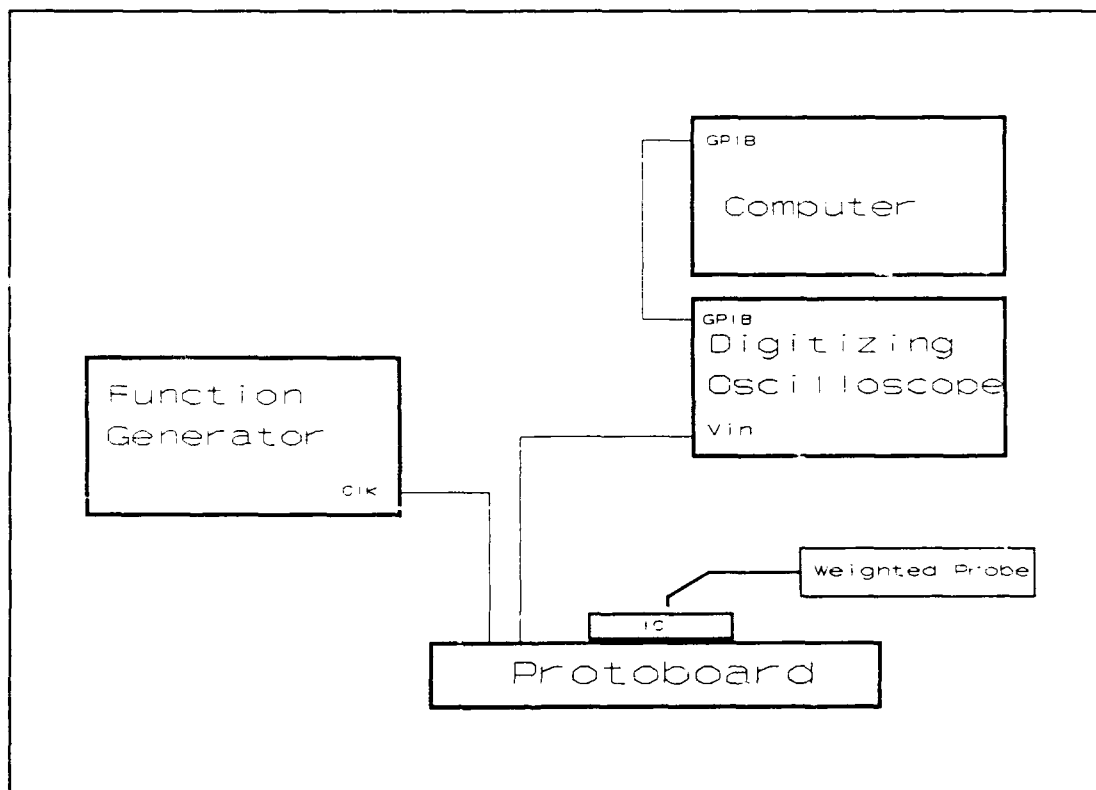
Figure IV-21.   Instrumentation configuration for evaluating
the performance of the 5x5 multiplexed tactile sensor IC.

Testing the fabricated tactile sensor required scanning
the sensor's response twice for each load that was applied.
The first scan occurred following the application of a
uniform bias, and thus, a reference level was established

with which further PVDF film tests could be compared. The second scan occurred following the load's application and attainment of a stabilized response.

Data Reduction. The format of the data collected using the computer program (HPOSC1A.BAS) was organized in an array of time versus voltage responses. To obtain the three-dimensional representation of an object under test, required that the data be transformed into the form of position versus voltage. The BASIC computer program listed in Appendix E (CONVERT.BAS) satisfies this requirement.

Computing the difference between the load and no load conditions tended to reduce the effect of the variations between the initial charge states between the sensor electrodes. This manipulation produced a "corrected" representation of an applied shape. Normalizing this "corrected response" permitted subsequent tests to be compared on a common basis. The BASIC computer program code listed in Appendix E (NORMAL.BAS) performed this function.

The final normalized data file was plotted to produce a three-dimensional representation, which gave a general depiction of the shape under test. Topographical slices through the three-dimensional plot were then made to obtain a more meaningful visualization of the shape under consideration. A mask, scaled to the size and shape of the load under test, was utilized to compare the topographical slices with that of the actual applied load. Using a grid

of squares as a second mask, the areas of the applied load and topographical slices were calculated. When the topographical slice's total area approached that of the applied load, the corresponding voltage value used to construct the slice was recorded. This value was then used as the threshold value for the BASIC computer program code named ARRAY.BAS. This computer code generated a visual representation of the electrode array, indicating the selected (and nonselected) electrodes. By superimposing the topographical slice and mask over the generated electrode array, a recognizable representation of the incident load's shape became apparent.

Summary

This chapter dealt with the basic design goals and considerations which lead to a complete research effort. The techniques for fabricating a PVDF tactile sensor were also discussed. In addition, a description of the test procedures described the chronology of events which led to a tactile sensor configuration that was evaluated. The next chapter discusses the results obtained in this research.

V. Experimental Results

This chapter describes and discusses the results obtained from the experiments conducted. The format follows the same pattern that was developed in Chapter IV. The three main sections of this chapter include the performance evaluation of the originally designed 16x16 electrode array integrated circuit (IC), the modified 16x16 electrode array IC; and finally, the multiplexed 5x5 electrode array IC. A photograph of the 16x16 electrode array IC is displayed in Figure V-1.

16x16 Electrode Array Performance Evaluation

The performance evaluation of the 16x16 electrode array integrated circuit was conducted in two parts. The first part characterized the linear MOSFET amplifiers, while the second part determined the optimal characteristics of the multiplexing circuitry.

MOSFET Amplifiers. The MOSFET amplifiers were characterized using the procedures discussed in Chapter IV; the evaluation was accomplished in two steps.

A total of 40 resistors were measured (eight resistors from five different IC packages). The resistors measured were chosen at random from the entire IC lot (20 die
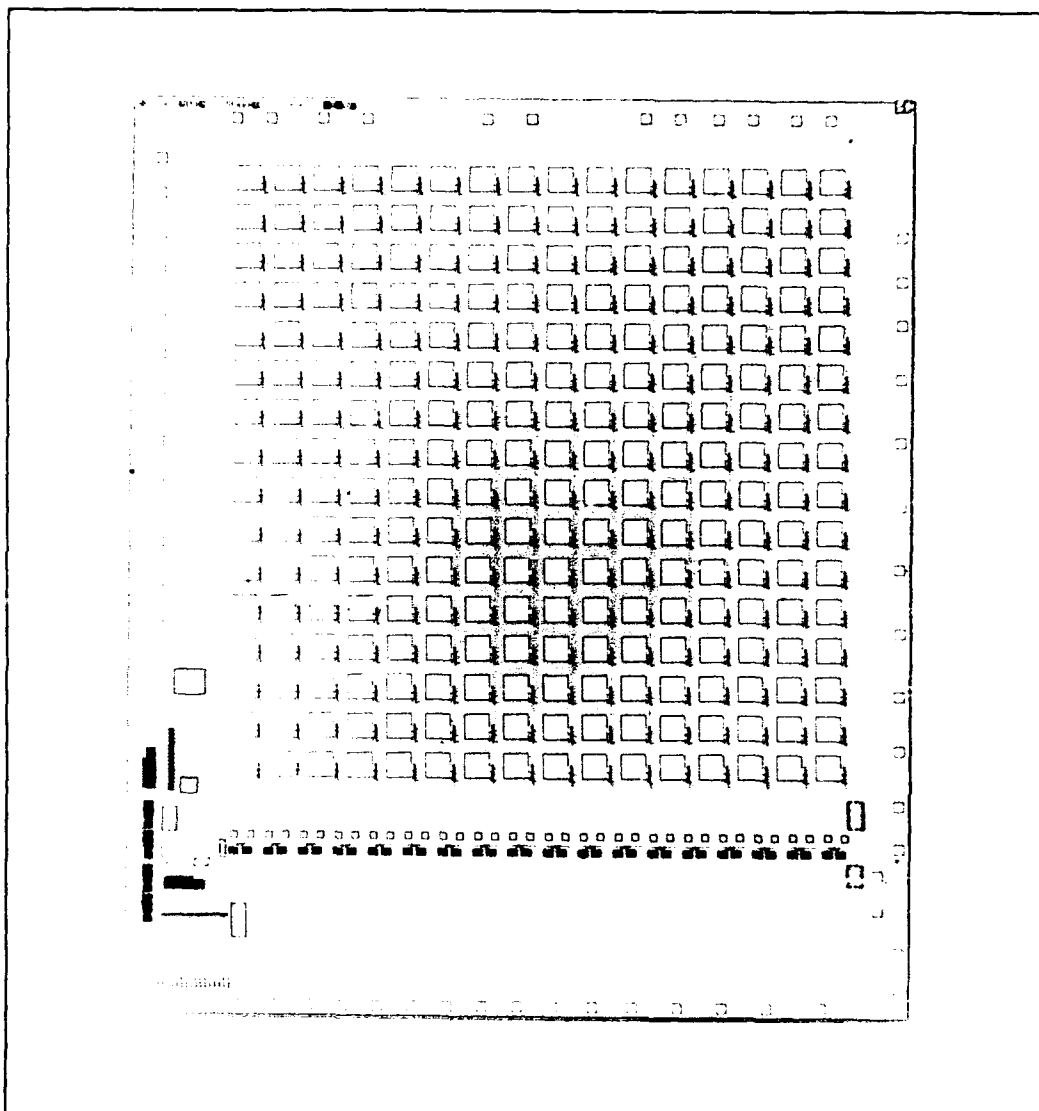
Figure V-1.   Photograph of the MOSIS fabricated 16x16
Electrode Array IC.

pieces). This test verified that the resistors possessed a

uniform ohmic value.

The resistor's average value was calculated to be 4.41

KΩ (standard deviation of 1.38 KΩ) which was slightly lower

than the designed 5 KΩ resistance value.   The serpentine

n-diffusion resistors were designed using a baseline sheet resistance of 20 Ω/square (obtained from the MOSIS specification sheet). A resistor design employing 250 squares should yield a 5 KΩ resistor.

Because each amplifier was composed of two cascaded n-type transistors, the net effect of the smaller resistor values was a shift (toward the right) of the linear region of the amplifier's DC operating characteristic.

Figure V-2 displays the MOSFET·s Spice simulated DC characteristic curve versus a representative sample of an actual DC characteristic curve. Originally, a DC bias of 3.5 V was predicted as necessary to bring the amplifier into the linear portion of the operating curve (based on the Spice analysis). Since the beginning of the linear operating region of the amplifier shifted to 5 V, a minor change in the biasing voltage was implemented to achieve the desired performance. Therefore, no major changes in test procedure was necessary.

Multiplexing Circuit. Significant circuit problems occurred during the performance evaluation of the multiplexing circuit. As previously discussed, testing of the IC was initiated with the row select circuits. With a 1 Hz clock signal applied to the circuit, no synchronized voltage pulse was observed on any of the row select lines. In fact, any pulse that did occur appeared in a purely random fashion.

MOSFET Amplifier
DC Characteristic Curve

□ Spice Model   + Actual Value
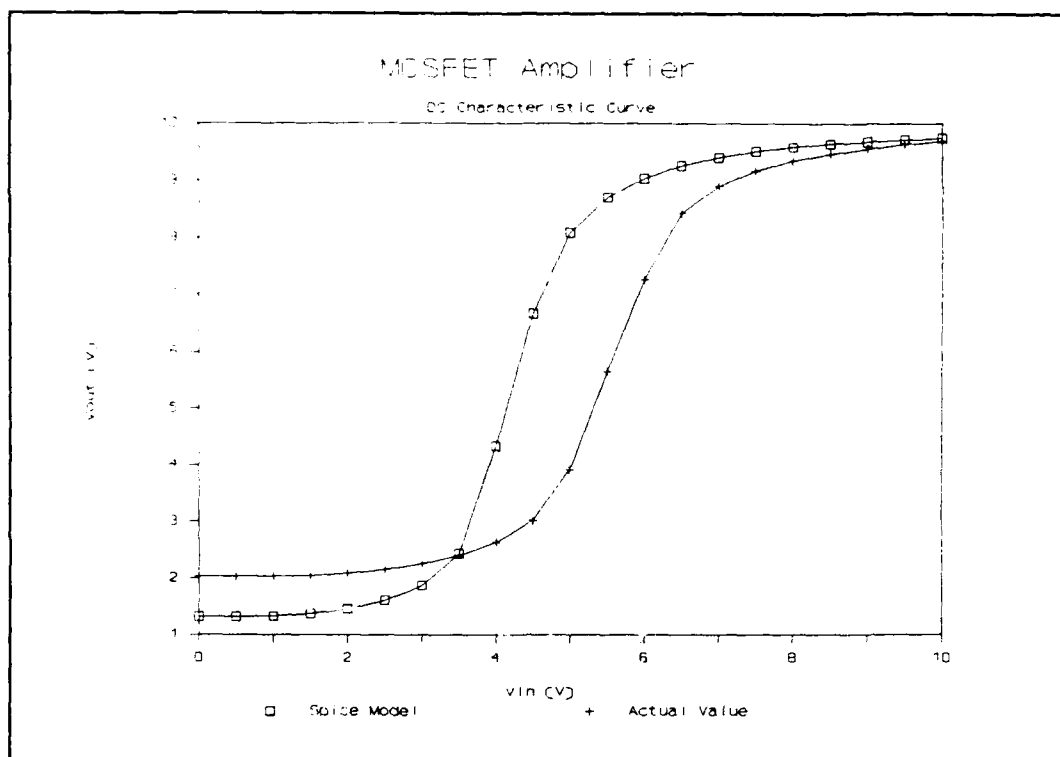
Figure V-2.   Operating characteristics of the MOSFET amplifier.

The signal being measured was one channel of the driver/buffer, which was controlled by the output of the Row Select Decoder. The decoder, in turn, was controlled by the counter circuit. Considering the degree of circuit complexity, the most probable cause of circuit failure resides within either the Row Select Decoder or the row counter circuitry.

Unfortunately, test pads between the decoder and counter were inadvertently neglected in the design submitted for fabrication. This oversight prevented sampling the binary signals between the counter and decoder. An attempt

was made to open a window in the passivating silicon dioxide (SiO_2) layer using the ultrasonic cutter to permit direct probing of the metal conductor residing beneath the SiO_2. However, this procedure did not prove practical. The tornado-like action of the ultrasonic cutter's tip failed to provide an exposed metal surface which could be probed.

Modified 16x16 Electrode Array Circuit

The modular design incorporated in the integrated circuit permitted isolating the electrode array from the defective multiplexing circuit. This action was accomplished by severing all the control lines using the ultrasonic cutter. A photograph of the severed control lines is shown in Figure V-3.

The alternate control circuit utilizing the external TTL ICs was tested using the procedures outlined in Chapter IV, and it functioned as expected. Figure V-4 shows the controlling input pulse to Row #1 of the array. Each row input was characterized in the same fashion, confirming proper row selection.

Three independent tests were implemented to determine the operating characteristics of the modified circuit:

      1)   electrode isolation test,

      2)   electrode array test, and

      3)   charge coupling test.
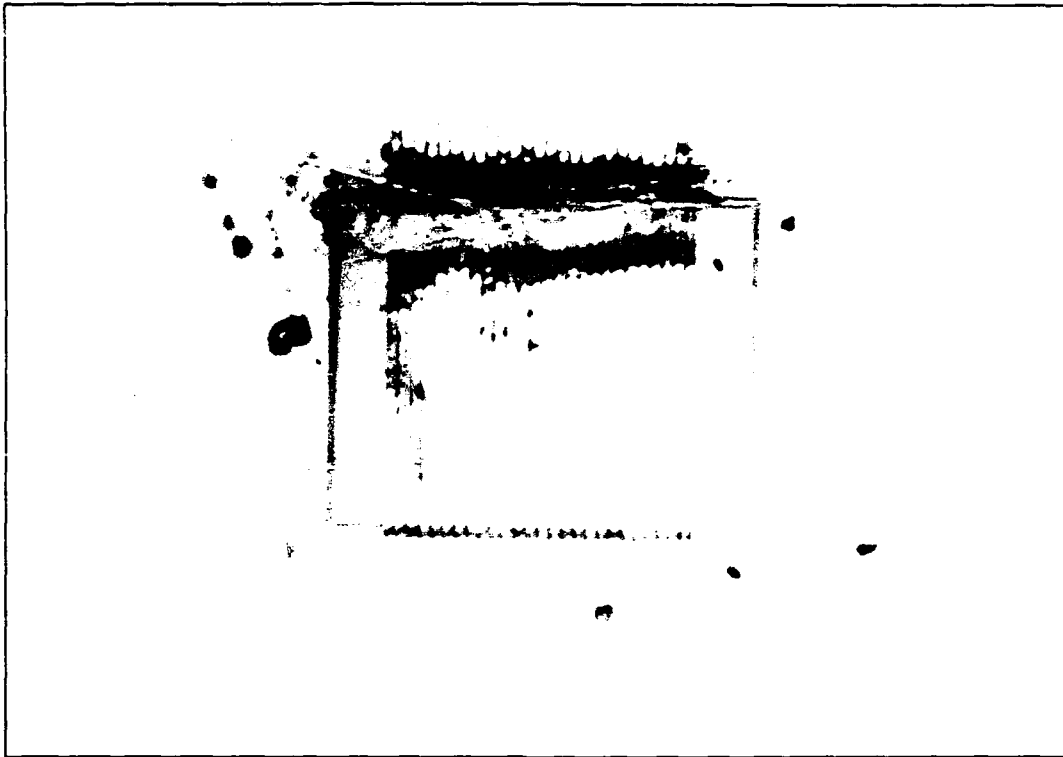
Figure V-3.   Photograph of the severed control lines between the row select circuit and the electrode array.

Electrode Isolation Test.   With the ability to select any one electrode, characterizing the degree of coupling between neighboring electrodes was then accomplished. Following the procedures outlined in Chapter IV, when the measuring probe surveyed a neighboring "non-selected" electrode, only millivolt-level signals were measured, indicating negligible coupling.   The same measurements were taken on the opposite side of the "non-selected" transmission gate (that is, at the floating V_{bias} terminal). A representative sample of the recorded voltage values is displayed in Table V-1.   The applied voltage was
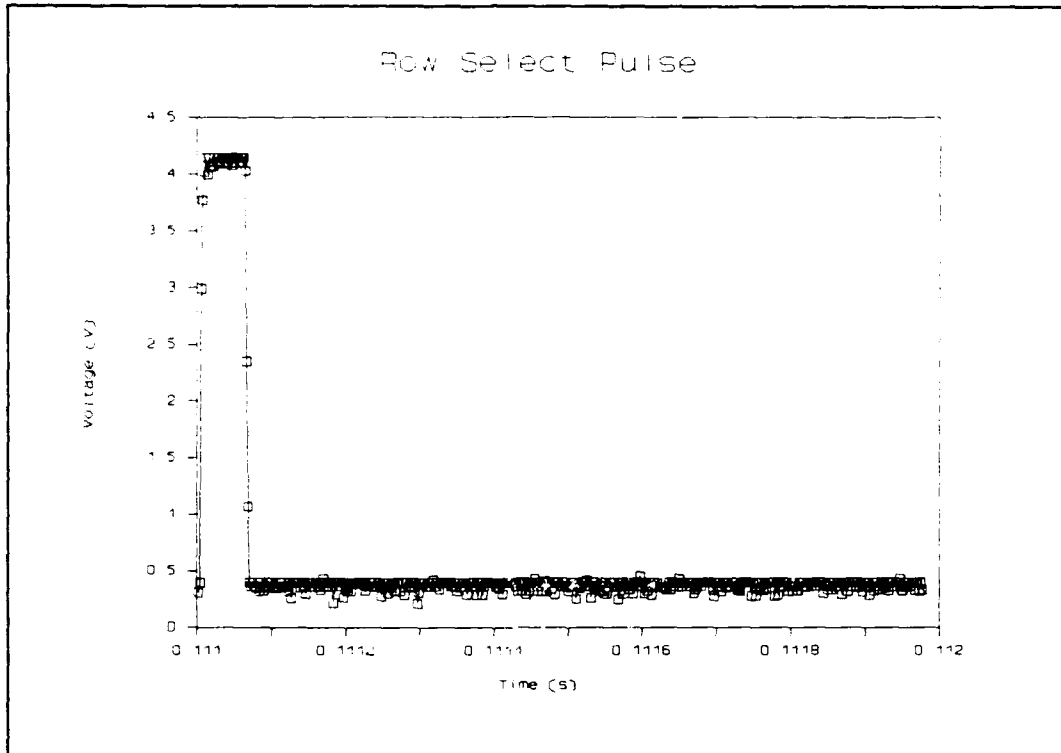
Figure V-4.   Controlling voltage pulse input into electrode array control lines.

incrementally increased until transmission gate breakdown occurred. The second and third columns of Table V-1 reflect the voltages measured at the amplifier and PVDF film bias terminal, respectively. Column 4 indicates the voltage measurements taken from the surrounding electrodes, which essentially possessed the same voltage values as the V_{bias} terminal, as expected. In addition, the voltages occurring at the input to the MOSFET amplifier shows little loss, if any. Once the applied voltage exceeded a certain threshold, transmission gate breakdown occurred. With a $V_{dd} = 5$ V, the transmission gate breakdown occurred at approximately

Table V-1. Electrode Isolation Test.

V(applied)	V(amp)	V(bias)	V(N,S,E,W)*
0	0	-0.31	-0.31
1.0	0.68	-0.31	-0.31
1.15	1.15	-0.31	-0.31
1.25	1.25	-0.31	-0.31
1.50	1.50	-0.30	-0.31
1.60	1.60	+0.17	+0.17
1.75	1.74	+1.70	+1.70

* N,S,E,W refers to the four nearest-neighbor electrodes located to the north, south, east and west positions with respect to the "selected" electrode.

1.60 V. As long as the applied voltage did not exceed this threshold, isolation between the electrodes existed.

When the measurement probe was placed on the "selected" electrode and a voltage spanning 0 - V_{dd} was placed on the PVDF film bias electrode, identical characteristics were measured. This result further indicated that the circuit functioned as designed, provided the applied voltage did not exceed the breakdown threshold of the transmission gate transistors.

Figure V-5 shows the characteristic curve for a single electrode transmission gate. The ultrasonic cutter was used to totally isolate the external circuitry from affecting the measurement. The breakdown for a single, isolated transmission gate occurred at 2.5 V (or 1/2 V_{dd}).
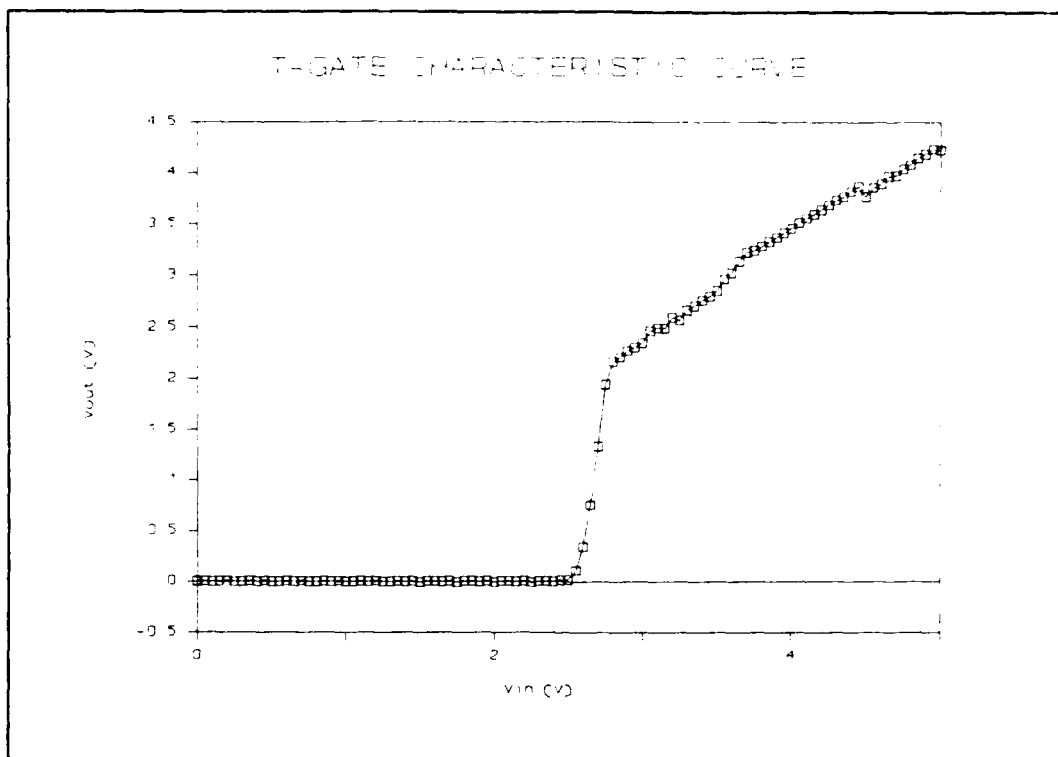
Figure V-5.   Characteristic curve of a transmission gate.

Electrode Array Test.   Figure V-6 depicts the

result when a 5 V potential was applied as the input to

electrode (11,1), the first electrode of the eleventh row.

While the other electrodes maintain a 1 V steady baseline,

an obvious pulse occurs at the site reserved for electrode

(11,1).   This result indicates that no apparent coupling

between electrodes exists.   Similar results were obtained

for the other electrodes selected at random using various

input signals.

Charge Coupling.   Attempting to couple charge from the

PVDF film to the electrode array resulted in the

identification of a serious·problem inherent in the circuit
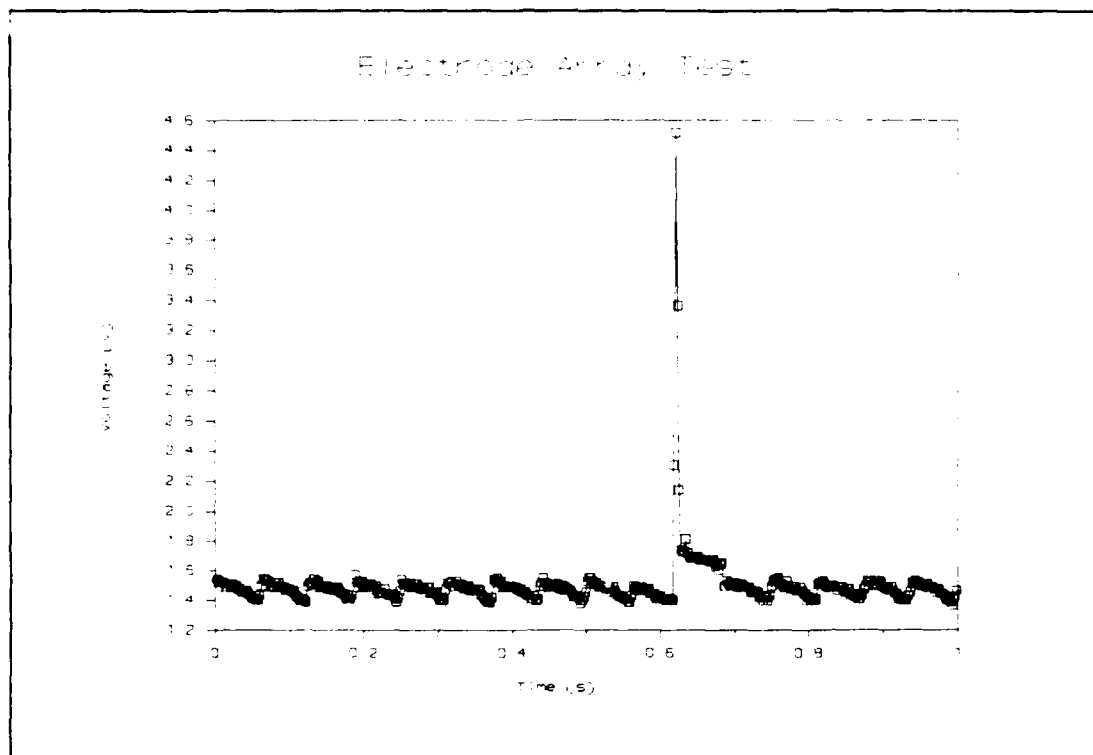
Figure V-6. Multiplexed output signal with a 5 V input applied to the first electrode located in the eleventh row.

design. Following the procedure discussed in Chapter IV, when the "charged" probe contacted the surface of a "selected" electrode, the potential residing on the probe immediately dropped to zero.

A macroscopic view of the circuit of interest is shown in Figure V-7a. The transmission gate coupled to the amplifier is turned-on, while the transmission gate coupled to the PVDF film bias is turned-off. Severing the transmission gate output lines (opposite to the electrode) with the ultrasonic cutter, isolated the electrode and transmission gates from all the other circuitry (line A).
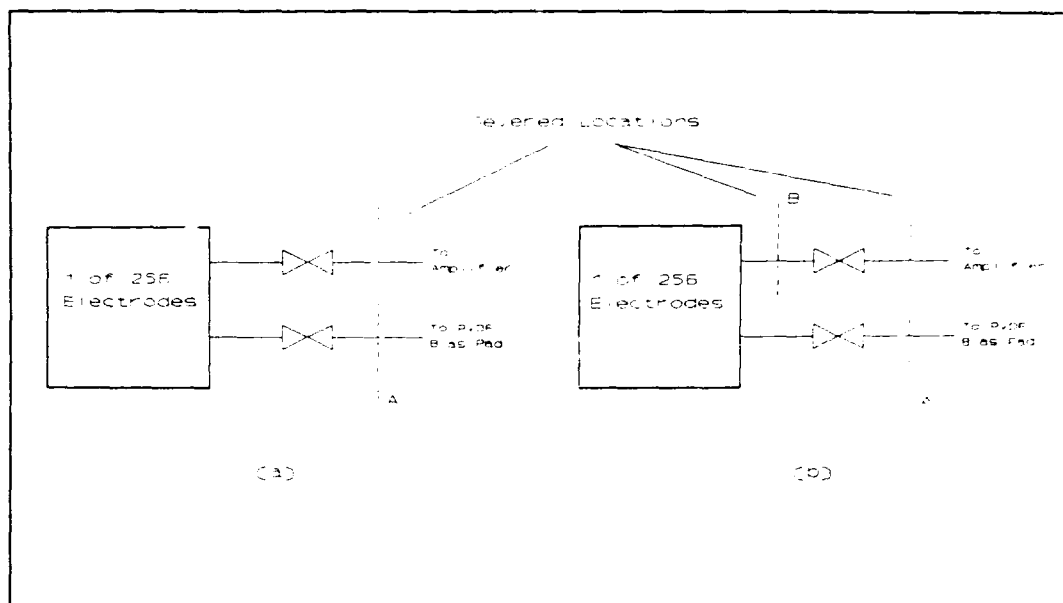
Figure V-7.   Sever locations used to isolate (a) both transmission gates, and (b) one transmission gate.

Using the Keithley electrometer, the electrode's DC input resistance was measured to be 6×10^8 Ω.   Isolating one transmission gate from the electrode (Figure V-7b), and measuring the resistance into the electrode resulted in a value of 6×10^8 Ω.   Isolating the opposite transmission gate (on a second electrode), and measuring the DC input resistance into the other electrode, it was observed that an identical measurement was made.

Finally, isolating both transmission gates from the electrode resulted in measuring an infinite input impedance, as expected.   This test confirmed that the charge was not leaking through the substrate to ground.

Since both the input and output impedances are high, some finite transfer of charge would be expected. An additional circuit parameter which affects the coupling of charge is capacitance. The capacitance of the PVDF film sample was calculated to be on the order of 10^{-12} Farads (Chapter IV, Section II), while the input capacitance of a MOSFET transmission gate is on the order of 10^{-15} Farads [18:125].

The output impedance of the PVDF film is given by the relationship $Z=(2\pi fC)^{-1}$, where f is the frequency, and C is the capacitance of the PVDF film [17:57]. Since the frequency is DC (f=0 Hz), a near infinite PVDF output impedance exists (actually 10^{12} to 10^{14} Ω).

While the DC resistances alone do not explain the circuit's failure, examining the difference between the input resistance and capacitance product (RC time constant) versus the output RC time constant, produces a large dissimilarity. With the PVDF film possessing a resistance of 10^{14} Ω (near infinite), and a capacitance of 10^{-12} F, the RC time constant is approximately 10^2 seconds. Correspondingly, the MOSFET possesses an input resistance of 10^9 Ω, and a capacitance of 10^{-15} F. Their product results in an RC time constant on the order of 10^{-6} seconds.

Consequently, the large difference in the time constants indicates that the electrode array circuitry discharges (through the transmission gates to ground) the

charge stored on the PVDF film 10^8 times faster than the film can accumulate new charge. This is a problem inherent within the circuit and it cannot be corrected.

Converse to this design, the 5x5 electrode array consisted of each electrode serving as the floating gate input to a MOSFET transistor (with near infinite input resistance). With an associated gate capacitance of 10^{-12} [18:135], the resulting RC time constant corresponds to that of the PVDF film. Therefore, the charge dissipation problem is not a concern for the 5x5 electrode array.

Multiplexed 5x5 Electrode Array Circuit

Following the construction of the TTL control circuitry for the 5x5 electrode array, the circuit was functionally tested as discussed in Chapter IV. The combinational logic circuit provided a synchronization signal for the digital storage oscilloscope's trigger input, as shown in Figure V-8. The synchronizing pulse identifies electrode (1,1), and provides a steady reference location on the oscilloscope's display. Figure V-9 shows the oscilloscope's display for the multiplexed circuit output. One electrode (1,1) maintains a 10 V input signal, while the other electrodes have no measureable potential applied. A noise spike occurs at approximately 0.65 ms due to the
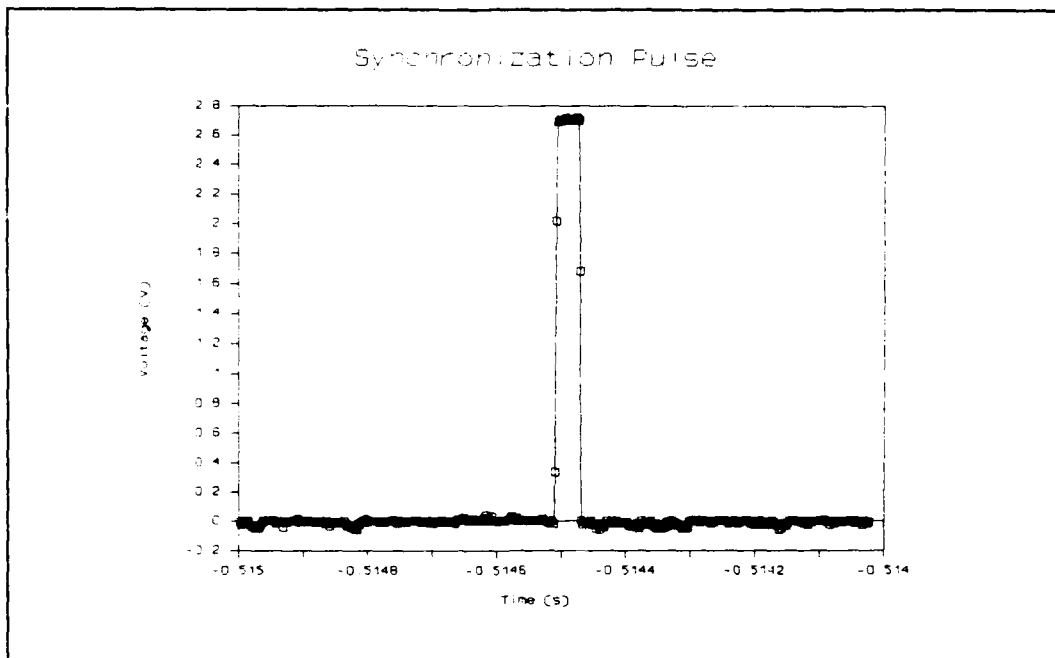
Figure V-8. Synchronization signal for the 5x5 electrode array circuit.
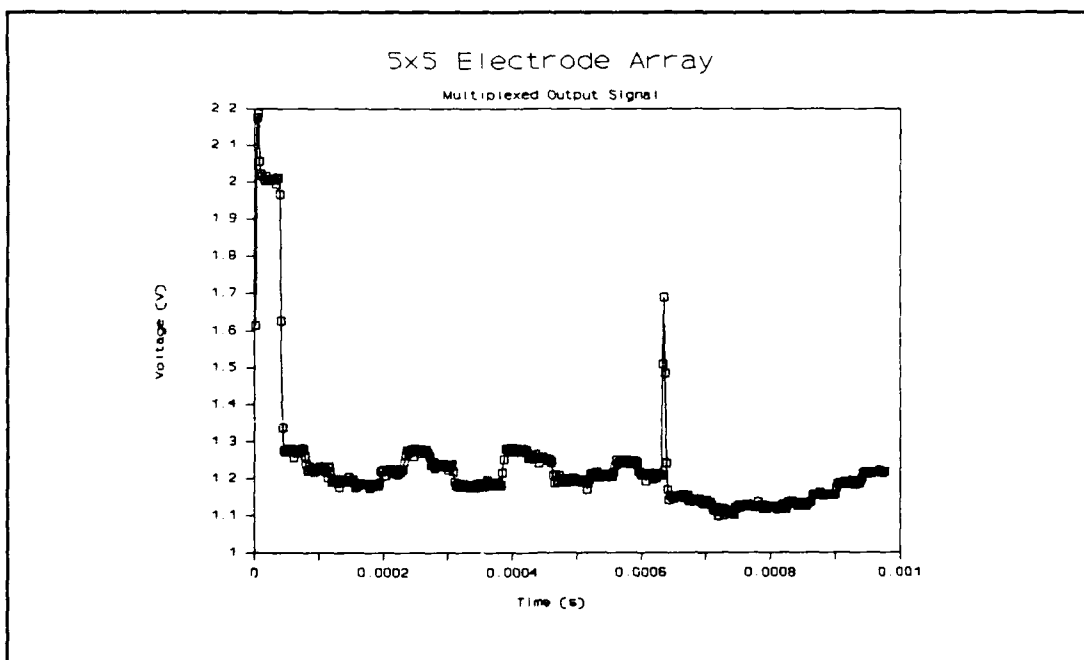

Figure V-9. Multiplexed 5x5 electrode array output with a 10 V signal applied to the first electrode in the first row.

discontinuity when using two discrete analog multiplexers
and combining the outputs onto one display.

Multiplexed 5x5 Electrode Tactile Sensor

Following confirmation that the control circuitry
functioned properly, the tactile sensor was then fabricated
by implementing the procedures outlined in Chapter IV.
Prior to characterizing the complete sensor, two issues were
resolved. The first issue concerned the adherence of the
PVDF film patch to the electrode array. The second issue
involved characterizing the response of a single electrode
to an applied load.

PVDF Film Adhesion. Four types of adhesives were
evaluated. Three were conformal coatings commonly used to
electrically passivate printed circuit boards, while the
fourth adhesive was a non-conducting, two-part adhesive.
The printed circuit board coatings were acrylic-, urethane-,
and silicon-based liquids (manufactured by Miller-Stephenson
Chemical Company, Danbury, CT 06810). The epoxy was a low
viscosity, non-polar adhesive (Epoxy Technology
Incorporated, Billerica, MA 01821).

Applying the adhesives to the IC was accomplished at
room temperature using a similar technique, yet each
adhesive possessed its own handling characteristics. The
silicon and urethane coatings were the easiest to apply. A

single drop from a 3 cc syringe provided an ample supply of adhesive. The acrylic was slightly less viscous, and it tended to cure at a faster rate, sometimes making it more difficult to work with. The fast cure rate of the acrylic material was observed by the noticeable clouding and thickening of the adhesive. Because of its viscosity, the epoxy was the most difficult material to work with.

All four adhesives were applied at room temperature, followed with an oven bake at 65°C, as recommended by the adhesive's manufacturer. All four adhesives provided a solid bond between the PVDF film and the aluminum electrodes, as discussed below. Complete cure times occurred after 1 hour at 65°C for the acrylic, urethane, and epoxy. The silicon coating required a cure time of at least 4 hours (at 65°C) before a solid bond developed.

The most durable bond was obtained from the two-part epoxy. It provided the highest degree of resistance to peeling when probed under an optical microscope with a pair of sharp bonding tweezers. Next to the epoxy, ranked high to low, were the urethane, acrylic, and silicon materials. In all cases, the degree of electrical coupling between the PVDF film and the electrode array appeared to be sufficient, as determined by the ability to couple a 0 - 10 V signal from the film to an electrode, as discussed in Chapter IV.

Individual Electrode Response. Applying a range of loads to the 25 μm thick PVDF film yielded a linear response

for a range of loads spanning 5 g to 75 g. Figure V-10 displays the amplifer's output response for loads spanning 5 g to 100 g. The amplifier's output response reached it's maximum output of 7 V with an applied load of approximately 75 g. Larger loads caused no significant change (increase) in the sensor's output.

Individual Electrode Response

Voltage (V)

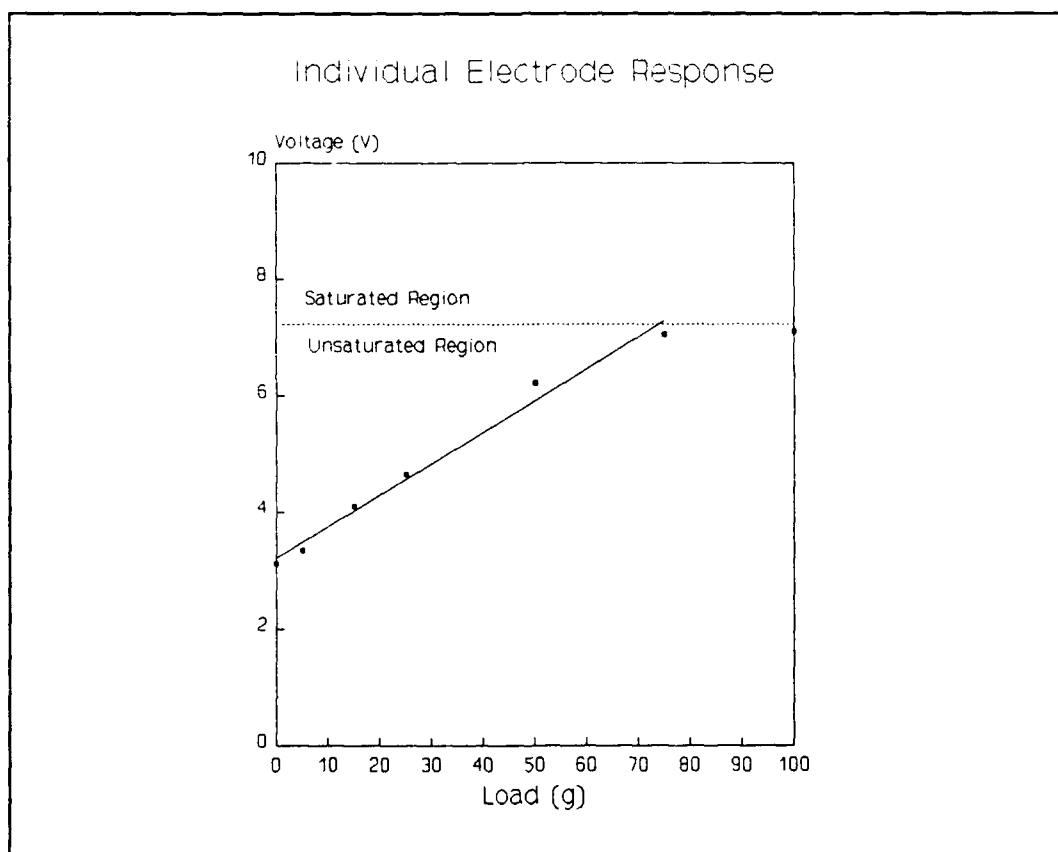Saturated Region

Unsaturated Region

Load (g)

Figure V-10. Individual electrode response to applied loads spanning 5 g to 100 g, with the PVDF film biased at 2.2 V. (Each data point represents the average response of four electrodes from one sensor.)

Data Acquisition and Reduction

Film Biasing. The most difficult task involved in
determining the shape of an incident load, began with
providing a uniform bias across the entire electrode array,
prior to load application. Simply applying an external
static voltage bias to the metalized PVDF film's surface
induced a nonuniform charge level on each of the amplifier's
gate electrode. Figure V-11 displays the multiplexed output
response of all 25 electrodes from the 5x5 array sensor,
with a non-uniform charge distribution caused by the
application of a 2 V static bias.
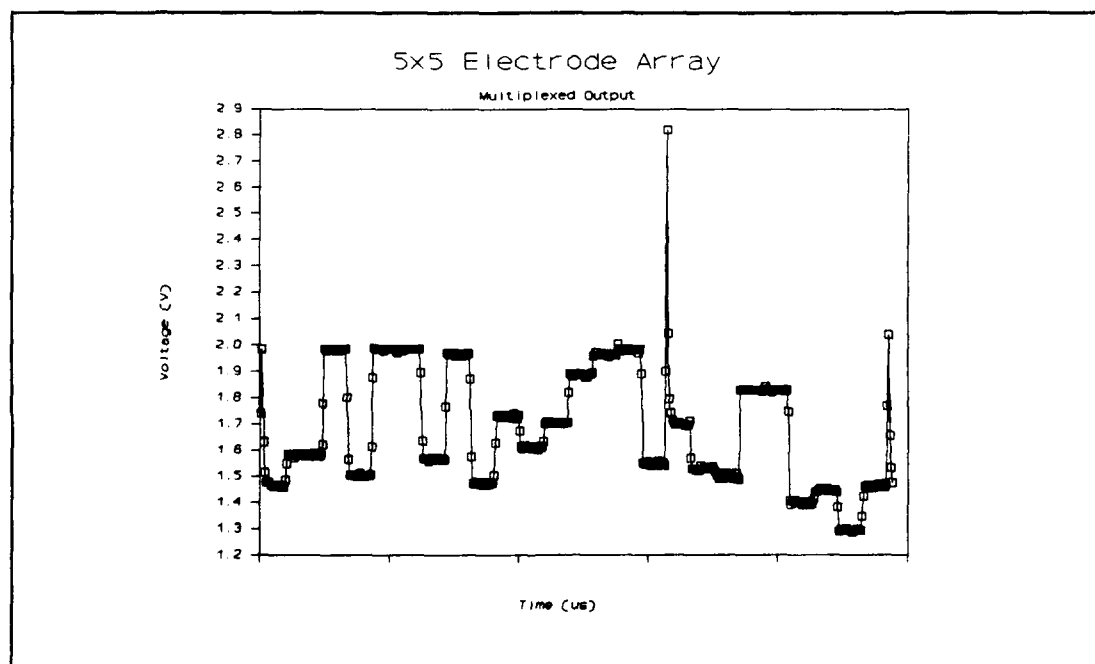
Figure V-11. Multiplexed output response of the 5x5 array
(25 electrodes) with a 2 V bias applied to the PVDF film's
metalized surface prior to charge equilibration.

Figure V-12 shows the same multiplexed output response as a function of voltage versus position. This visualization of the electrode array divides the continuous voltage versus time representation (Figure V-11), into discrete elements. The electrodes labeled on the horizontal axis of the Figure V-12 correspond to the electrodes displayed in Figure V-13.

Figure V-12. Equivalent multiplexed output response of the 5x5 array (25 electrodes) relative to that displayed in Figure V-10, as a function of voltage versus position.

Equilibration of the charge state on each electrode was necessary prior to taking measurements. This state was accomplished by probing each amplifier input with an appropriate biasing potential, as discussed below. The high

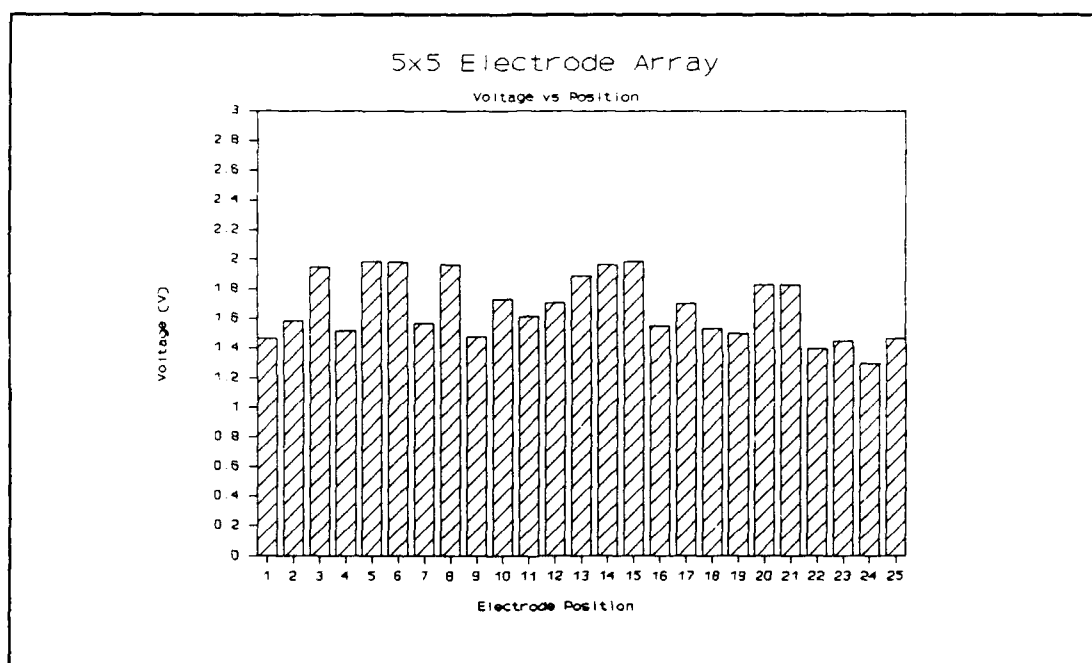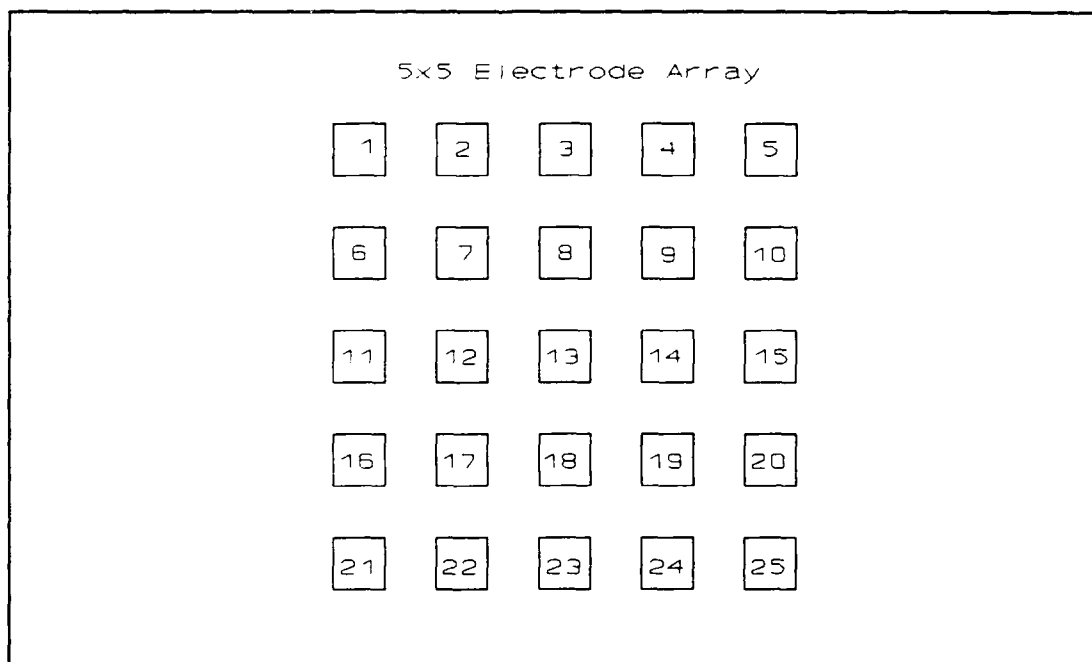Figure V-13. Electrode numbering scheme for the 5x5 electrode array.

impedance of both the PVDF film and the MOSFET amplifier's gate electrode functioned to store the applied charge. In the case of a positively polarized film, the external bias voltage was on the order of +4 V. A negatively polarized film required a +9 V potential (an applied load would produce a corresponding subtractive voltage response). Figure V-14 shows a typical multiplexed output signal (25 electrodes) of a positively polarized film, once the charge equilibration procedure was concluded.

In either case, "precharging" the array produced a more uniform bias. Negative polarization, as defined in this context, refers to the PVDF film orientation where an applied load produced a decrease in the sensor amplifier's

output. Correspondingly, positively polarized films produce
an increase in the sensor amplifier's output.

   3 g Circular Load. Data acquisition was accomplished
using the procedure described in Chapter IV. Upon
completion of the initial scan of the biased sensor (control
scan), the load was gently lowered onto the array's surface.
When the load made contact with the surface, a noticeable
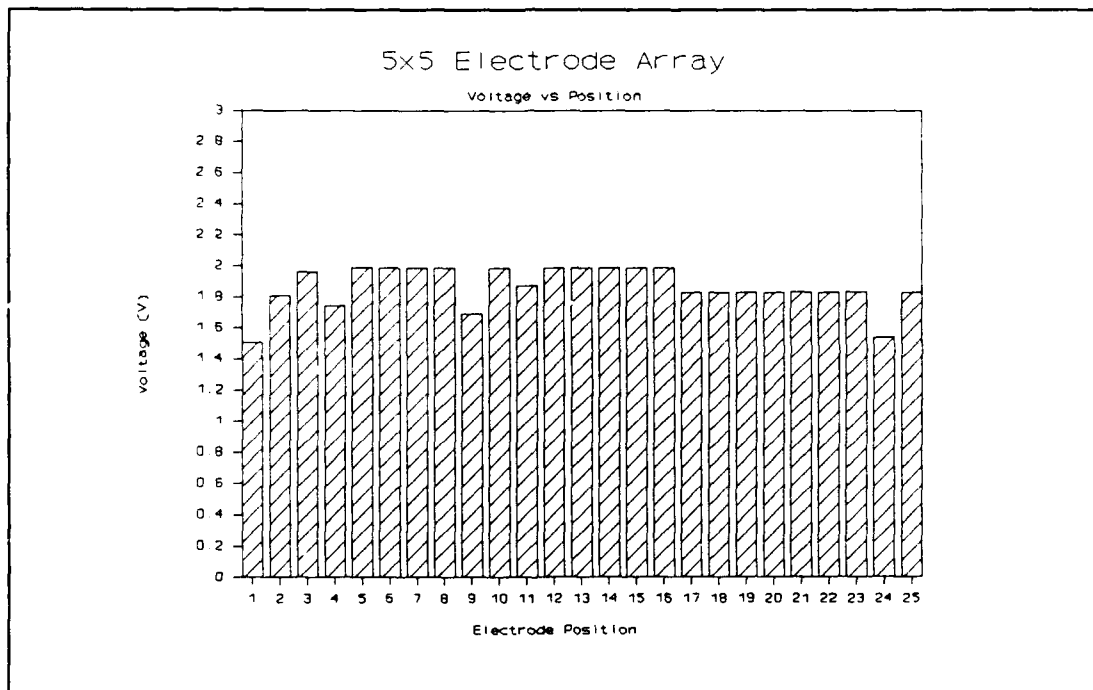
Figure V-14. Multiplexed output response of the 5x5 array
(25 electrodes) with a 2 V bias applied to the metalized
PVDF film's surface, after applying 4 V to the gate of each
MOSFET amplifier.

change occurred at the amplifier outputs (as observed on the
oscilloscope's display). Figure V-15 shows the effect of a
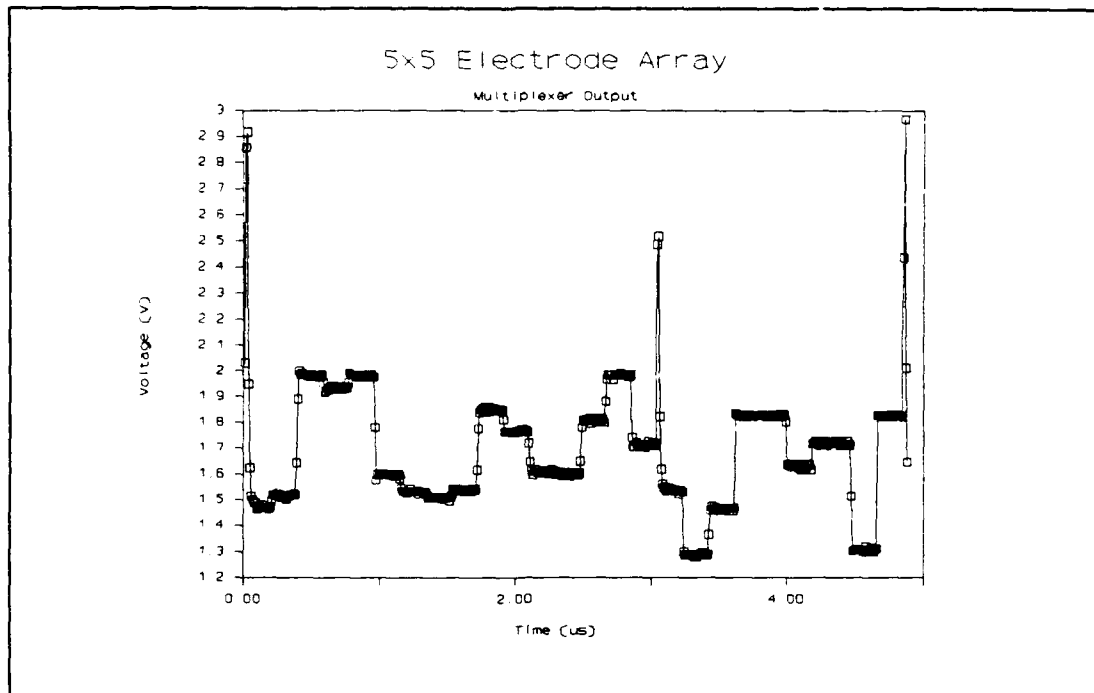
Figure V-15. Multiplexed electrode array output with a
4 mm diameter, 3 g circular applied load.

4 mm diameter, 3 g circular load, which was placed on the

array.

Following normalization of the individual electrode

voltage responses relative to the largest response in the

array's data file (composed of the responses of all 25

electrodes), a three-dimensional representation of the

circular test shape was obtained (Figure V-16).

While a circular shape is somewhat recognizable in

Figure V-16, selecting topographical slices provided a

clearer visualization of the shape. Figure V-17 exhibits an

ensemble of topographical slices spanning between the 0.4 V

and 0.55 V levels. Over each slice is positioned a scaled
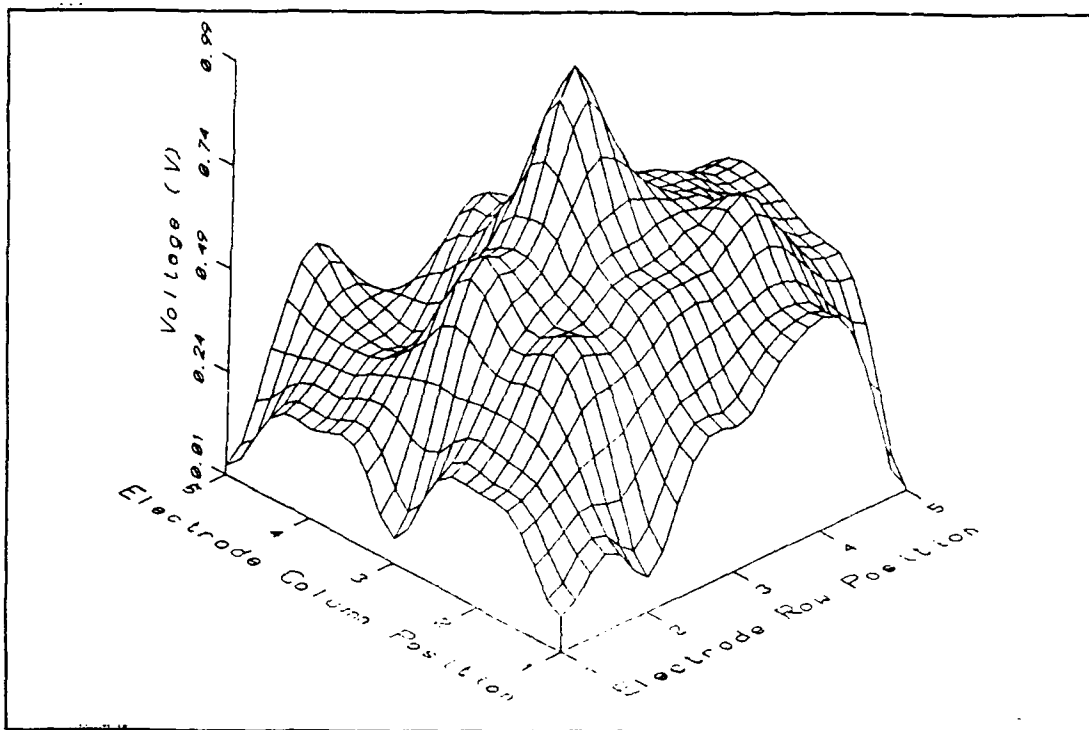
Figure V-16.   Three dimensional response of a 4 mm diameter,
3 g circular load applied to the 5x5 electrode array.

image which identifies the location and shape of the applied

load.   Using a grid of squares as a template, the area of

each topographical slice could be calculated.   Comparing

this area to the actual area of the applied load (using the

same template), yielded a metric (filter) which was used to

select the topographical slice that "best" reproduced the

shape of the applied load.   In this case, the 0.45 V

topographical slice yields the best correlation with the

surface area of the load.

Upon selection of the "best" topographical slice, an

overlay of the selected sensor electrodes in the array was

applied, as shown in Figure V-18.   Observing all three
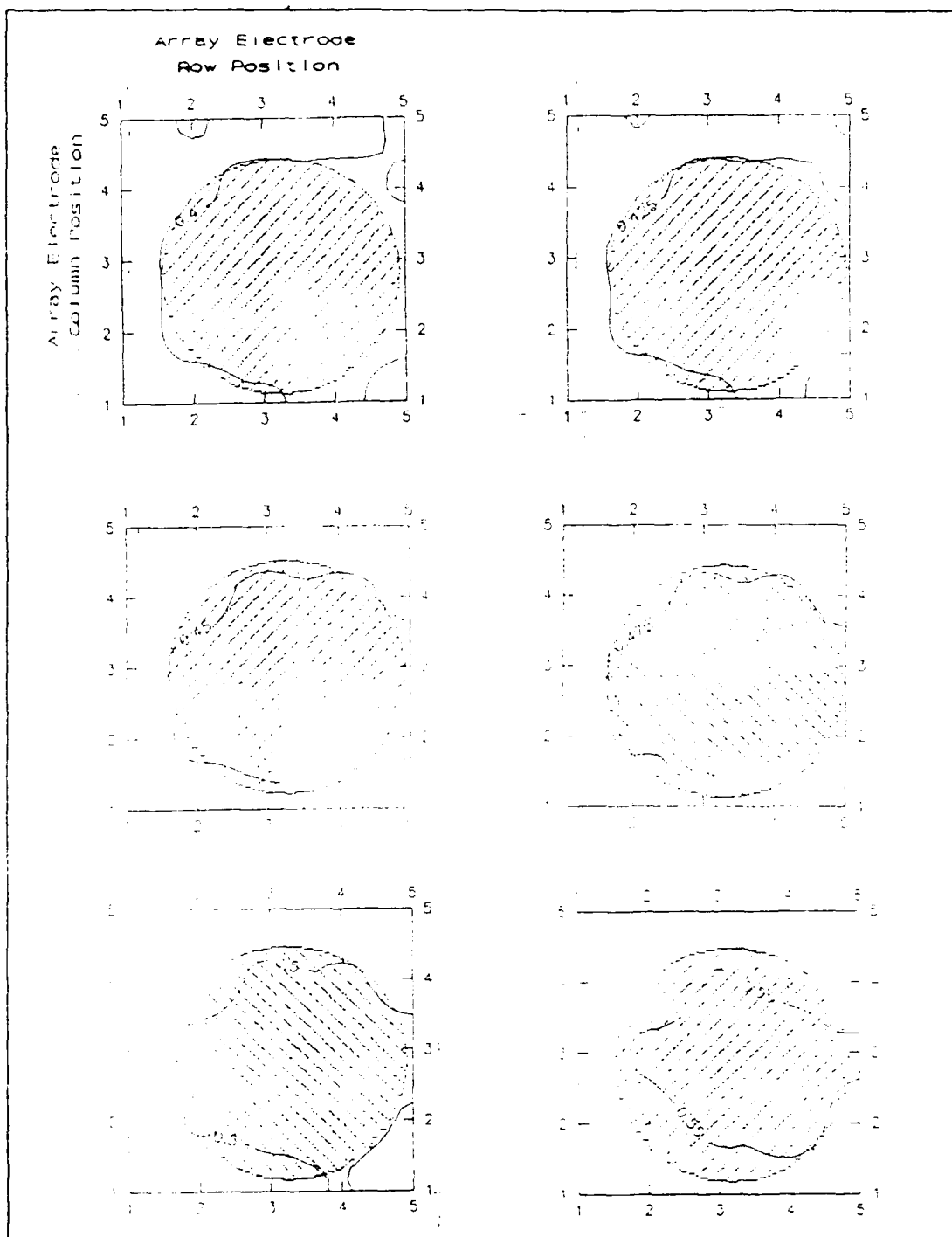
Figure V-17. Representative topographical slices of the 4 mm diameter, 3 g circular load. (The tick marks represent the bisections of each electrode element).
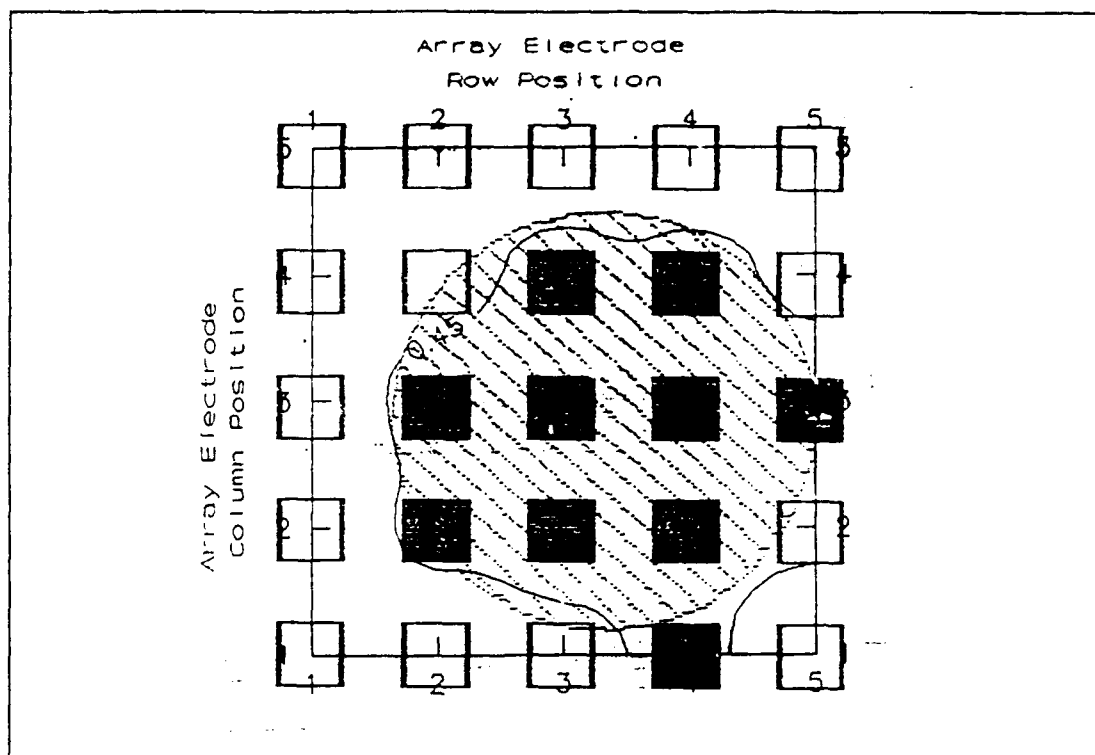
Figure V-18. Overlay of the selected array electrodes (black) and non-selected electrodes (white); the applied 4 mm diameter, 3g circular load; and the selected topographical slice whose area best correlates with that of the applied load.

images together in an overlayed configuration, produced a recognizable representation of the applied circular shape.

100 g Circular Load. Figure V-19 shows the corresponding overlayed representation (including the best-fit topographical slice) associated with the 4 mm diameter, 100 g circular load applied to the 5x5 array. Two electrodes, confined within the boundary of the applied shape, did not possess the threshold voltage of 0.625 V. This "misfiring" was likely caused by misalignment of the probe arm. That is, the rigidity of the probe arm, inherent
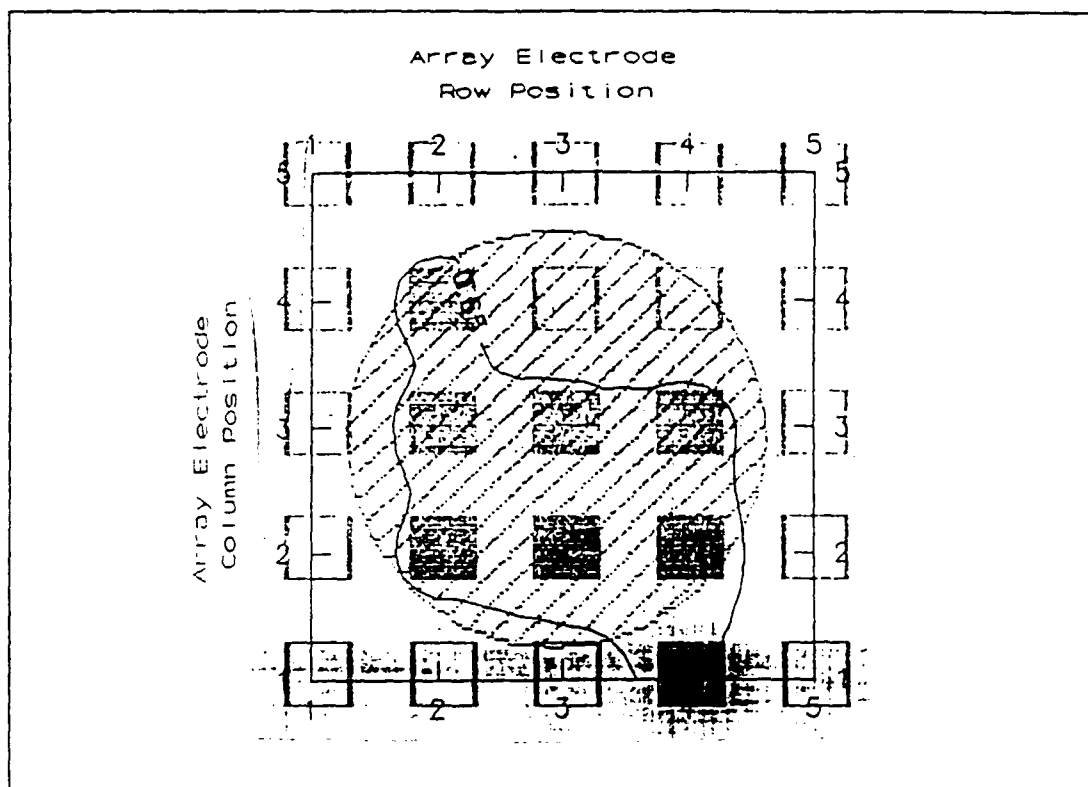
Figure V-19. Overlay of the selected array electrodes (black) and non-selected electrodes (white); the applied 4 mm diameter, 100 g circular load; and the selected topographical slice whose area best correlates with that of the applied load.

of the probe arm design, resulted in a non-uniform load distribution of the circular shape over the electrode's array.

Other Considerations. A variety of other shapes were applied to the array, including a rectangle, toroid, and hexagon. The rectangle was sampled in two orientations: its longest edge oriented parallel to a boundary edge of the array, and its longest edge oriented parallel to an internal diagonal of the array. In addition, the hexagon was

designed for use with the larger 16x16 array. When centered over the 5x5 array, the entire array was concealed. For this reason, the hexagon was positioned off to one side, resulting in only a portion of the shape to cover the array.

The circle, toroid, rectangle (both orientations), and hexagon were tested using 3 g, 45 g, and 100 g loads. The test results are displayed in Table V-2. Appendix F displays the full set of data collected for this test series. The circular and rectangular shape (parallel edge orientation) produced a linear voltage response for the loading range considered.

Table V-2. Filtered topographical voltage slice results for the circular, rectangular, toroidal, and hexagonal shapes for 3 g, 45 g, and 100 g loads.

	Applied Load		
Shape	3 g	45 g	100 g
Circle	0.45 V	0.5 V	0.65 V
Rectangle	0.45 V	0.5 V	0.675 V
Rectangle*	0.55 V	0.525 V	0.675 V
Toroid	0.45-0.55 V (0.5) V**	0.5-0.6 V (0.55) V**	0.6-0.65 V (0.625) V**
Hexagon	0.425 V	0.475 V	0.625 V

* Rectangular shape applied parallel to an internal diagonal of the array.

** ( ) V represents the average potential of the topographical slice selected for a given load.

Defining the linear voltage response for the rectangular load which was applied parallel to the array's internal diagonal was more difficult. A skewed rectangular shape was evident for the 3 g and 45 g loads, by viewing the various topographical slices. However, selecting a representative topographical slice from each load, using the area matching technique, resulted in slices taken from nearly the same voltage potential of approximately 0.50 V. Additionally, for a load of 100 g, the topographical slice patterns associated with the two rectangular shape orientations were nearly indistinguishable. Figures F-19 and F-22, displayed in Appendix F, shows an overlay using the 0.675 V topographical slice for both applied shapes. The inferior shape definition can be attributed to two influencing factors: a non-uniform weight distribution across the array's surface (similar to the 100 g circle), and exceeding the saturation threshold of the sensor (see Figure V-9).

The more complex shape of the toroid represented a more challenging shape recognition problem. Figures F-14 through F-16 (Appendix F), display the selected composite overlay arrangement for each toroidal load. The toroid used in this test was designed for the larger and denser electrode array (16x16). While an outline of a toroid could be discerned by viewing the topographical slices, choosing a single slice based on the area matching method was not practical. For

this reason, only a range of voltage values (based on visual inspection of the topographical slices) for each weight class was obtained.

Selecting a particular topographical slice for the toroid was accomplished by selecting the average of the voltage range (defined above), as shown in Table V-II. While the perfect topographical slice was not readily apparent, an upward linear trend is evident. That is, for an increasing load, the "averaged" value of the selected topographical slice increased as well, following the linear trend depicted in Figure V-9.

For the shapes and load range evaluated, an overall linear response trend is apparent. As depicted in Table IV-2, it is readily apparent that an average response level is characteristic of a given load range, and is independent of shape. For instance, the sensor's output response for a 3 g shape spans response values between 0.425 V and 0.55 V, while the 45 g shapes span 0.475 V and 0.6 V. While the differences between the two ranges are not ideally conclusive, the upward trend partially validates the "filter" algorithm.

Summary

This Chapter discussed the problems, solutions, and results associated with characterizing the performance of

the piezoelectric tactile sensor. While the originally designed 16x16 electrode array sensor failed to produce a fully functional tactile sensor, the 5x5 tactile sensor design from a previous thesis provided a critical link for the continuation of this project. The final result is a fundamental algorithm which may provide a pattern recognition technique useful in future tactile sensor research. The following chapter provides a summary of accomplishments, and provides recommendations for further work.

VI. CONCLUSIONS AND RECOMMENDATIONS

·The goal of this research effort was to design and fabricate a multiplexed piezoelectric tactile sensor onto a host silicon wafer. The sensor was designed to possess a 16x16 electrode array which was confined to a 6.5 mm x 6.5 mm surface area. In addition, the sensor was designed to possess the ability to establish an equilibrated charge state on the PVDF film prior to a load's application.

An integrated circuit was designed and fabricated which provided a solution to these goals. The design consisted of a resident analog multiplexer, which provided a time-division multiplexed representation of the electrode's array response. Selection or non-selection of the individual electrodes was controlled by two CMOS transmission gates. One transmission gate passed a voltage generated by the PVDF film to the output. The second transmission gate supplied a voltage potential to the electrode, which was necessary for establishing a constant bias state on the PVDF film.

This thesis effort was not successful with respect to the design of the multiplexed 16x16 electrode array IC; however, valuable information was obtained. The design for this project relied entirely on the proper operation of the transmission gates connected to each electrode. While the electrode array functioned properly (logically), failure occurred when the PVDF sensor was fabricated. A mismatch

between the RC time constants of the PVDF film and the input of each electrode compromised the sensor's operation. That is, the charge generated by the PVDF film was discharged through the electrode at a rate faster than the rate at which the PVDF film could generate it.

With the knowledge that this design would not suffice, work continued to verify that the concept of a multiplexed tactile sensor was still feasible. To accomplish this task, a previous AFIT tactile sensor design [2] was used, which employed a 5x5 electrode array. This design configuration consisted of each array element coupled directly into the gate electrode of a MOSFET transistor, resulting in a RC time constant similar to that of the PVDF film. A commercial analog multiplexer provided the time-division multiplexing function required to convert the 25 discrete electrode responses into an output signal as a function of time. This multiplexed output was then evaluated with respect to its capacity to provide information from which a fundamental pattern recognition algorithm could be aeveloped.

Two problem areas cited from the previous thesis were partially solved [2:5-2]. The first problem concerned film adhesion. Four adhesives were characterized as being physically compatible with the PVDF film, and could readily perform as a quality dielectric. The second problem involved the establishment of a uniform charge state over

the entire electrode array. This situation was accomplished by scanning each amplifier's input with a Micromanipulator probe biased at the desired voltage level.

Future Integrated Circuit. Further work in this research area needs to be accomplished. While the design incorporated in this project did not perform as expected, the piezoelectric PVDF tactile sensor still has a potential application in robotics [2:5-1].

The goals for the next fabrication attempt remain the same: increase the size of the electrode array (from 5x5), and establish an equilibrated bias on the PVDF film. A 9x9 array confined to a 7 mm x 7 mm square area would supply adequate resolution relative to that of the previous design. The establishment of a constant bias across the electrode array opens a new problem area.

Because of the RC time constant problem associated with the design used in this project, CMOS transmission gates cannot be used as a means for controlling the electrode array. In fact, each array electrode on a future design should serve as the gate input of a CMOS transistor, which is compatible with the PVDF film's generated voltage.

Two methods can be used to solve the charge coupling problem. The first solution entails the design of a transmission gate which contains an input capacitance approaching 10^{-12} F (the capacitance of a PVDF film square). This, however, is not feasible using CMOS technology. The

second solution involves the total isolation of the applied
bias from the electrode using a mechanical (optical) switch.
Figure VI-1 displays this concept for a 3x3 array. Each
electrode feeds directly into the gate of a linear
amplifier, followed by an analog multiplexer. The PVDF film
equilibration voltage is controlled by the bank of
mechanical/optical switches. This multiplexing scheme would
provide an input RC time constant compatible with the PVDF
film, and provide the ability to establish a charge state
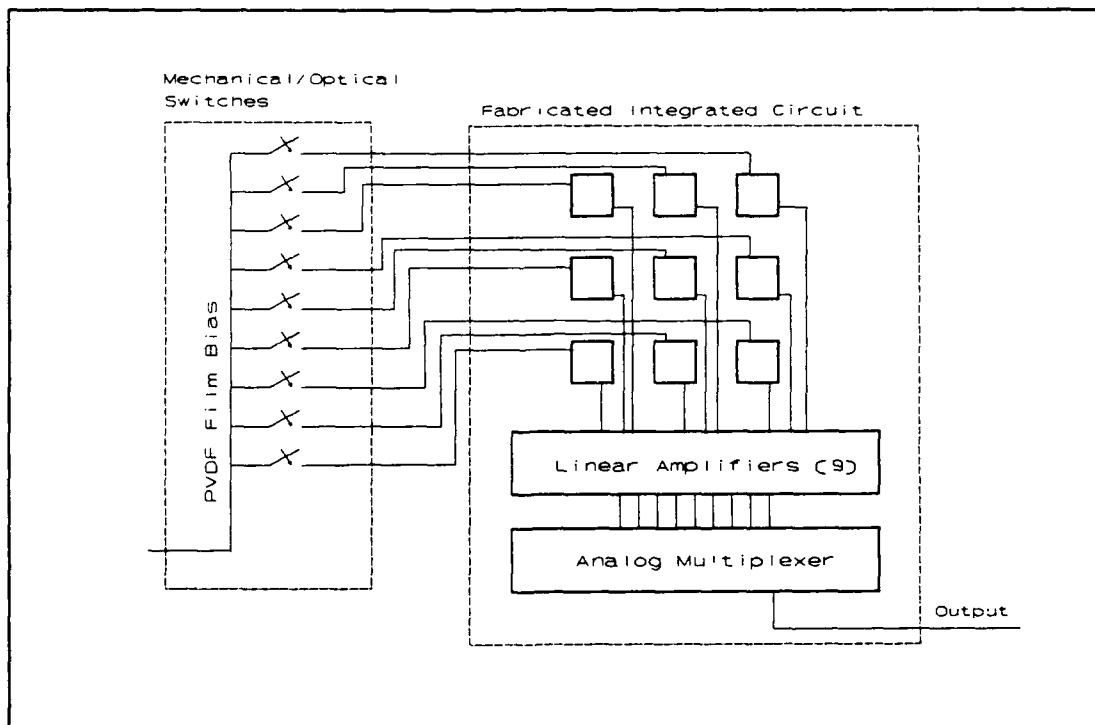across the PVDF film.

Figure   VI-1.   Multiplexed   tactile   sensor   employing
mechanical/optical switches to supply the PVDF bias voltage.

One problem associated with the mechanical switch approach involves the lack of available output connections. Using an IC package of the same dimensions used in this project limits the number of output pins to 64. A mechanical (optical) switch would have to reside external to the IC, thereby requiring a connection for each switch and electrode pair (81 connections for a 9x9 array). This exceeds the total number of available pins. Using a 132-pin package may overcome this 64-pin limitation, depending on other circuit requirements.

Design Considerations. Future work should focus primarily on the design and fabrication of a functioning resident analog multiplexing circuit. Future sensors must employ a reliable multiplexer. The design should incorporate abundant test pads, strategically placed throughout the designed multiplexer (especially between the counter and decoder circuitry), to facilitate in troubleshooting. In addition, the designed multiplexer must incorporate sufficient latitude such that it can reliably function for any reasonable variation in the fabrication process.

Modification of the probe arm assembly is necessary to obtain a more evenly distributed load over the array's surface. A lack of rotational flexibility sometimes prevented a load (shape) from contacting the tactile sensor orthogonal to the PVDF film's surface. Modifying the probe

holder to use a pin, rather than a threaded screw, would provide the degree of freedom necessary to obtain an even weight distribution over the sensor's surface.

In conclusion, coupling each electrode directly into the gate of a MOSFET amplifier input would ensure adequate charge coupling between the PVDF film and the integrated circuit. Selected electrodes may employ the mechanical switch biasing method (limited by the number of available output connections). This would allow a modular design approach, as well as advance the tactile sensor design an additional level.

APPENDIX A: Materials and Equipment

Table A-1: INSTRUMENTATION

Digitizing Oscilloscope, Model HP 54100
Hewlett Packard Company
Colorado Springs, CO

Semiconductor Parameter Analyzer, Model HP 4145A
Hewlett Packard Company
Colorado Springs, CO

Fluke Multimeter, Model 77/AN
John Fluke Manufacturing Co
Everett, WA

Keithley 617 Electrometer
Keithley Instruments, Inc.
Cleveland, OH

Zenith 248 Data Collection Computer
(with IEEE-488 GPIB Interface)
Zenith Data Systems,
Glenview, IL

ISI Scanning Electron Microscope, Model WB-6
International Scientific Instruments, Inc.
Milpitas, CA

Micromanipulator Probe Station, Model 6200
The Micromanipulator Company, Inc.
Escondido, CA

Micromanipulator, Model 450/360 VM
Manipulators (3),
The Micromanipulator Company, Inc.
Escondido, CA

Power Supply, Model HP 6205B
Hewlett Packard Company
Colorado Springs, CO

Pulse Generator, Model 148
Wavetek, Inc.
San Diego, CA

Aluminum Wedge Bonder, Model TV909
MECH-EL Industries, Inc.
Woburn, MA

Loading Weight Probe
Weights/Shape Kit
Protoboard
Scalpel
Syringe
Solef PVDF film (25 μm, and 40 μm thick)
Kynar PVDF film (52 μm thick)
Shipley Photoposit 1400-17 Photoresist
Dow Corning 3140 Room Temperature Vulcanizing
        (RTV) Silicone Coating
Ferric Chloride
Silver Conductor Paint
MOSIS Circuits
Acrylic, Silicon, and Urethane Adhesives
De-Ionized Water
Concentrated (37%) HCl
Glass Slides
Isopropyl Alcohol

Appendix B: PVDF Film Specifications

Table B1. PVDF Film Electrical and Mechanical Parameters [?].

	Solef 25 μm	Solef 40 μm	Kynar 52 μm	Kynar 110 μm
d_{33}	16 pC/N	16 pC/N	20-22 pC/N	20-22 pC/N
ϵ_r	11	11	11-13	11-13
k_{33}	10-15%	10-15%	19%	19%
Tensile Strength	180 MPa	180 MPa	160-330 MPa	160-330 MPa

Table B2. PVDF Film Chemical Resistance [2].

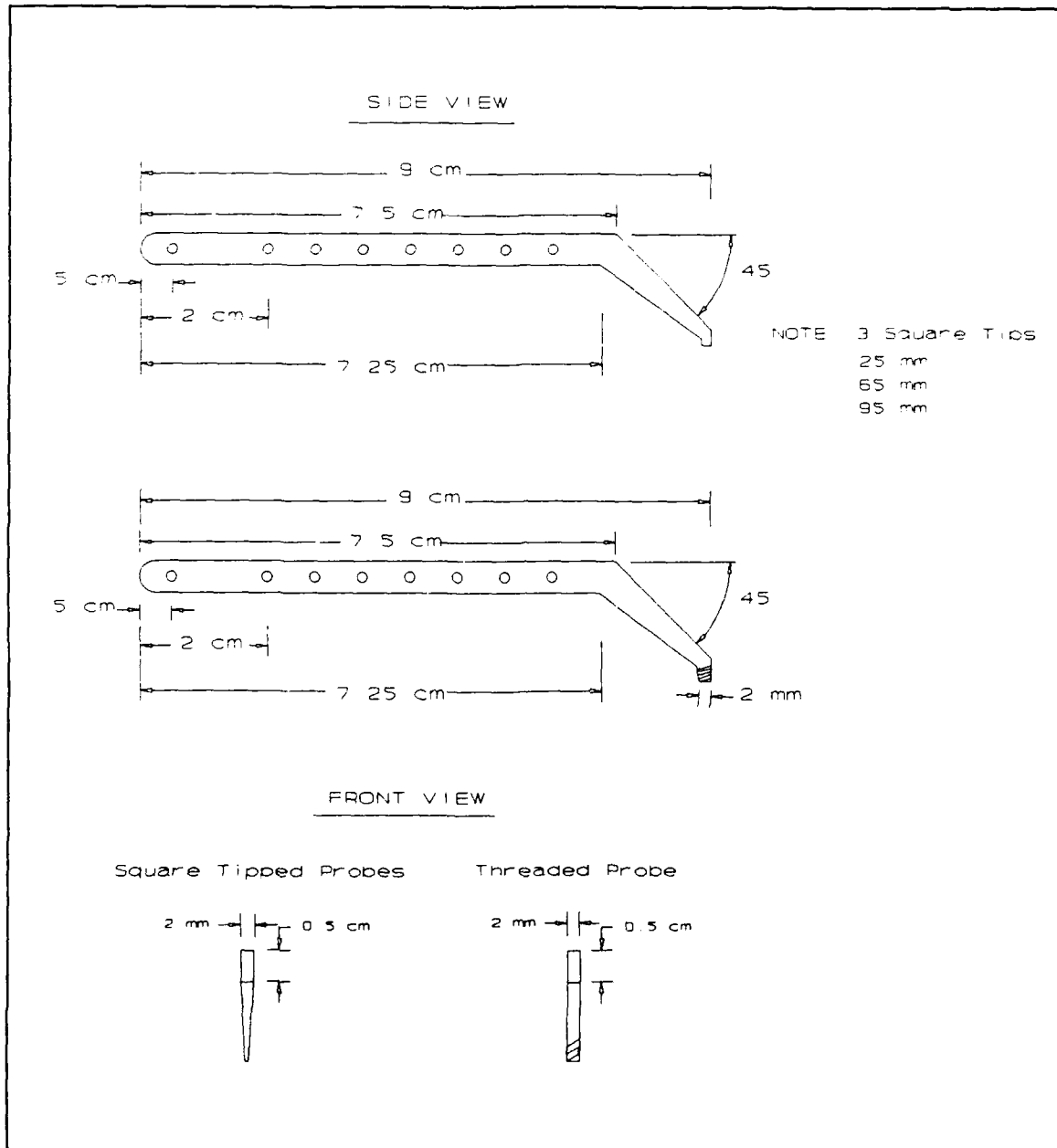| Chemical	Maximum Temperature for Exposure
Acetone	Not Recommended
Acetone (10% in Water)	125°F
Butyl Acetate	80°F
Ferric Chloride	275°F
Hydrochloric Acid (Concentrated)	275°F
Isopropyl Alcohol	140°F
Methyl Ethyl Ketone	Not Recommended
Silicone Oil	250°F
Xylene	200°F

Appendix C: Probe Assembly Design
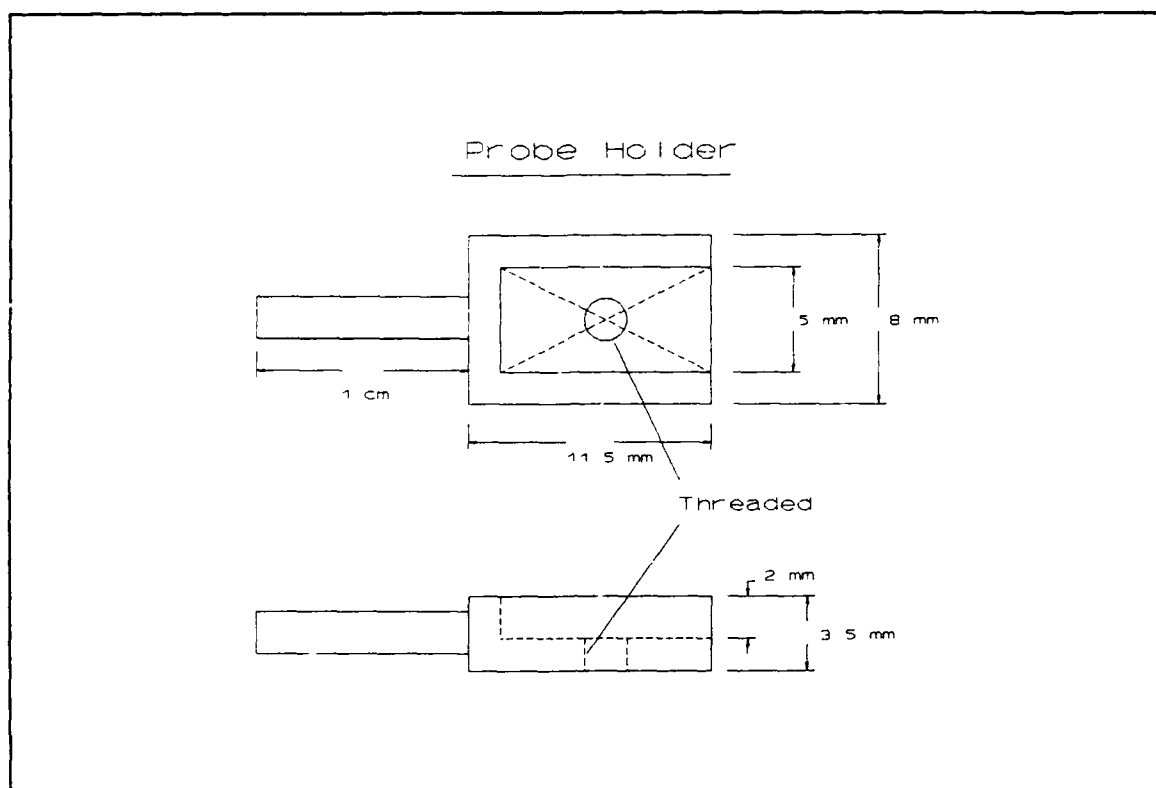

Figure C-1. Probe Arm Design

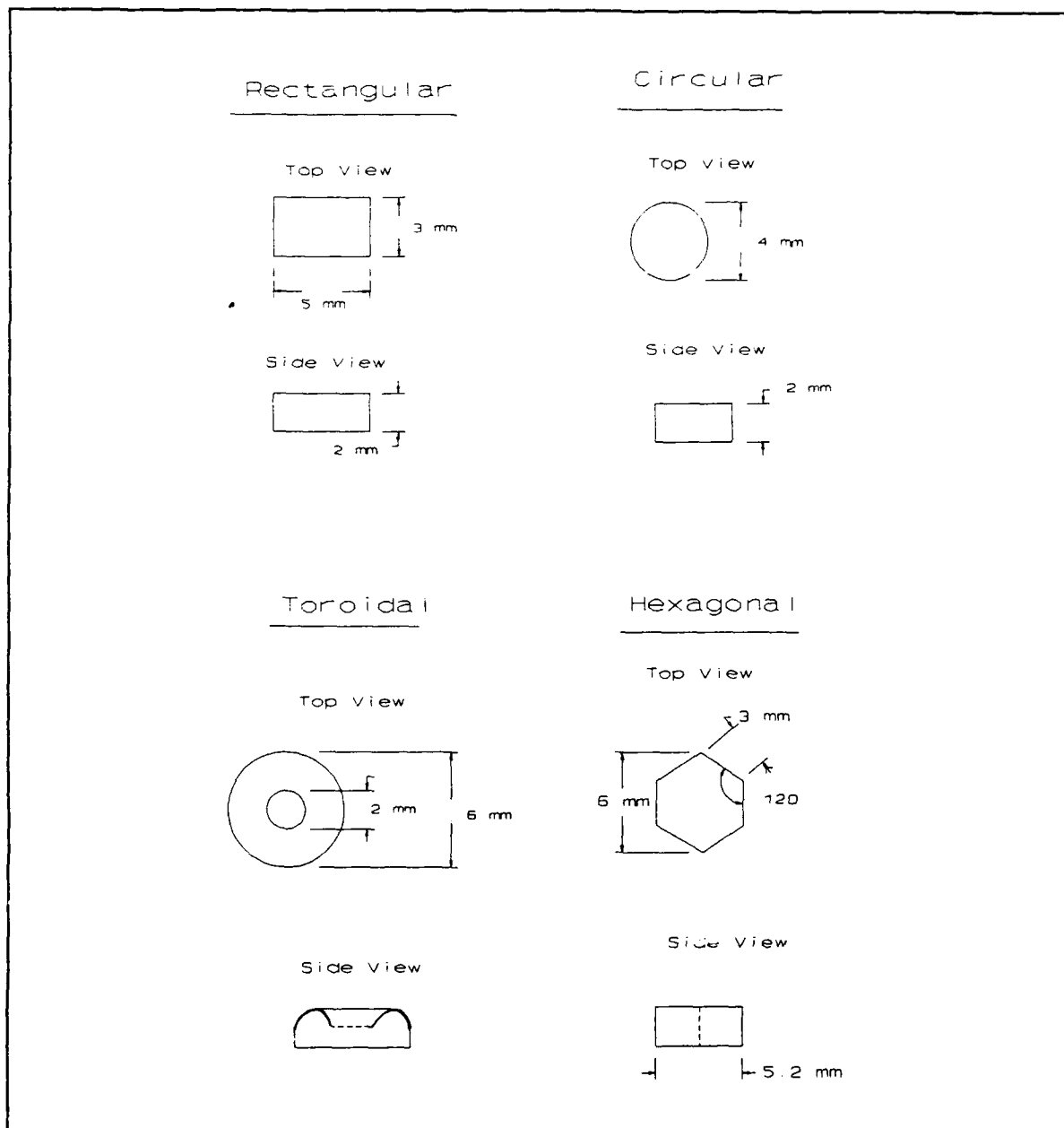Figure C-2. Probe holder for attaching probe arm to Micromanipulator Subassembly.

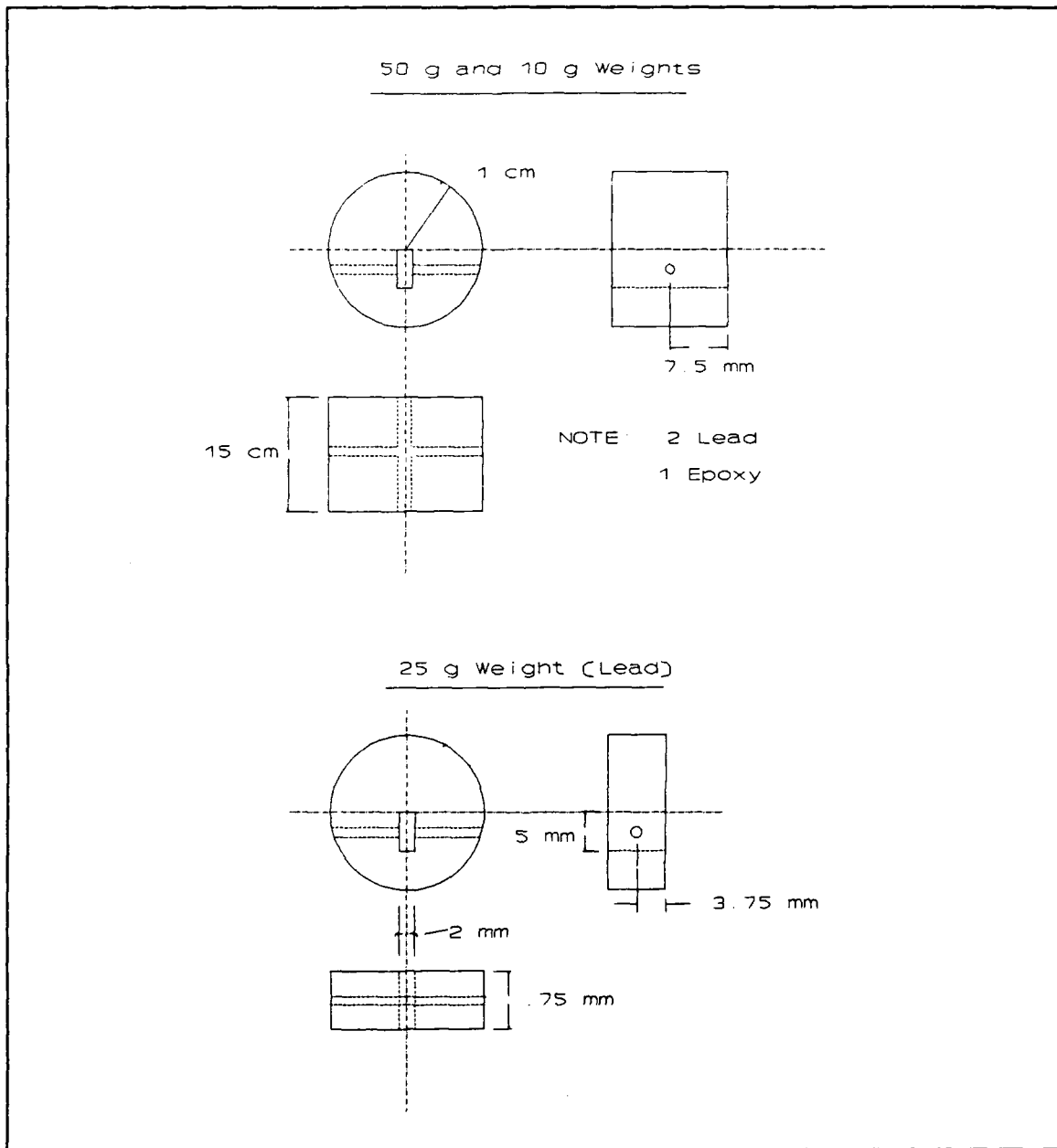**Figure C-3. Designed test shapes.**

Figure C-4.   Designed probe arm weights.

Appendix D: MOSIS Spice Parameters

*** MOSIS N-CHANNEL MOSFET MODEL FOR 1.5 MICRON CMOS ***

```
.MODEL CMOSN NMOS LEVEL=2 LD=0.250000U TOX=415.000000E-10
+ NSUB=6.880000E+15 VTO=0.751458 KP=5.342000E-05
+ GAMMA=0.5743 PHI=0.6 UO=642 UEXP=0.160551 UCRIT=23573.9
+ DELTA=4.21614 VMAX=58782.3 XJ=0.150000U
+ LAMBDA=3.880171E-02 NFS=1.000000E+11 NEFF=1
+ NSS=1.000000E+12 TPG=1.000000 RSH=36.110000
+ CGDO=3.120311E-10 CGSO=3.120311E-10 CGBO=4.447631E-10
+ CJ=1.320000E-04 MJ=0.779100 CJSW=4.830000E-10
+ MJSW=0.227200 PB=0.800000
```

*** MOSIS P-CHANNEL MOSFET MODEL FOR 1.5 MICRON CMOS ***

```
.MODEL CMOSP PMOS LEVEL=2 LD=0.250000U TOX=415.000000E-10
+ NSUB=6.760000E+15 VTO=-0.782902 KP=2.197000E-05
+ GAMMA=0.5693 PHI=0.6 UO=264 UEXP=0.257213 UCRIT=18948.1
+ DELTA=1.000000E-06 VMAX=58979.3 XJ=0.050000U
+ LAMBDA=5.480820E-02 NFS=1.000000E+11 NEFF=1.001
+ NSS=1.000000E+12 TPG=-1.000000 RSH=115.800000
+ CGDO=3.120311E-10 CGSO=3.120311E-10 CGBO=5.289931E-10
+ CJ=2.430000E-04 MJ=0.555300 CJSW=3.035000E-10
+ MJSW=0.341500 PB=0.800000
```

APPENDIX E: BASIC COMPUTER PROGRAM CODE

PARAMR1.BAS: This BASIC computer program code retrieves the visual display
from the Semiconductor Analyzer to an ASCII text file.

```
5  REM  THIS PROGRAM WILL "CAPTURE" THE SCREEN ON THE HP4145
10  REM  INITIALIZE THE 488 VARIABLES
15 DEF SEG=&HC400
20 INIT%=0
30 TRANSMIT%=3
40 RECIEVE%=6
50 SEND%=9
60 SPOLL%=12
70 ENTER%=21
80 HP4145%=2: MYADDR%=21
90 SYSCON%=0
99  REM initialize the card
100 CALL INIT%(MYADDR%,SYSCON%)
105 REM GET THE DRAIN VOLTAGE DATA
110 PRINT " "
115 INPUT "ENTER THE INITIAL VIN VOLTAGE: ",VD1
120 INPUT "ENTER THE VIN VOLTAGE STEP SIZE: ",VDS
125 INPUT "ENTER THE NUMBER OF STEPS: ",VDNS
130 PRINT " "
135 REM GET THE GATE VOLTAGE DATA
140 INPUT "ENTER THE INITIAL BIAS VOLTAGE: ",VG1
145 INPUT "ENTER THE BIAS VOLTAGE STEP SIZE: ",VGS
150 INPUT "ENTER THE NUMBER OF STEPS: ",VGNS
155 PRINT " "
160 REM GET THE VOUT DATA
165 REM DETERMINE THE NUMBER OF CURRENT POINTS TO FETCH
170 POINTS=VDNS*VGNS
172 OPTION BASE 1
173 REM DIMENSION THE ARRAY TO HOLD THE DATA
175 DIM A(POINTS)
180 PRINT "RETRIEVING THE VOUT VOLTAGE VALUES FROM HP4145"
185 PRINT " "
190 GOSUB 500
260  REM COMBINE THE THREE SETS OF DATA INTO THE FINAL OUTPUT
265  INPUT "ENTER THE NAME OF FILE TO STORE DATA: ", N$
270  OPEN "O", #1, N$
275  VD=VD1
276  VG=VG1
280  DIM OUTDATA(VDNS,VGNS)
282  FOR K=1 TO VGNS
285          FOR J=1 TO VDNS
287                  OUTDATA(J,K)=A(J +(K-1)*VDNS)
290          NEXT J
292  NEXT K
293  REM WRITE THE OUTPUT FILE
294  PRINT#1,VD1,
295  FOR K=1 TO VGNS
296    IF K>1 THEN VG=VG+VGS
```

```
297      PRINT#1,CHR$(9);VG,
298      NEXT K
299      PRINT#1,""
300  FOR J=1 TO VDNS
301          IF J>1 THEN VD=VD+VDS
302              PRINT#1,VD,
303          FOR K=1 TO VGNS
310                          PRINT#1,CHR$(9);OUTDATA(J,K),
320          NEXT K
321      PRINT#1,""
325  NEXT J
330 CLOSE #1
335 PRINT "ALL DONE" :SYSTEM
340 STOP
500 REM SUBROUTINE TO TRANSFER DATA FROM HP4145 TO PC
501 CALL SPOLL%(HP4145%,POLL%,STATUS%)
506 S$="UNL UNT"
507 CALL TRANSMIT(S$,STATUS%)
508 S$="BC"
509 CALL SEND%(HP4145%,S$,STATUS%)
510 S$="DO 'VOUT'"
520 CALL SEND%(HP4145%,S$,STATUS%)
530 S$="MLA TALK 2"
540 CALL TRANSMIT%(S$,STATUS%)
545 TEMP$=SPACE$(13)
550 FOR I=1 TO POINTS
560 CALL RECIEVE%(TEMP$,LENGTH%,STATUS%)
571 A(I)=VAL(RIGHT$(TEMP$,12))
580 NEXT I
585 S$="UNL UNT"
586 CALL TRANSMIT%(S$,STATUS%)
590 RETURN
600 END
^Z
```

HPOSC1A.BAS: This BASIC computer code retrieves the HP54100 digital oscilloscope's display (Memory 1) into a user specified ASCII text file.

```
10 DIM R$(100)
20 DIM HPDAT(1024)
30 DEF SEG=&HC400                ' ADDRESS OF GP-IB INTERFACE
40 INIT%=0                       ' OFFSET OF INITIALIZE ROUTINE
50 TRANSMIT%=3                    ' OFFSET OF TRANSMIT ROUTINE
60 RECEIVE%=6                     ' OFFSET OF RECIEVE ROUTINE
70 SEND%=9                        ' OFFSET OF SEND ROUTINE
80 SPOLL%=12                      ' OFFSET OF SERIAL POLL ROUTINE
90 ENTER%=21                      ' OFFSET OF ENTER ROUTINE
100 '
110 ' GP-IB ADDRESSES OF INSTRUMENTS
120 '
130 PRINTER%=1: MY.ADDR%=21: K617%=27: HPOS%=15
140 SYSCON%=0                    'PC488 ACTS AS CONTROLLER
150 '
160 CALL INIT%(MY.ADDR%,SYSCON%)
170 '
180 S$="REN SDC 15"
190 CALL TRANSMIT%(S$,STATUS%)
200 '
220 S$="HEADER OFF"
226 CALL SEND%(HPOS%,S$,STATUS%)
228 S$="stop"
230 CALL SEND%(HPOS%,S$,STATUS%)
232 S$="CLEAR"
233 CALL SEND%(HPOS%,S$,STATUS%)
234 S$="RUN"
235 CALL SEND%(HPOS%,S$,STATUS%)
240 S$="ACQUIRE TYPE AVERAGE COUNT 8 POINTS 500"
250 CALL SEND%(HPOS%,S$,STATUS%)
251 TEMP$=MID$(TIME$,8,1)
252 IF MID$(TIME$,8,1)=TEMP$ THEN 252
253 IF MID$(TIME$,8,1) <>TEMP$ THEN 253
260 S$="STORE CHANNEL1,MEMORY1"
261 CALL SEND%(HPOS%,S$,STATUS)
262 S$="STOP"
270 CALL SEND%(HPOS%,S$,STATUS%)
280   INPUT "FILENAME FOR CHANNEL 1";DF$
290   OPEN "O",#1,DF$
300   S$="WAVEFORM SOURCE MEMORY1 TYPE NORMAL FORMAT ASCII points
500"
310   CALL SEND%(HPOS%,S$,STATUS%)
320   R$=SPACE$(15)
330   S$="POINTS?"
340   CALL SEND%(HPOS%,S$,STATUS%)
350   CALL ENTER%(R$,LENGTH%,HPOS%,STATUS%)
360   PNTS=VAL(R$)
370   S$="YREF?"
380   CALL SEND%(HPOS%,S$,STATUS%)
390   CALL ENTER%(R$,LENGTH%,HPOS%,STATUS%)
400   YREF=VAL(R$)
410   S$="YINC?"
420   CALL SEND%(HPOS%,S$,STATUS%)
```

```
430   CALL ENTER%(R$,LENGTH%,HPOS%,STATUS%)
440   YINC=VAL(R$)
450   S$="YOR?"
460   CALL SEND%(HPOS%,S$,STATUS%)
470   CALL ENTER%(R$,LENGTH%,HPOS%,STATUS%)
480   YORG=VAL(R$)
490   S$="XINC?"
500   CALL SEND%(HPOS%,S$,STATUS%)
510   CALL ENTER%(R$,LENGTH%,HPOS%,STATUS%)
520   XINC=VAL(R$)
530   S$="XOR?"
540   CALL SEND%(HPOS%,S$,STATUS%)
550   CALL ENTER%(R$,LENGTH%,HPOS%,STATUS%)
560   XORG=VAL(R$)
570   S$="XREF?"
580   CALL SEND%(HPOS%,S$,STATUS%)
590   CALL ENTER%(R$,LENGTH%,HPOS%,STATUS%)
600   XREF=VAL(R$)
610   S$="DATA?"
620   CALL SEND%(HPOS%,S$,STATUS%)
630   S$="MLA TALK 15"
640   CALL TRANSMIT%(S$,STATUS%)
650   X$=SPACE$(15)
660   Y$=SPACE$(15)
670   FOR I=1 TO PNTS
680     CALL RECEIVE%(Y$,LENGTH%,STATUS%)
690     X=(I*XINC)+XORG
700     Y=((VAL(Y$)-YREF)*YINC)+YORG
710     WRITE #1,X,Y
720   NEXT I
730   CLOSE #1
740   S$="LISTEN 15 MTA"
750   CALL TRANSMIT%(S$,STATUS%)
760   S$="LOCAL"
770   CALL SEND%(HPOS%,S$,STATUS%)
780 REM SYSTEM
^Z
```

CONVERT.BAS: This BASIC computer program code converts a voltage versus time display ascii file (from the HP54100 digital oscilloscope) to a voltage versus position ascii file (for graphic display).

```
5 REM  "This program converts a VOLTAGE vs TIME ASCII
6 REM   data file into a VOLTAGE vs POSITION file."
10 DIM OUTFILE$(3,25)
20 INPUT "Input Filename:", INFILE$
30 INPUT "Output Filename:", OUTFILE$
40 OPEN "I", #1, INFILE$
50 OPEN "O", #2, OUTFILE$
60 I=1
70 J=1
80 K=20
90 SUM=0
100 SUM=SUM+20
110 REM    "JUMP TO CENTER OF BLOCK"
120 FOR ISUM=1 TO 9
130    INPUT #1, T$, D$
140 NEXT ISUM
150 TEMP=0
160 AVG=0
170 REM    "AVERAGE 6 DATA POINTS"
180 FOR ISUM1=1 TO 6
190    INPUT #1, T$, D$
200    TEMP=TEMP+VAL(D$)
220 NEXT ISUM1
230 AVG=TEMP/6
240 REM IF EOF(1) THEN END
260 WRITE #2, J, I, AVG
270 REM    "TO SEE OUTPUT ON SCREEN, USE LINE 280"
280 REM WRITE J, I, AVG
290 REM      "JUMP TO CENTER OF NEXT BLOCK"
300 FOR C=1 TO 5
310    INPUT #1, T$, D$
320 NEXT C
330 I=I+1
340 IF I <= 5, GOTO 100
350 I = 1
360 J = J + 1
370 IF J <= 5, GOTO 100
380 CLOSE #1
390 CLOSE #2
400 END
^Z
```

NORMAL.BAS: This BASIC computer code program computes the difference between "File A" and "File B", then normalizes the output file.

```
10 DIM OUTFILE$(3,24), DELETE.ME(3,24)
20 INPUT "Name of File A:", FILEA$
30 INPUT "Name of File B:", FILEB$
40 INPUT "Name of Output File:", OUTFILE$
50 OPEN "I", #1, FILEA$
60 OPEN "I", #2, FILEB$
7u OPEN "O", #3, "delete.me"
100 TEMP=0
110 FOR J=1 TO 25
120     INPUT #1, I, K, X
130     INPUT #2, M, N, Y
140     Z=X-Y
150     WRITE #3, I, K, Z
160     IF Z > TEMP THEN TEMP=Z
170 NEXT J
180 CLOSE
190 OPEN "O", #1, OUTFILE$
200 OPEN "I", #3, "delete.me"
210 FOR K=1 TO 25
220     INPUT #3, M, N, Z
230     IF TEMP=0 THEN Z=0 ELSE Z=Z/TEMP
240 WRITE #1, M, N, Z
260 NEXT K
270 END
^Z
```

ARRAY.BAS: This BASIC computer program code graphically displays "selected" or "unselected" electrodes of a 5x5 electrode array based on a given threshold level.

```
1 ' This program graphically displays a 5x5 electrode array.  Electrodes          possessing
a normalized value greater than 70% of unity are filled          squares.  Otherwise, they
are outlined.
2 '
3 '
5 REM "NOTE: IF YOU WANT A HARDCOPY <SHFT-PRTSC> YOU MUST FIRST
                RUN GRAPHICS.COM from DOS."
6 '
7 '
8 '
10 CLS
20 INPUT "Normalized Data Filename?", INFILE$
25 INPUT "Threshold= ", VL
30 OPEN "I", #1, INFILE$
40 SCREEN 2
50 Y1=41
60 FOR ICOL=1 TO 5
70 X1=101
80 FOR IROW=1 TO 5
90 INPUT #1, IC, IR, V
100 X2=X1+24
110 Y2=Y1+10
120 IF V >=VL THEN LINE (X1,Y1)-(X2,Y2),,BF ELSE LINE (X1,Y1)-(X2,Y2),,B
130 X1=X1+48
140 NEXT IROW
150 Y1=Y1+20
160 NEXT ICOL
170 END
^Z
```
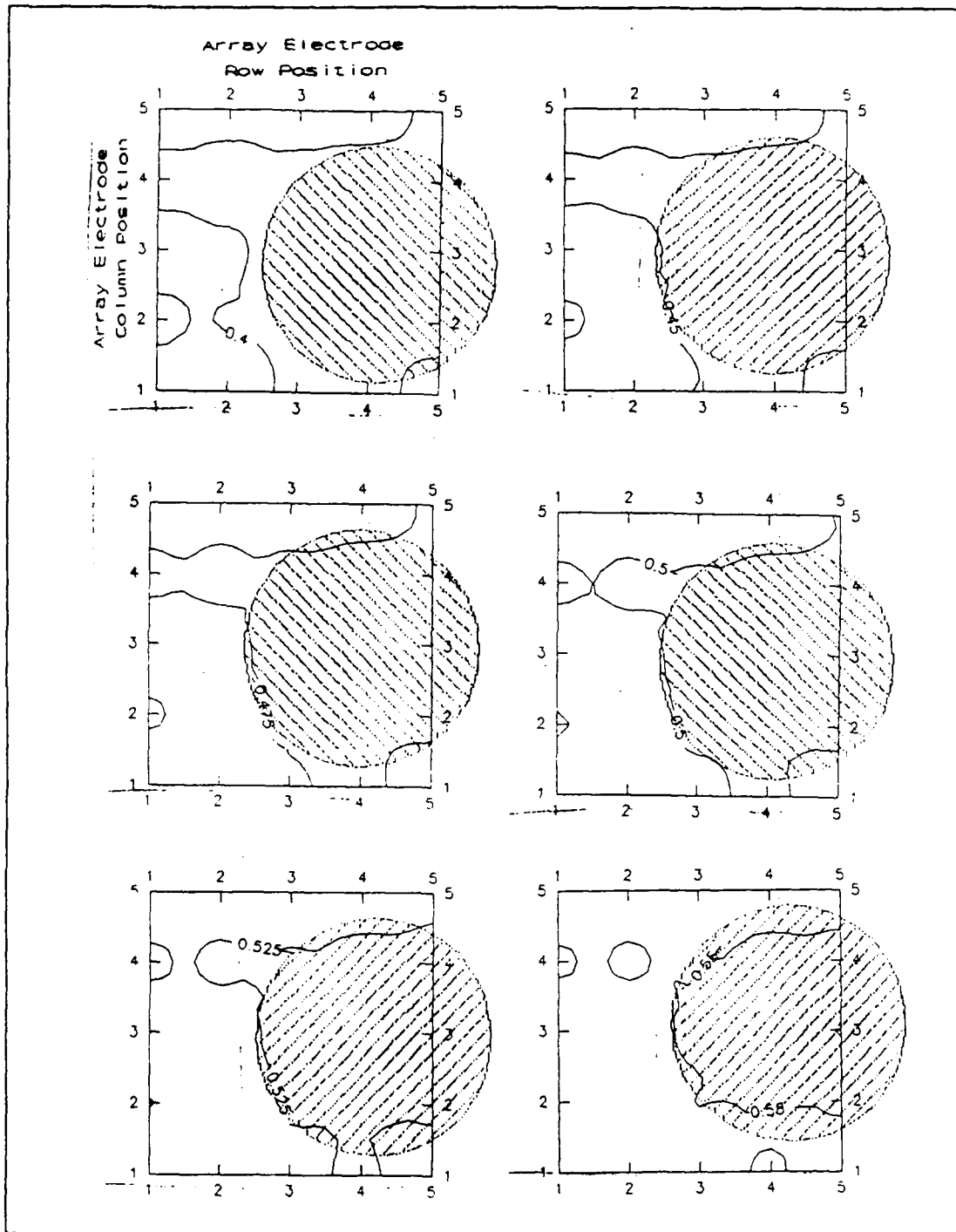
Figure F-1. Representative topographical slices for the 4 mm diameter, 45 g circular load (0.5 V is the selected slice).
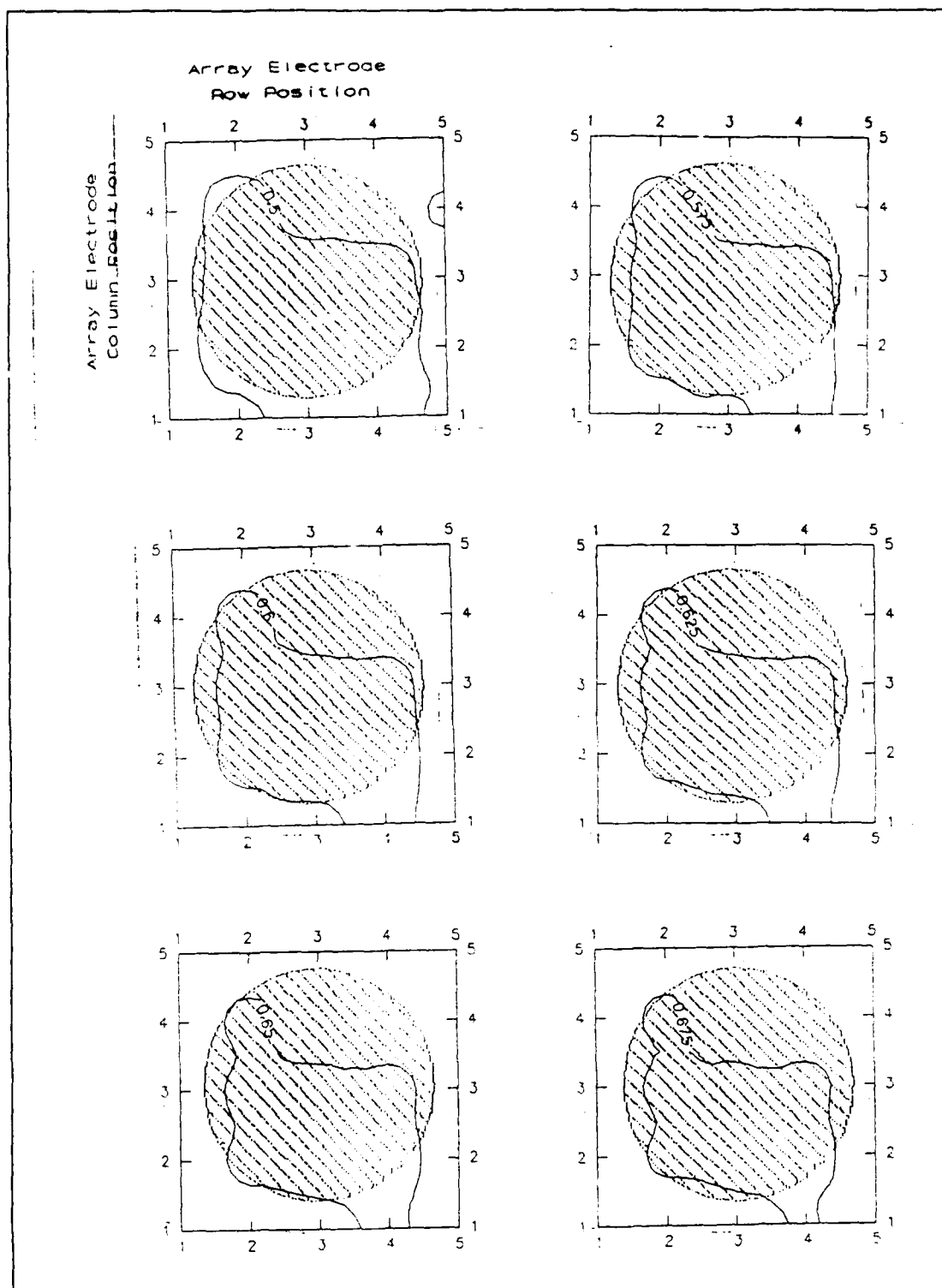
Figure F-2. Representative topographical slices for the 4 mm diameter, 100 g circular load (0.65 V is the selected slice).
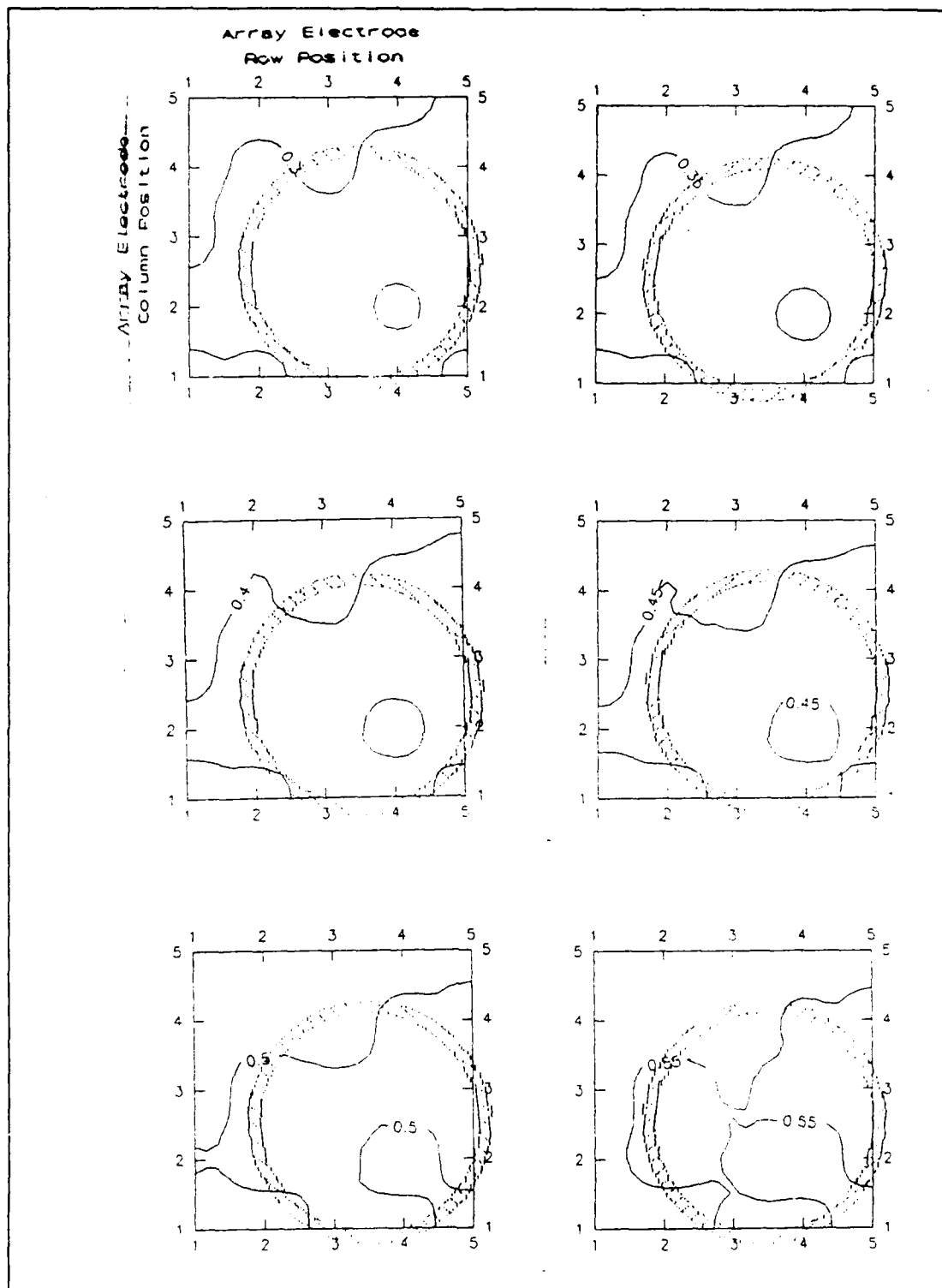
Figure F-3. Representative topographical slices for the
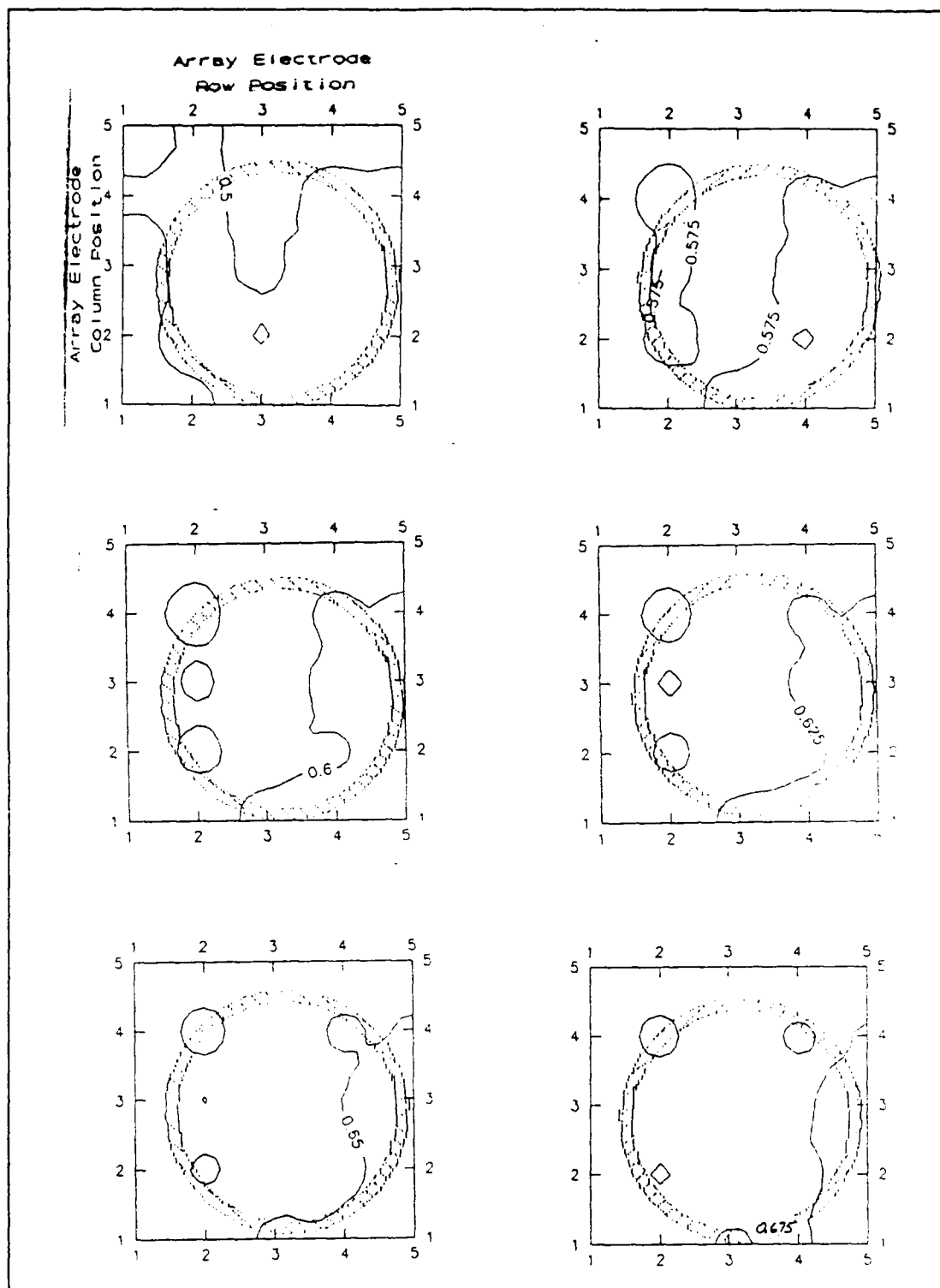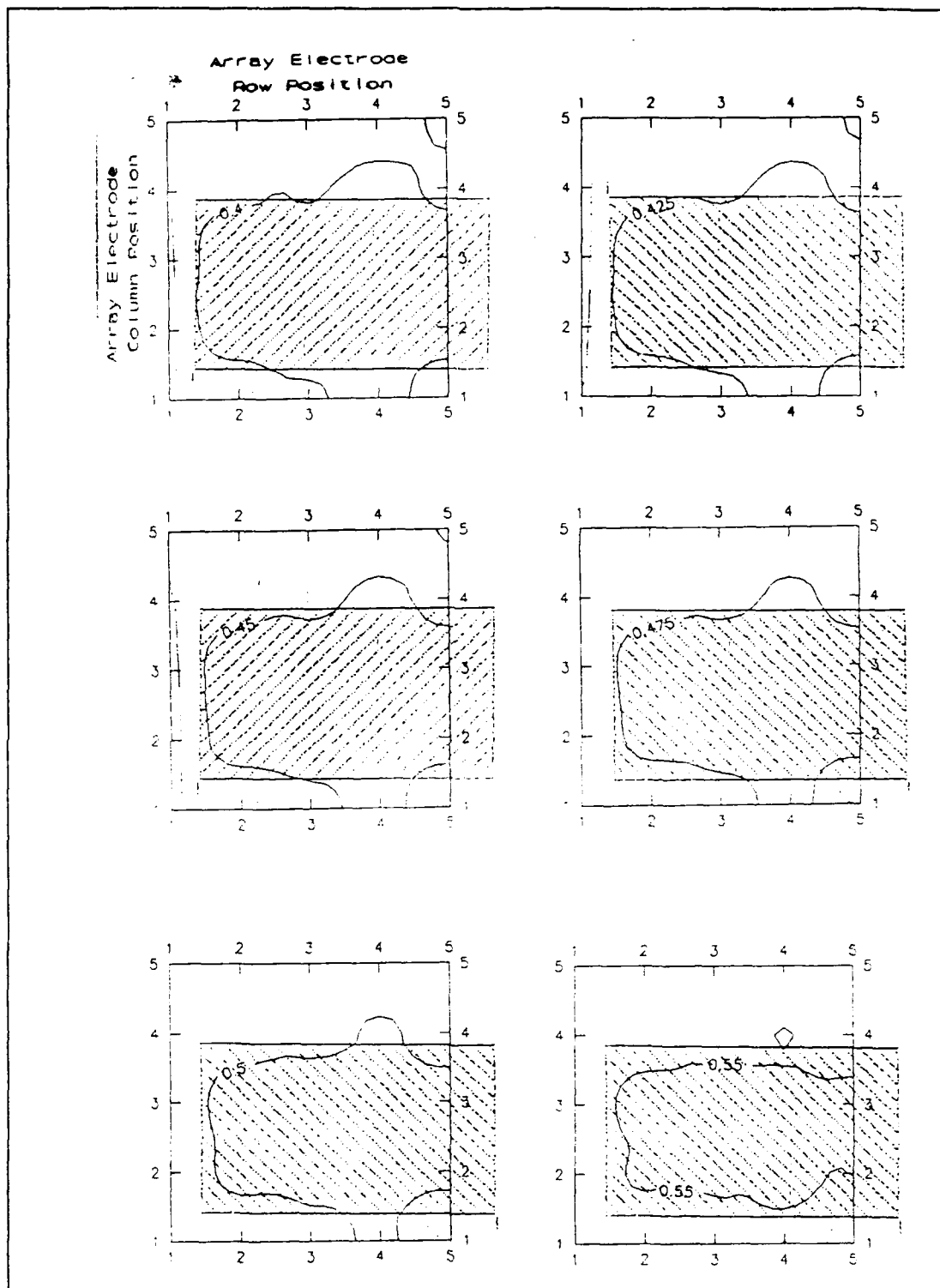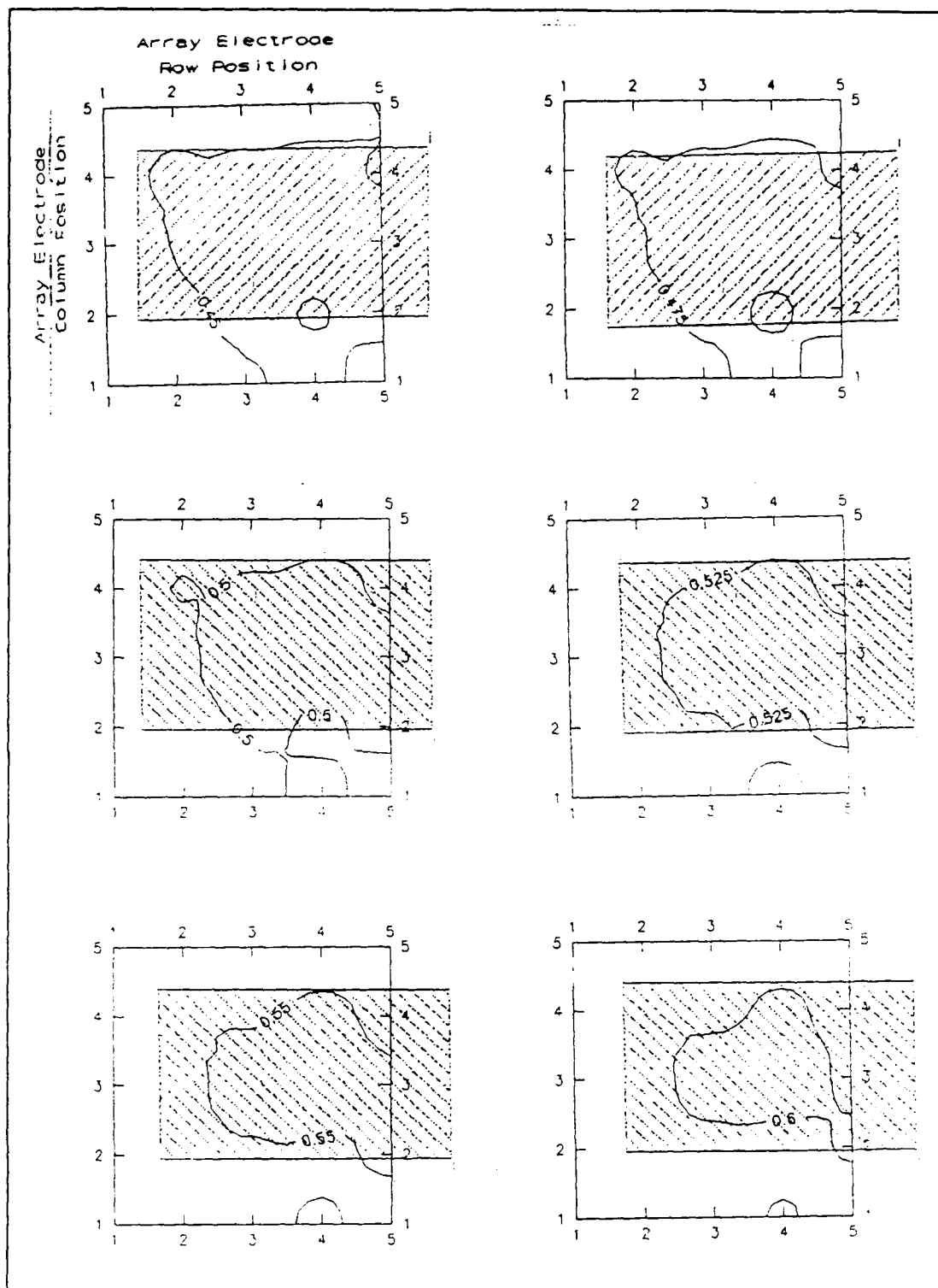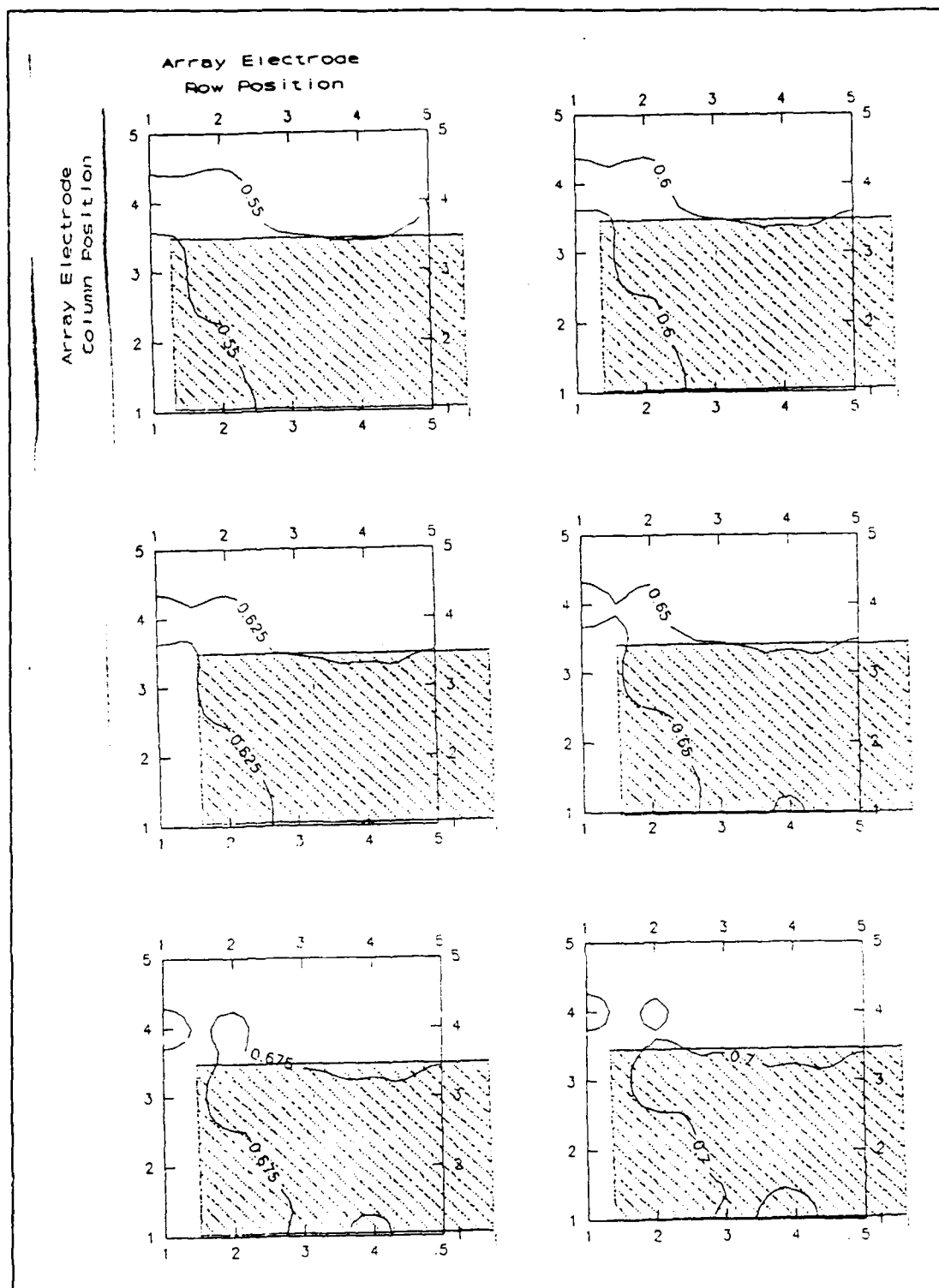4 mm diameter, 3 g toroidal load (0.5 V is the selected
slice).
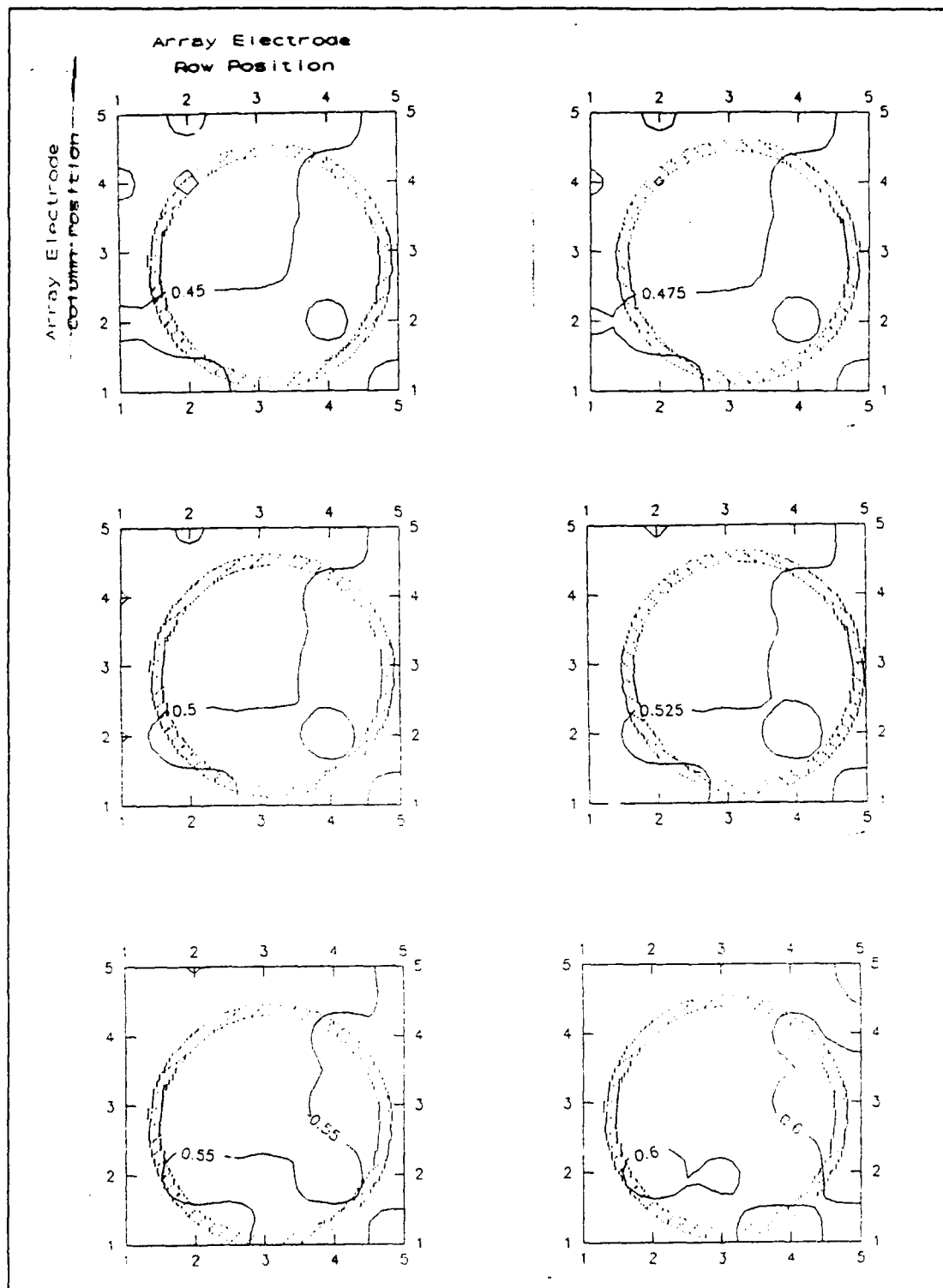
Figure F-4. Representative topographical slices for the 4 mm diameter, 45 g toroidal load (0.55 V is the selected slice).

Figure F-5. Representative topographical slices for the 4 mm diameter, 100 g toroidal load (0.625 V is the selected slice).

Figure F-6.   Representative topographical slices for the
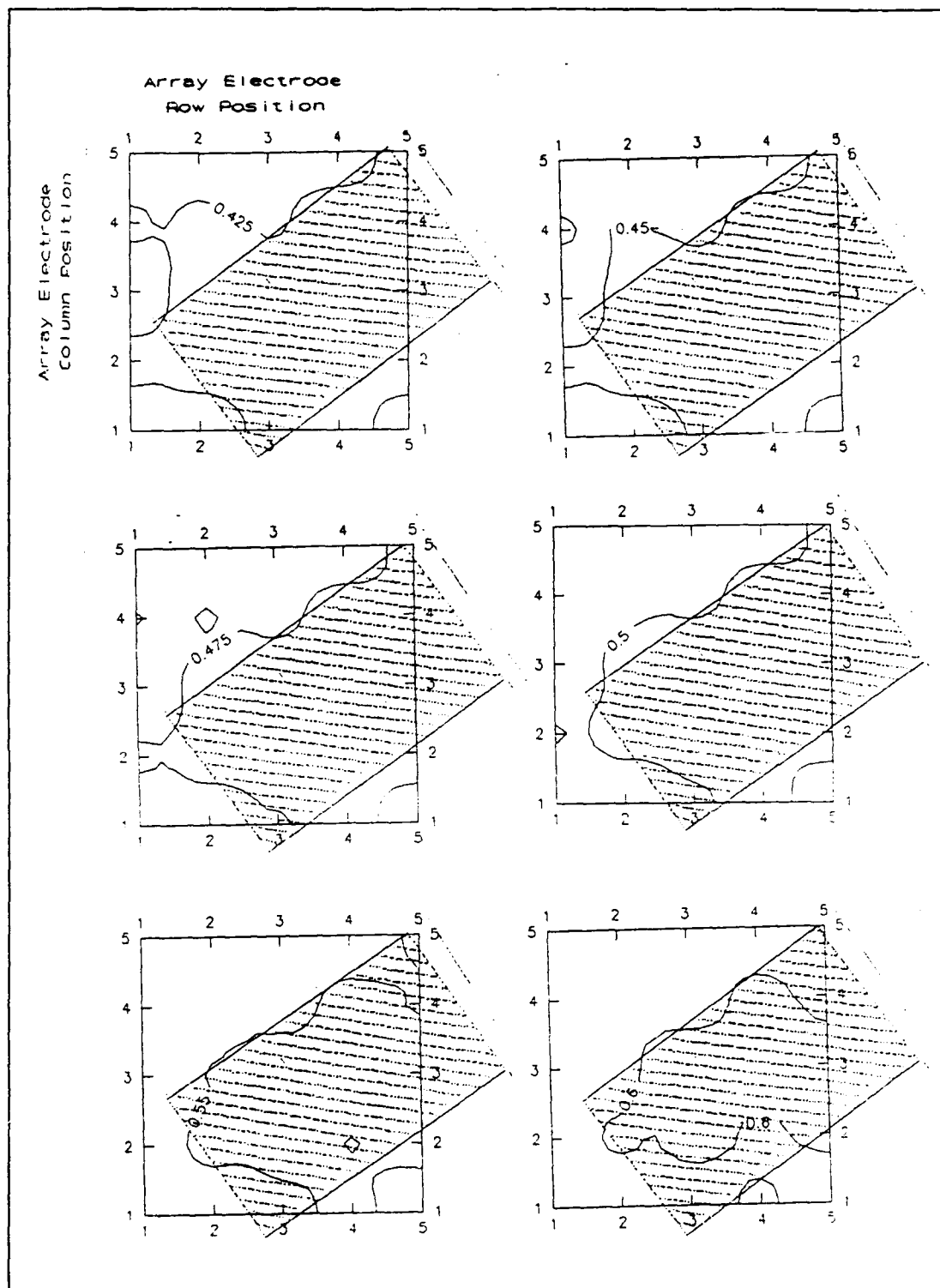5 mm x 3 mm, 3 g rectangular load (0.45 V is the selected
slice).

Figure F-7. Representative topographical slices for the 5 mm x 3 mm, 45 g rectangular load (0.5 V is the selected slice).

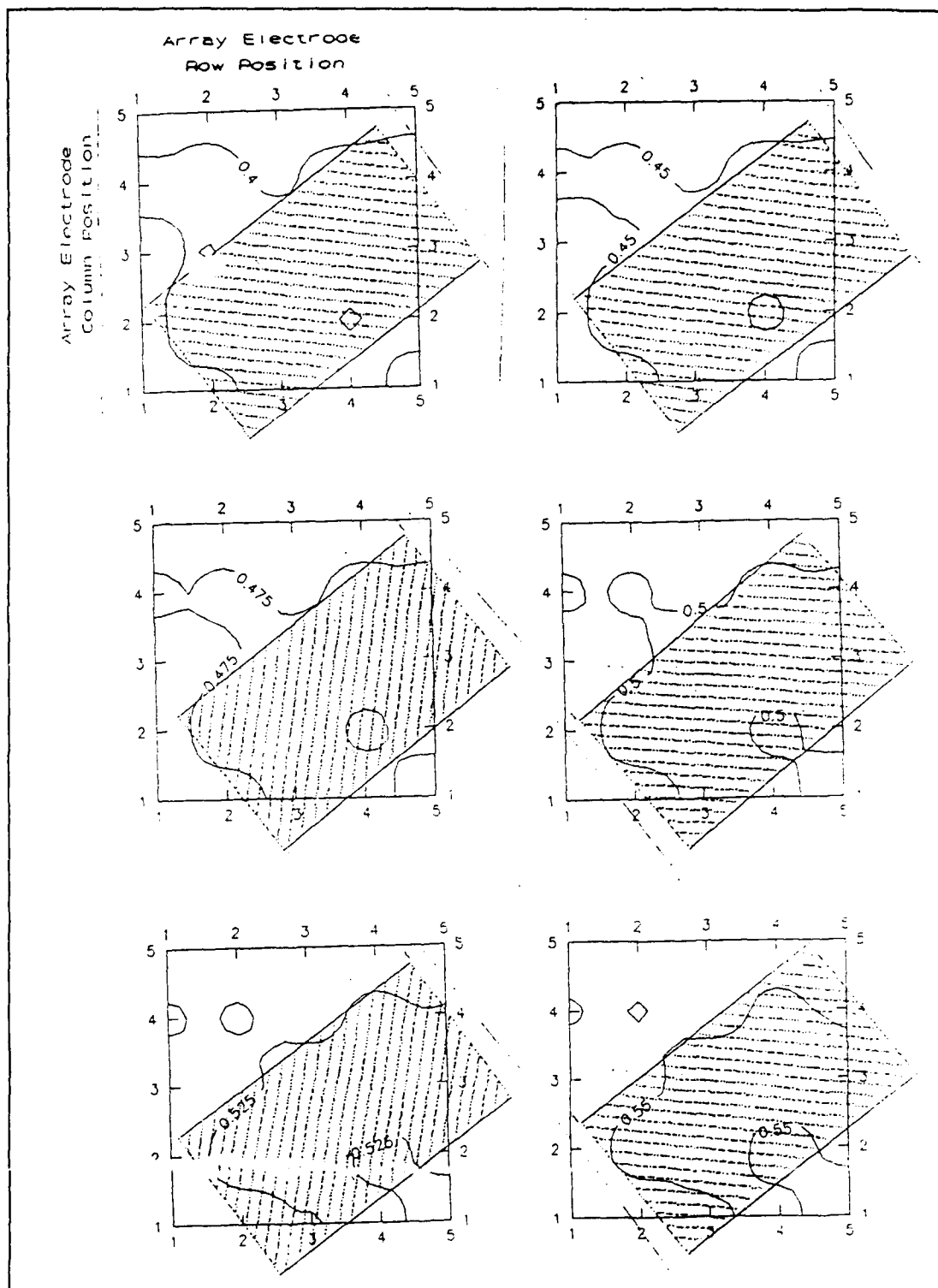Figure F-8. Representative topographical slices for the 5 mm x 3 mm, 100 g rectangular load (0.675 V is the selected slice).

Figure F-9. Representative topographical slices for the 5 mm x 3 mm, 3 g, angled rectangular load (0.55 V is the selected slice).

Figure F-10. Representative topographical slices for the 5 mm x 3 mm, 45 g, angled rectangular load (0.525 V is the selected slice).
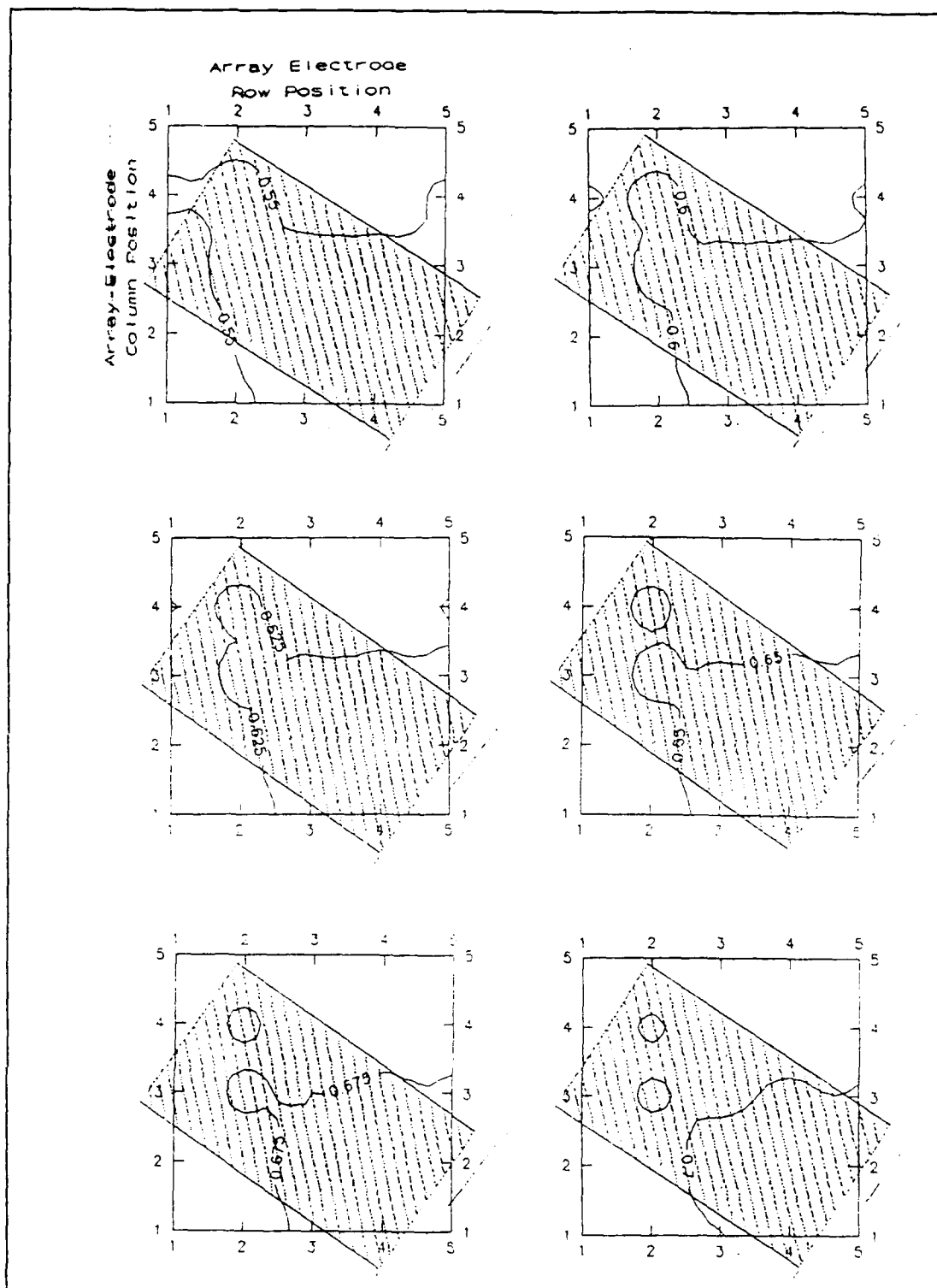
Figure F-11.   Representative topographical slices for the
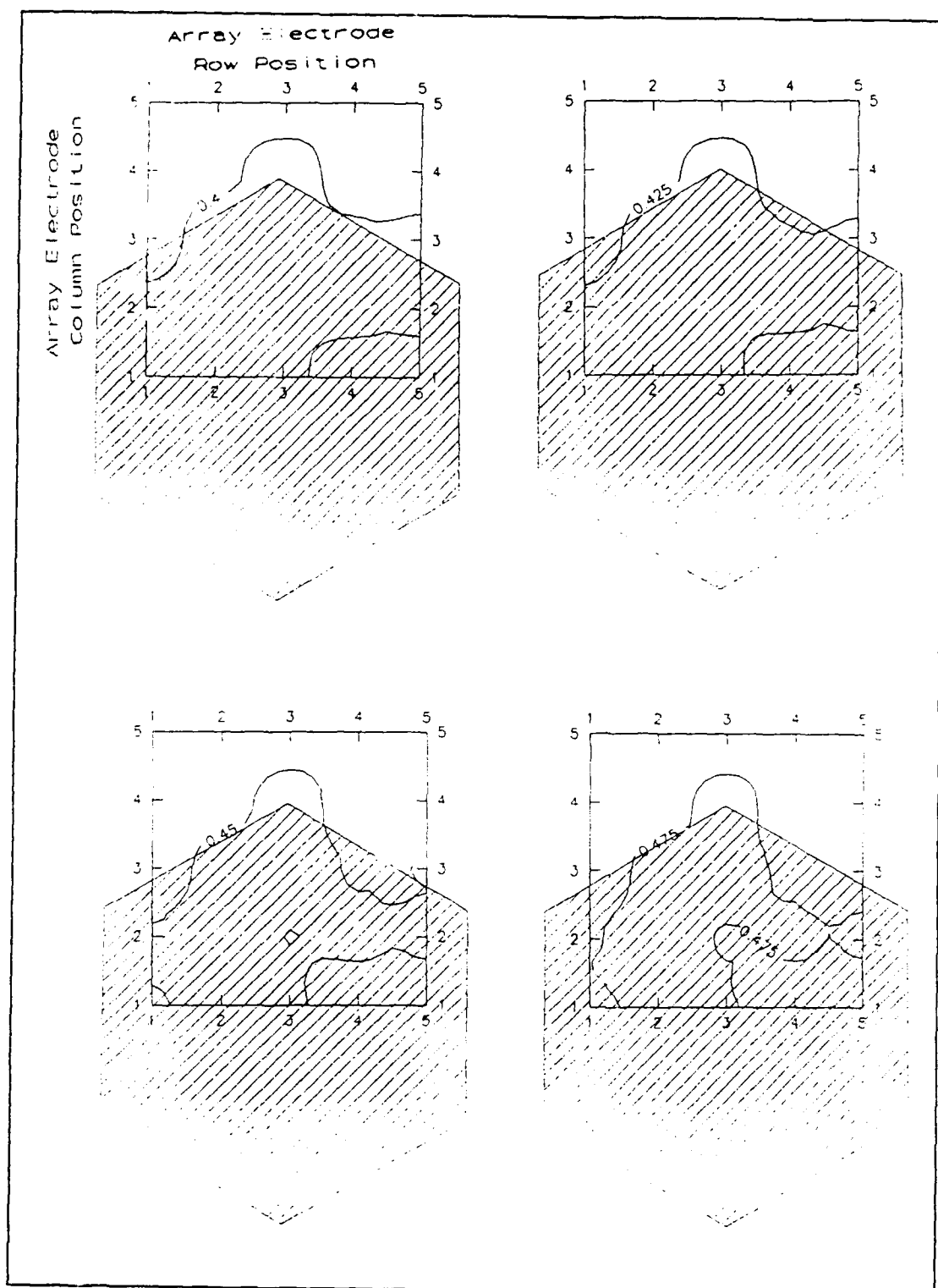5 mm x 3 mm, 100 g, angled rectangular load (0.625 V is the
selected slice).

Figure F-12. Representative topographical slices for the 3.175 mm (perimeter segment length), 3 g hexagonal load (0.425 V is the selected slice).
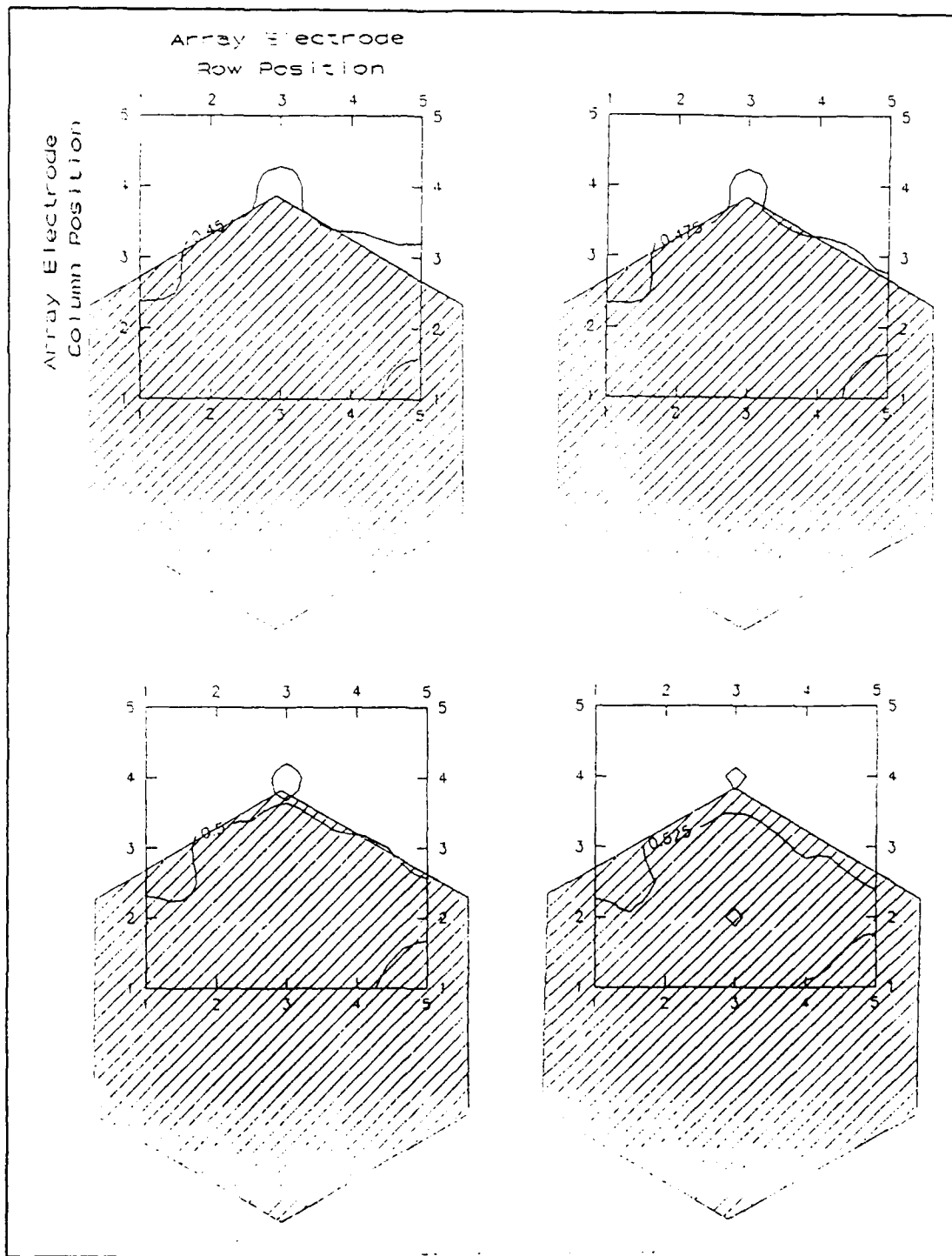
Figure F-13. Representative topographical slices for the
3.175 mm (perimeter segment length), 45 g hexagonal load
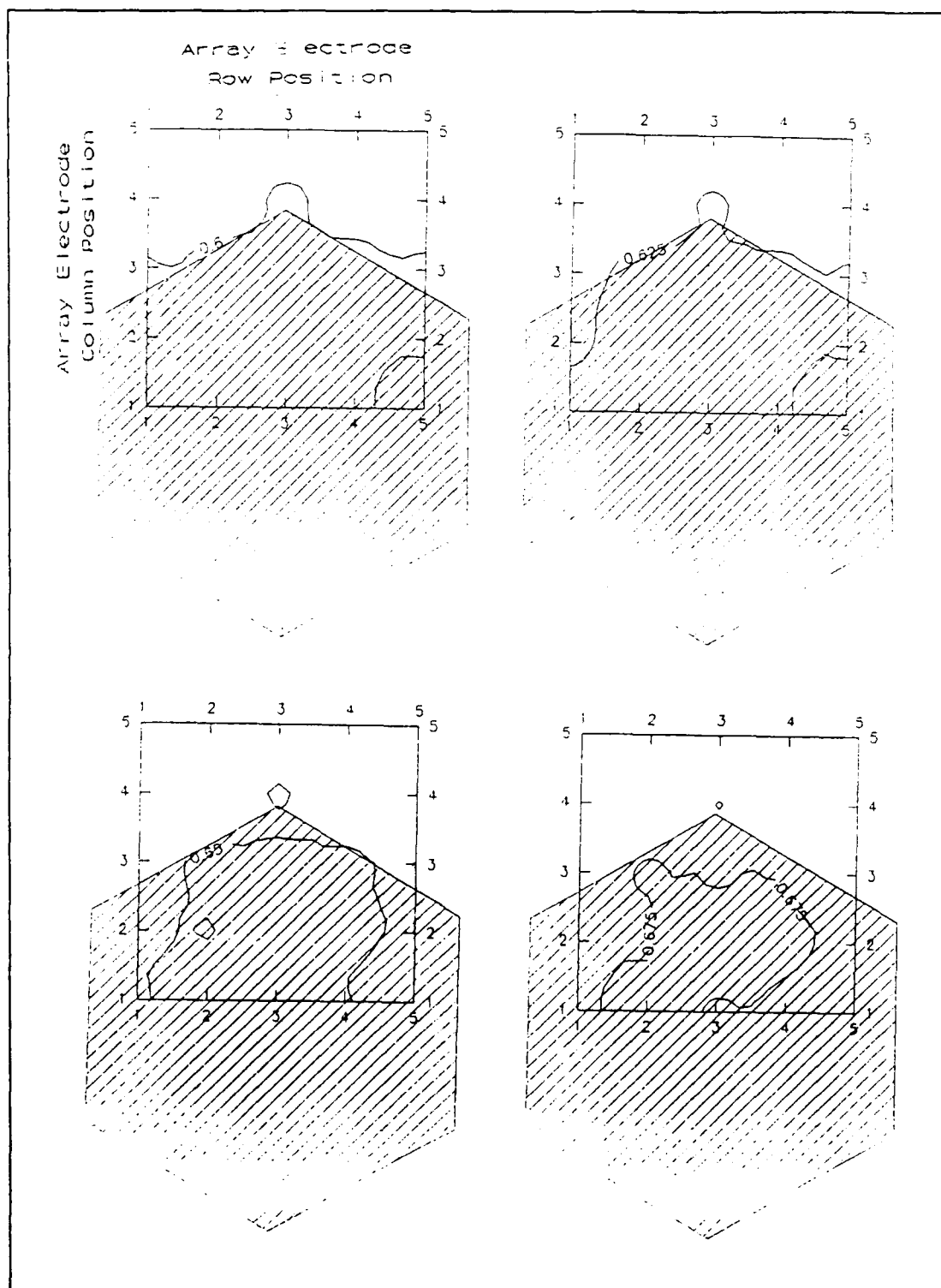(0.475 V is the selected slice).

Figure F-14. Representative topographical slices for the 3.175 mm (perimeter segment length), 100 g hexagonal load (0.625 V is the selected slice).
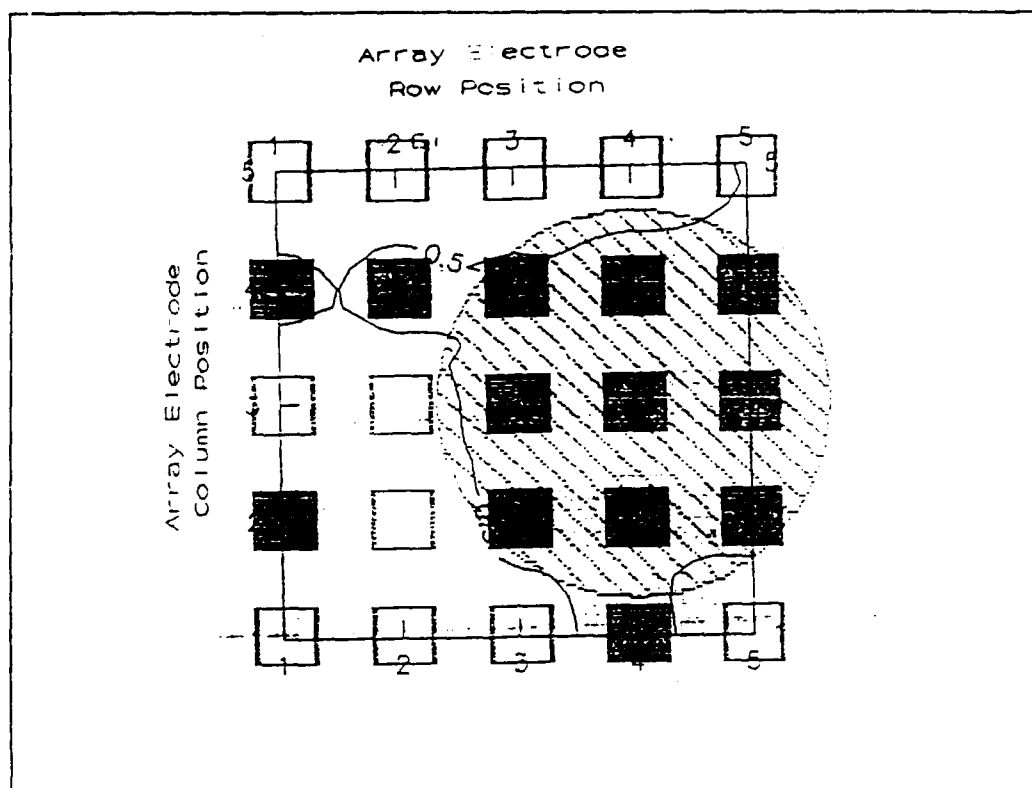
Figure F-15. Overlay of the selected array electrodes (black) and non-selected electrodes (white); the applied 4 mm diameter, 45 g circular load; and the selected topographical slice whose area best correlates with that of the applied load.
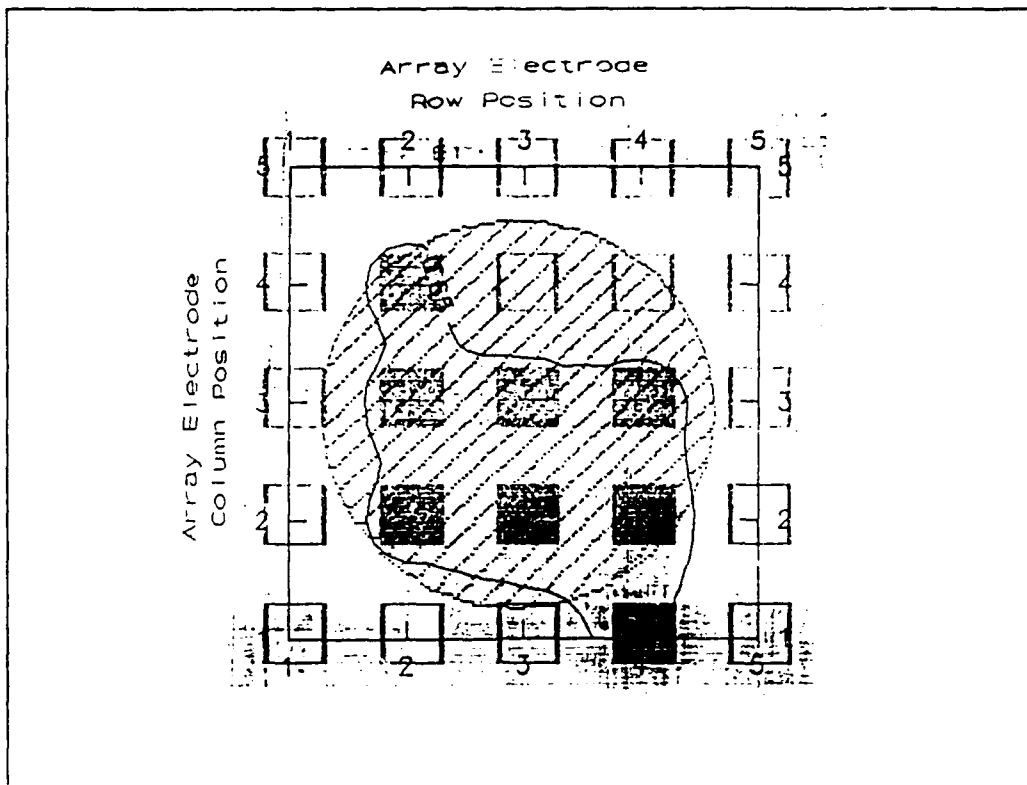
Figure F-16. Overlay of the selected array electrodes (black) and non-selected electrodes (white); the applied 4 mm diameter, 100 g circular load; and the selected topographical slice whose area best correlates with that of the applied load.
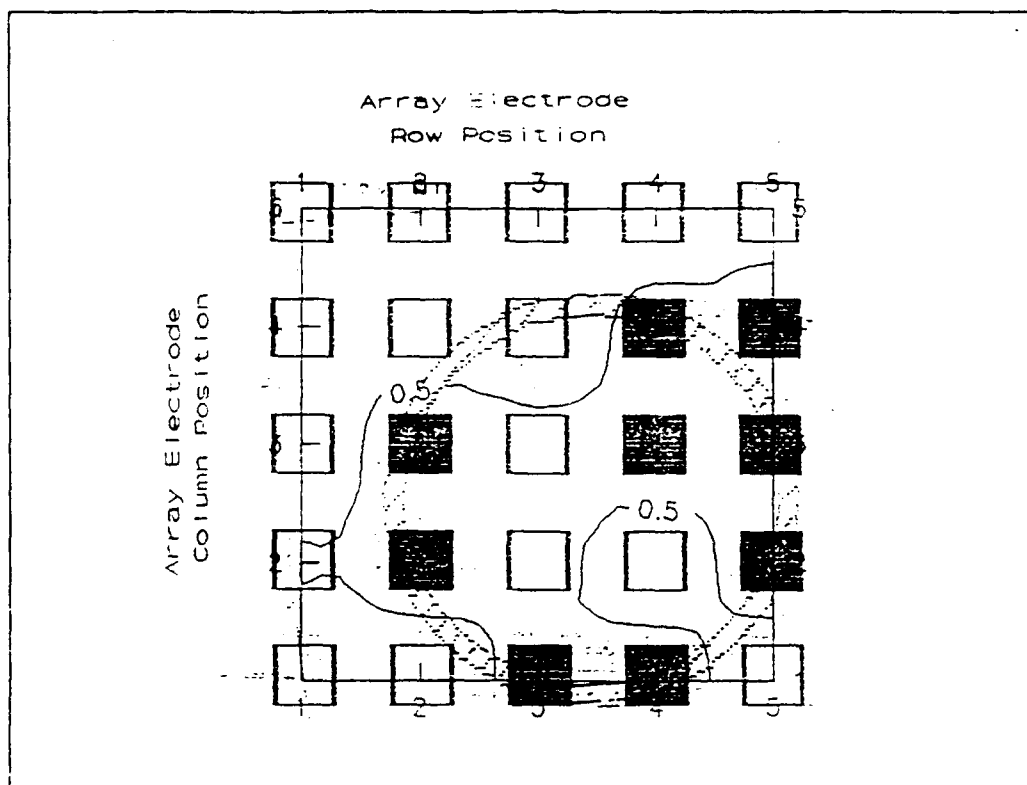
Figure F-17. Overlay of the selected array electrodes (black) and non-selected electrodes (white); the applied 4 mm diameter, 3 g toroidal load; and the selected topographical slice whose area best correlates with that of the applied load.

Figure F-18. Overlay of the selected array electrodes (black) and non-selected electrodes (white); the applied 4 mm diameter, 45 g toroidal load; and the selected topographical slice whose area best correlates with that of the applied load.

Figure F-19. Overlay of the selected array electrodes (black) and non-selected electrodes (white); the applied 4 mm diameter, 100 g toroidal load; and the selected topographical slice whos area best correlates with that of the applied load.
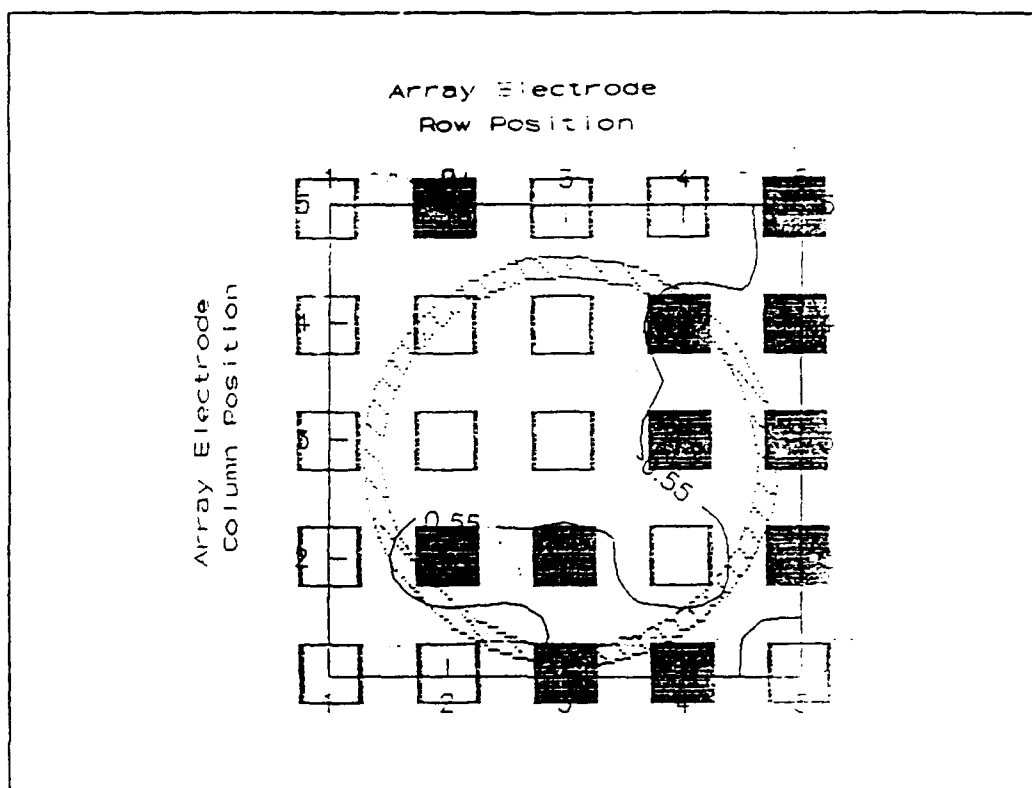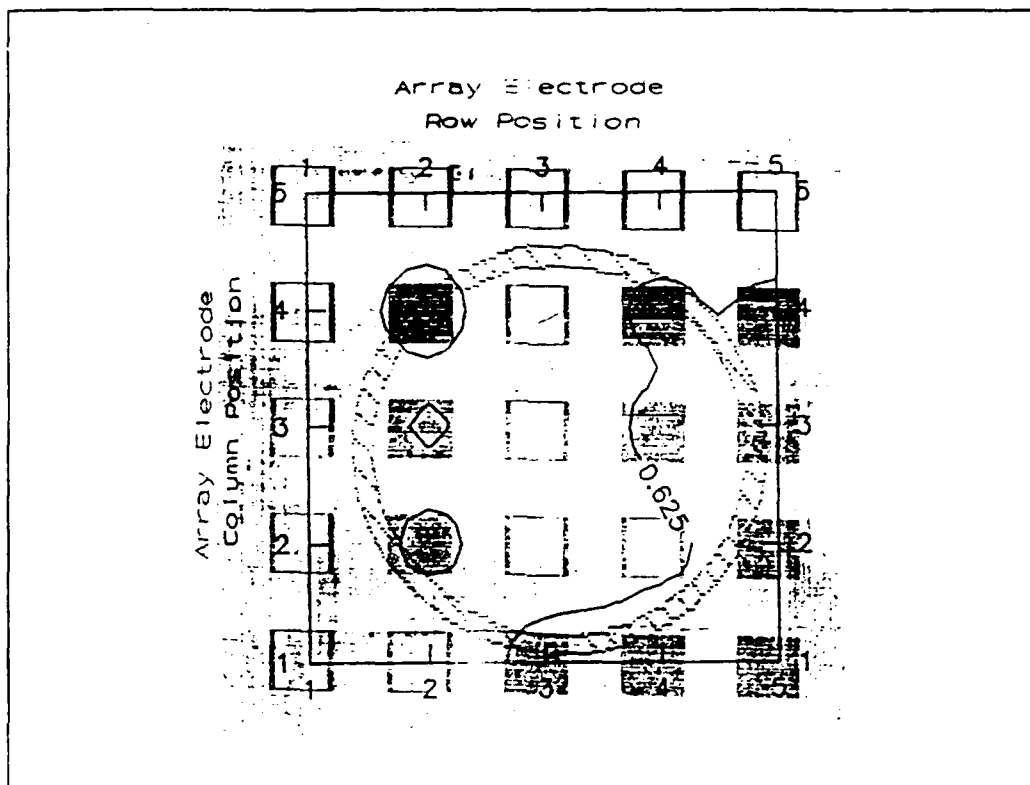
Figure F-20.   Overlay of the selected array electrodes (black) and non-selected electrodes (white); the applied 5 mm x 3 mm, 3 g rectangular load; and the selected topographical slice whose area best correlates with that of the applied load.

Figure F-21. Overlay of the selected array electrodes
(black) and non-selected electrodes (white); the applied
5 mm x 3 mm, 45 g rectangular load; and the selected
topographical slice whose area best correlates with that
of the applied load.

Figure F-22. Overlay of the selected array electrodes (black) and non-selected electrodes (white); the applied 5 mm x 3 mm, 100 g rectangular load; and the selected topographical slice whose area best correlates with that of the applied load.
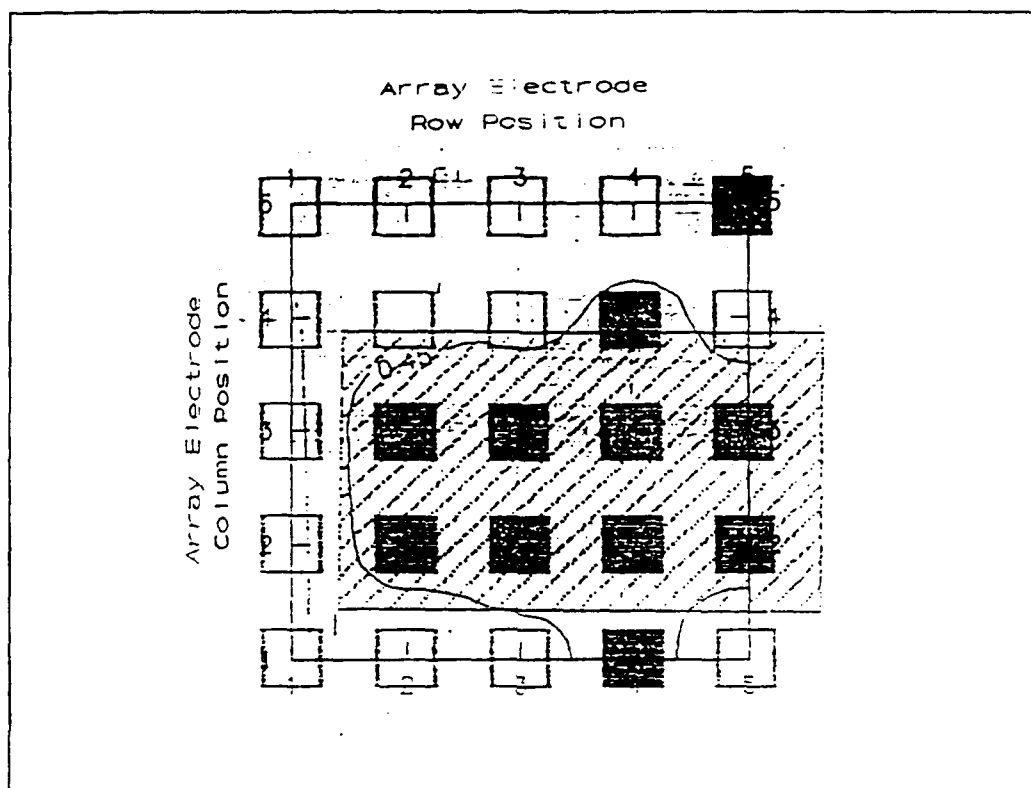
Figure F-23. Overlay of the selected array electrodes
(black) and non-selected electrodes (white); the applied
5 mm x 3 mm, 3 g angled rectangular load; and the
selected topographical slice whose area best correlates
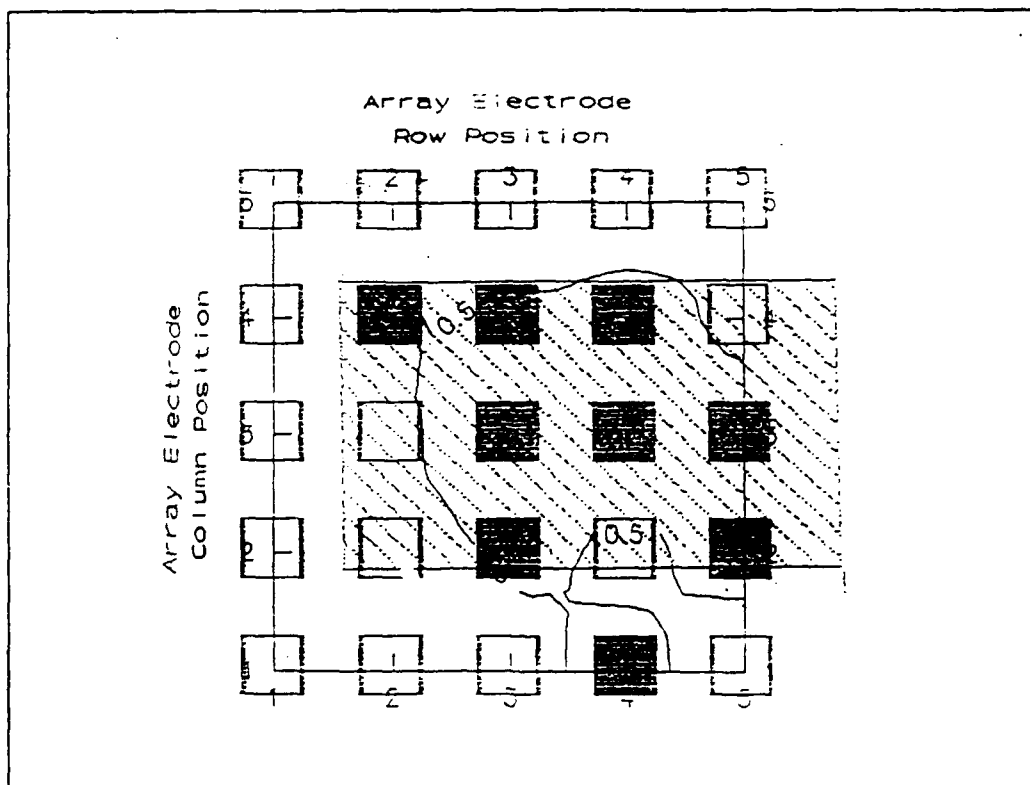with that of the applied load.

Figure F-24. Overlay of the selected array electrodes (black) and non-selected electrodes (white); the applied 5 mm x 3 mm, 45 g angled rectangular load; and the selected topographical slice whose area best correlates with that of the applied load.
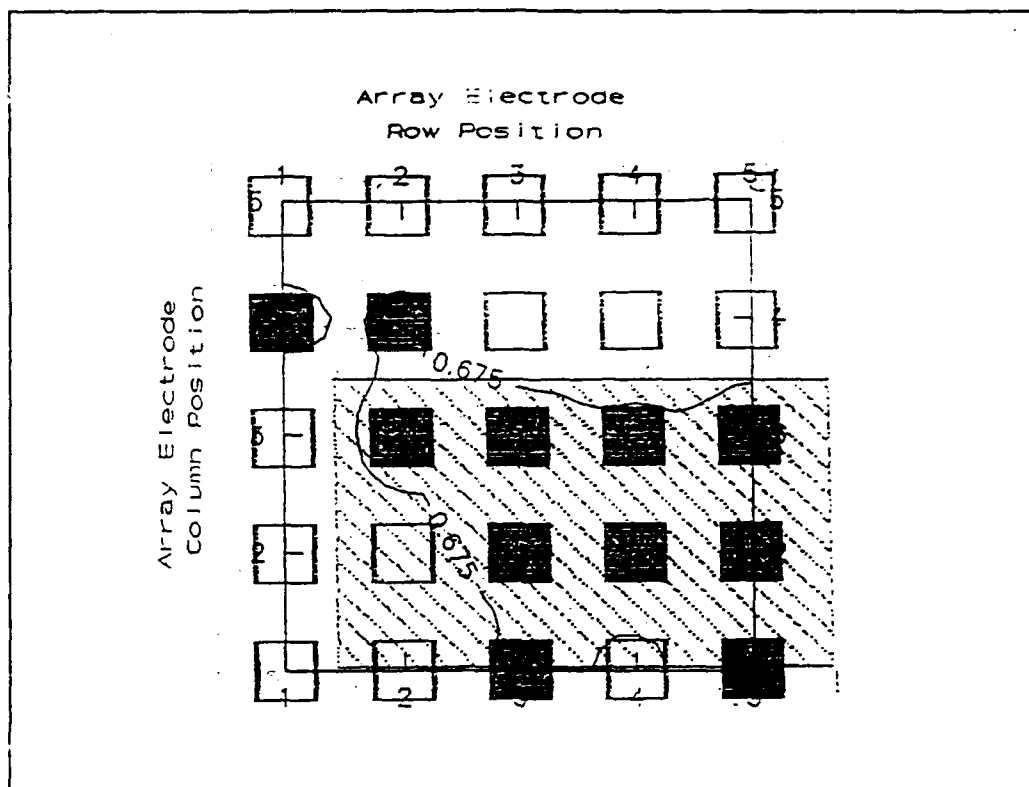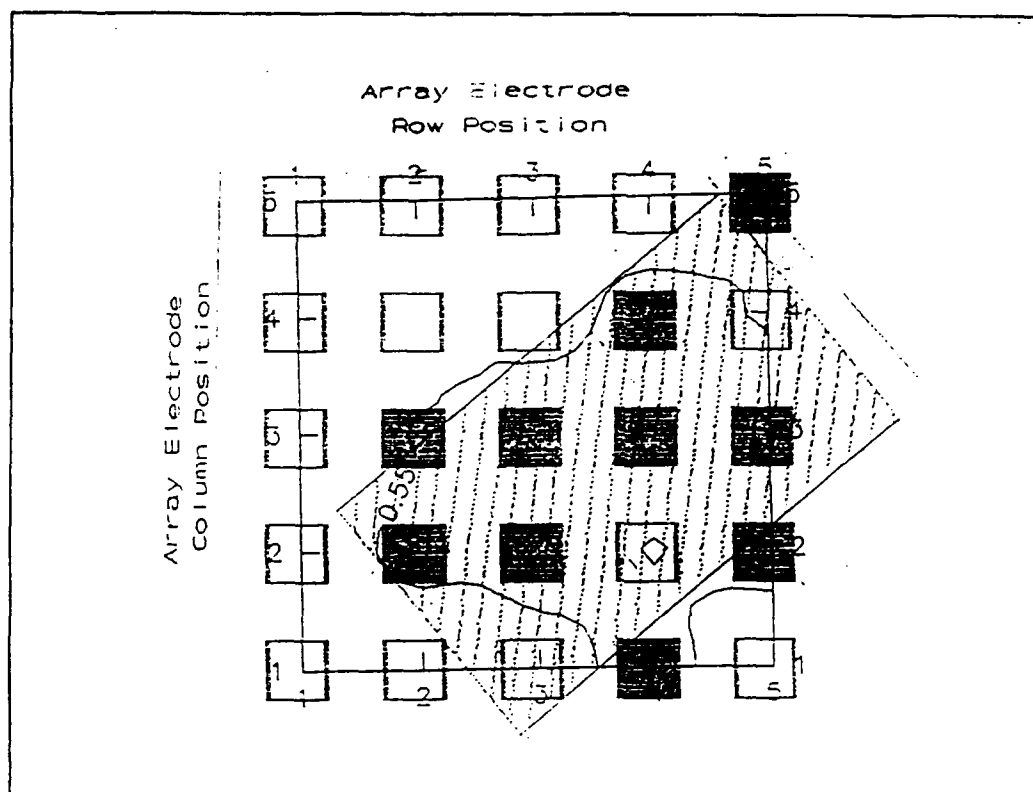
Figure F-25.   Overlay of the selected array electrodes
(black) and non-selected electrodes (white); the applied
5 mm x 3 mm, 100 g angled rectangular load; and the
selected topographical slice whose area best correlates
with that of the applied load.

Figure F-26. Overlay of the selected array electrodes (black) and non-selected electrodes (white); the applied 3.175 mm (perimeter segment length), 3 g hexagonal load; and the selected topographical slice whose area best correlates with the applied load.

Figure F-27. Overlay of the selected array electrodes (black) and non-selected electrodes (white); the applied 3.175 mm (perimeter segment length), 45 g hexagonal load; and the selected topographical slice whose area best correlates with the applied load.
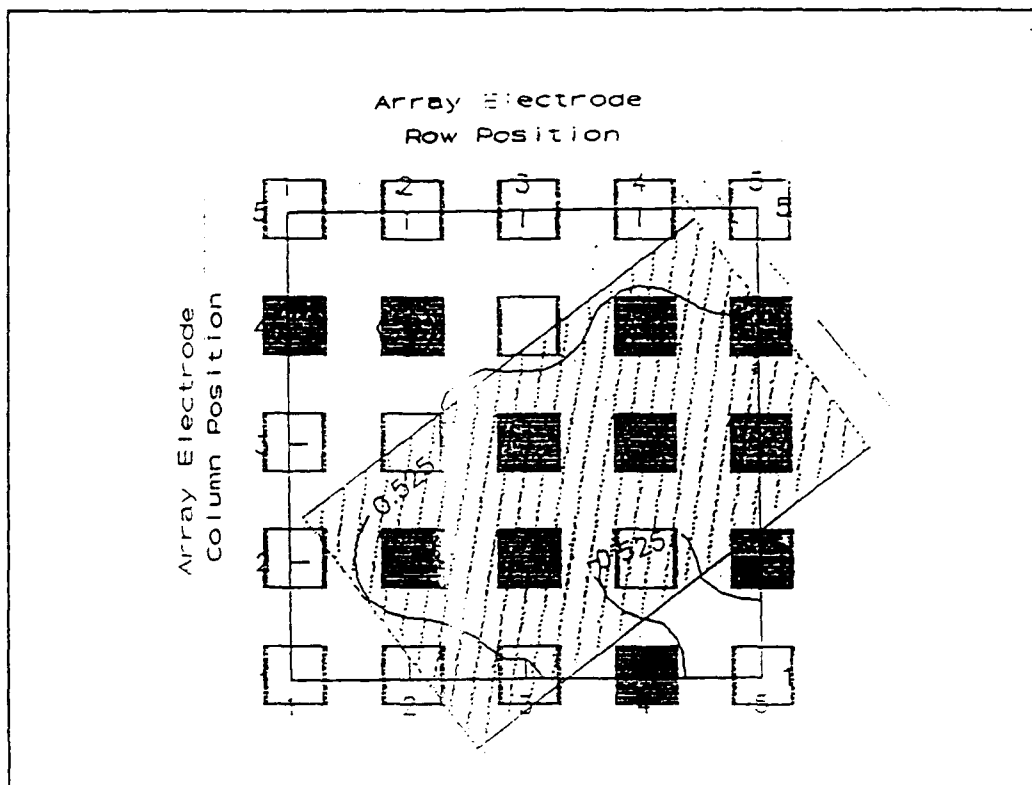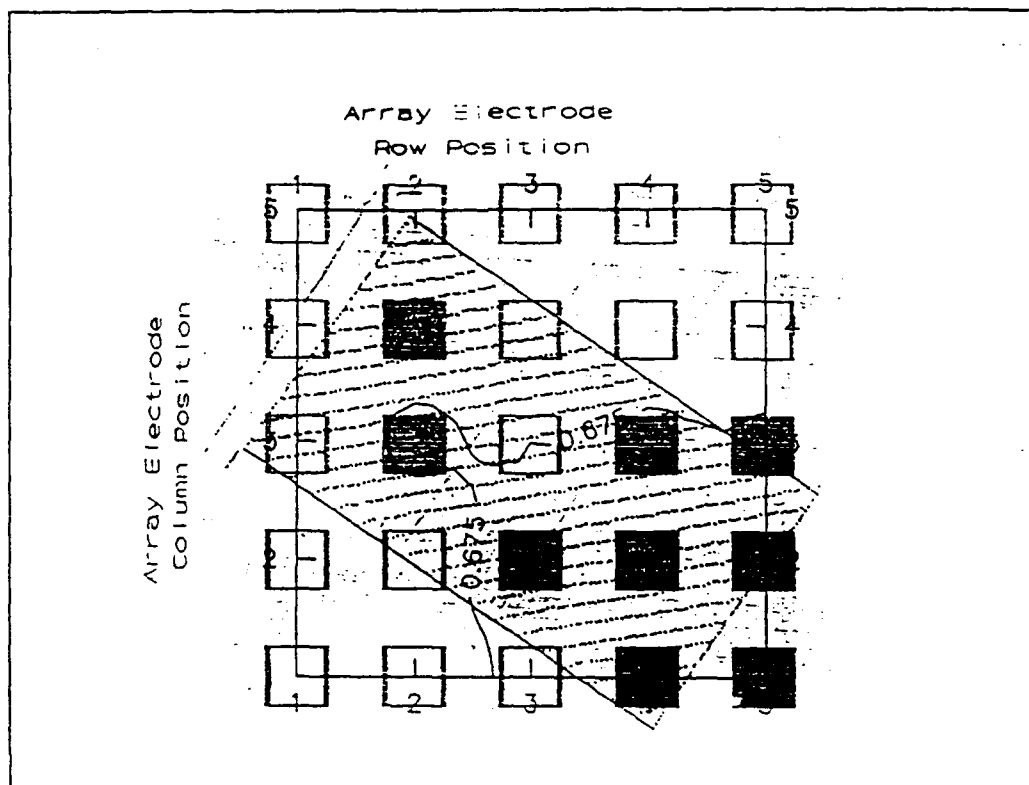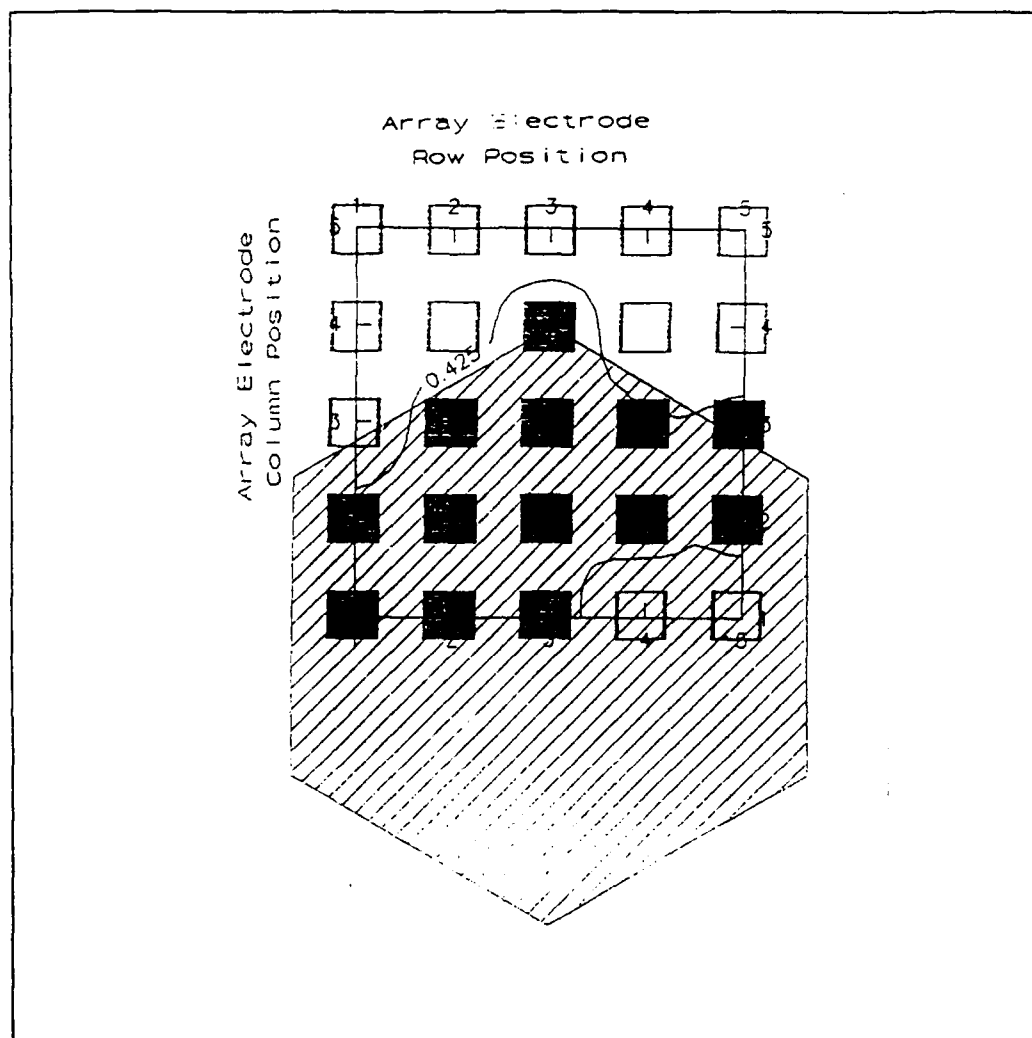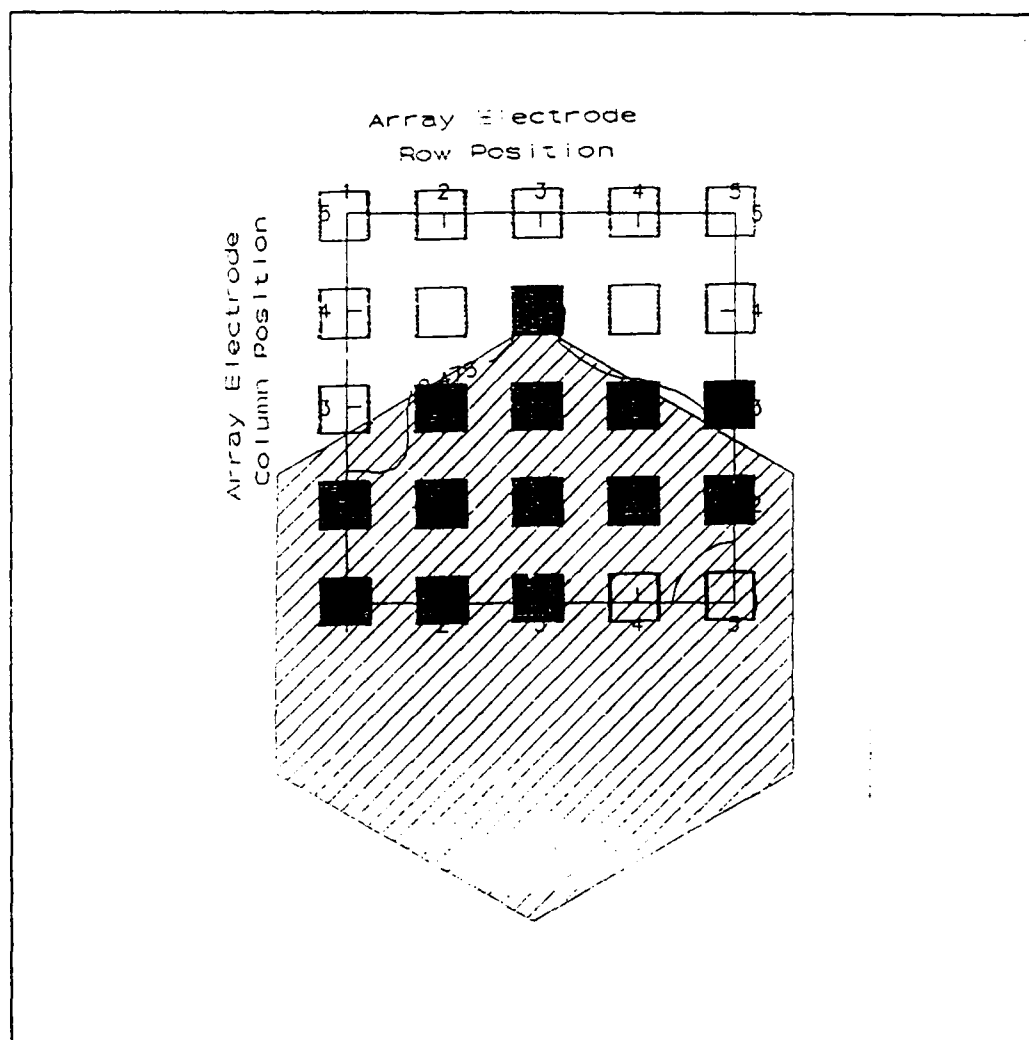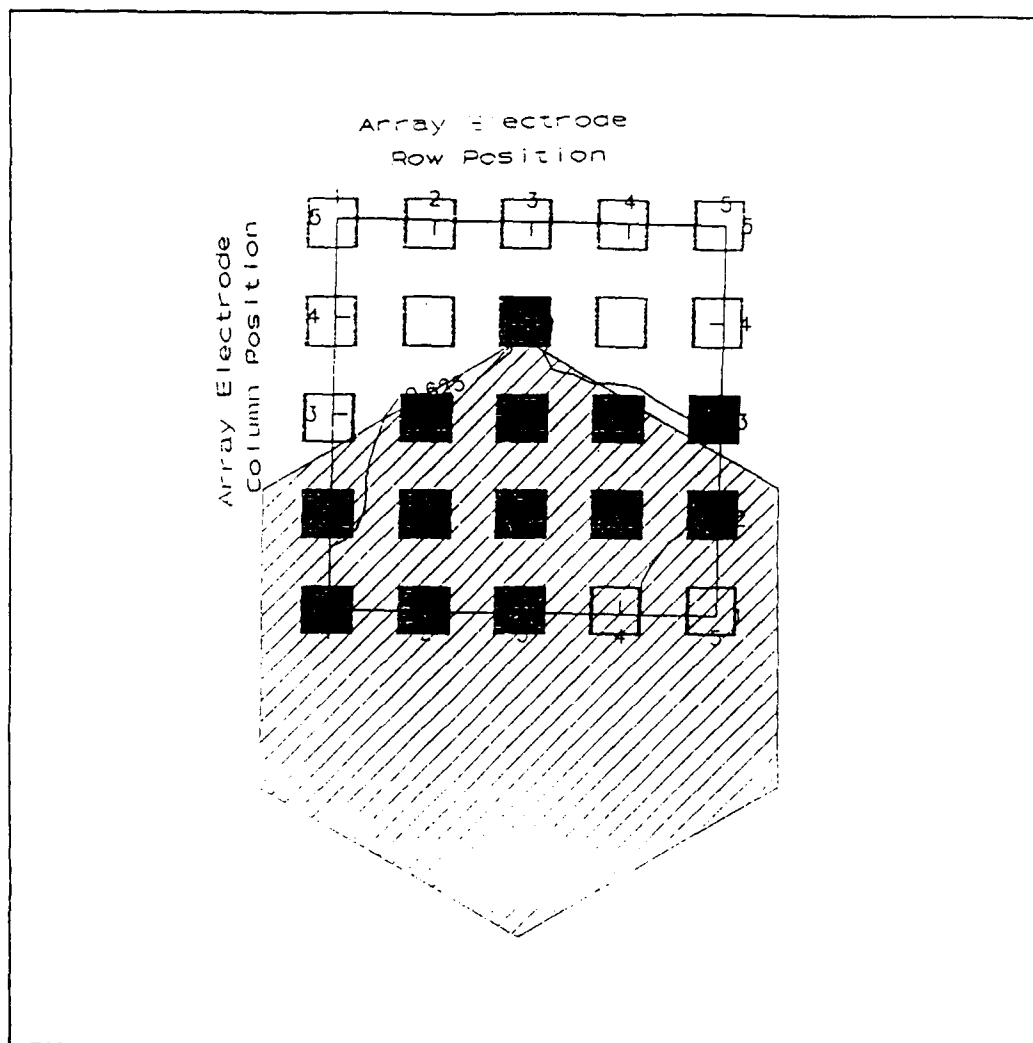
Figure F-28. Overlay of the selected array electrodes (black) and non-selected electrodes (white); the applied 3.175 mm (perimeter segment length), 100 g hexagonal load; and selected topographical slice whose area best correlates with the applied load.

BIBLIOGRAPHY

1. Pennywitt, Kirk E., "Robotic Tactile Sensing," Byte, 11:
    177-200, (January 1986).

2. Reston, Capt Rocky R., Robotic Tactile Sensor Fabricated
    From Piezoelectric Polyvinylidene Fluoride Films. M.S.
    Thesis, AFIT/GE/ENG/88D-41. School of Engineering, Air
    Force Institute of Technology (AU), Wright-Patterson AFB
    OH, December 1988.

3. Regtien, P.P.L. "Sensors for Applications in Robotics,"
    Sensors and Actuators, 10: Numbers 3 and 4, 195-218
    (November/December 1986).

4. Barth Phillip W. "Sensor Applications in Robotics,"
    Robotics Engineering, 8: 17-20 (September 1986).

5. Dario, Paolo, et al. "A Sensorised Scenario for
    Basic Investigation on Active Touch," Robot Sensors
    (Volume 2), Tactile and Non-Vision, edited by Alan Pugh.
    New York: IFS (Publications) Ltd, 1986.

6. Dario, Paolo and De Rossi, Danilo. "Tactile Sensors
    and the Gripping Challenge," IEEE Spectrum, 22: 46-52
    (August 1985).

7. Pennywitt, Kirk E. "Robotic Tactile Sensing,"
    Byte, 11: 177-200, (January 1986).

8. Park, Kyung, et al. "A PVDF Tactile Sensor for
    Industrial Robots," Conference Proceedings of
    Robotics, 10:4-47 to 4-72, April 1986.

9. Grahn, Allen R. and Astle, Lynn, "Robotic Ultrasonic
    Force Sensor Arrays," Conference Proceedings of Robot-
    ics, 8: 21-1 to 21-17, June 1984.

10. Pirolo, Capt David G. Piezoelectric Polymer Tactile
    Sensor Arrays for Robotics. MS thesis, AFIT/GE/ENG/
    87D-52. School of Engineering, Air Force Institute
    of Technology (AU), Wright-Patterson AFB OH,
    December 1987.

11. Cady, Walter G. Piezoelectricity, An Introduction to the
    Theory and Applications of Electromechanical Phenomena,
    Volumes I and II. New York: Dover Publications, Inc.,1964.

12. Bottom, Virgil E. Introduction to Quartz Crystal Unit
    Design, New York: Van Nostrand Reinhold Co., 1982.

13. Kraus, John D. Electromagnetics (Third Edition). New York: McGraw-Hill, 1984.

14. Herbert, J.M. Ferroelectric Transducers and Sensors, Volume I. New York: Gordon and Breach Science Publishers, 1982.

15. Sieppel, Robert G. Transducers, Sensors, and Detectors. Reston, Virginia. Reston Publishing Company, 1983.

16. Kynar Piezo Film Sales Department. Piezoelectric Plastic Promise New Sensors. Machine Design (Reprinted from October 23, 1986). Pennwalt Company. Philadelphia, PA.

17. KYNAR Piezo Film Department. Kynar Piezo Film Technical Manual. Manual 10-M-11-83-M. Pennwalt Corporation, King of Prussia PA, 1983.

18. Weste, Neil and Kamran Eshraghian. Principles of CMOS VLSI Design A Systems Perspective. Reading MA: Addison-Wesley Publishing Company, 1985.

19. Ousterhout, John K. "Magic: A VLSI Layout Editor," in 1986 Berkeley CAD Tools Users Manual. Berkeley (1986).

20. University of Southern California. MOSIS Users Manual. (1988).

Vita

Captain Douglas G. Ford ██████████████████ ████████████ ████████████████████████████ in Lake City, Michigan in 1972, ████ entered the USAF in October of that year. He worked as an avionics technician, attaining the rank of Staff Sergeant before being selected for the Airman Education and Commissioning Program in 1980. Following graduation in 1983, with a Bachelor of Science in Electrical Engineering from the University of New Mexico, he obtained his commission through Officer Training School. Upon graduation, he was assigned to the Air Force Weapons Laboratory, Kirtland AFB, New Mexico. From 1983 to 1987, he served as a high energy laser instrumentation engineer. From 1987 to 1988, he served as the test director for high power microwave effects and vulnerability testing. In May 1988, he entered the School of Engineering, Air Force Institute of Technology.

██████████████   ████████████████
                  ████████████████

REPORT DOCUMENTATION PAGE		Form Approved OMB No. 0704-0188

1a. REPORT SECURITY CLASSIFICATION	1b. RESTRICTIVE MARKINGS

2a. SECURITY CLASSIFICATION AUTHORITY	3. DISTRIBUTION / AVAILABILITY OF REPORT
2b. DECLASSIFICATION / DOWNGRADING SCHEDULE	Approved for Public Release; Distribution Unlimited

4. PERFORMING ORGANIZATION REPORT NUMBER(S)	5. MONITORING ORGANIZATION REPORT NUMBER(S)
AFIT/GE/ENG/89D-13	

6a. NAME OF PERFORMING ORGANIZATION	6b. OFFICE SYMBOL (If applicable)	7a. NAME OF MONITORING ORGANIZATION
School of Engineering	AFIT/ENG	

6c. ADDRESS (City, State, and ZIP Code)	7b. ADDRESS (City, State, and ZIP Code)
Air Force Institute of Technology Wright-Patterson AFB OH 45433-6583	

8a. NAME OF FUNDING / SPONSORING ORGANIZATION	8b. OFFICE SYMBOL (If applicable)	9. PROCUREMENT INSTRUMENT IDENTIFICATION NUMBER
AAMRL	CC	

9c. ADDRESS (City, State, and ZIP Code)	10. SOURCE OF FUNDING NUMBERS			
	PROGRAM ELEMENT NO.	PROJECT NO.	TASK NO	WORK UNIT ACCESSION NO
Wright-Patterson AFB OH 45433-6583				

11. TITLE (Include Security Classification)

See Box 19

12. PERSONAL AUTHOR(S)
Douglas G. Ford, B.S.E.E., Captain, USAF

13a. TYPE OF REPORT	13b. TIME COVERED	14. DATE OF REPORT (Year, Month, Day)	15. PAGE COUNT
MS Thesis	FROM _____ TO _____	1989 December	178

16. SUPPLEMENTARY NOTATION

17. COSATI CODES			18. SUBJECT TERMS (Continue on reverse if necessary and identify by block number)
FIELD	GROUP	SUB-GROUP	Piezoelectric Materials Tactile Sensing
09	01		Piezoelectric Transducers Robotic Sensors

19. ABSTRACT (Continue on reverse if necessary and identify by block number)

Thesis Advisor: Edward S. Kolesar
Associate Professor
Department of Electrical and Computer Engineering

Title: MULTIPLEXED ROBOTIC TACTILE SENSOR FABRICATED
FROM POLYVINYLIDENE FLUORIDE FILM   (Unclassified)

20. DISTRIBUTION / AVAILABILITY OF ABSTRACT	21. ABSTRACT SECURITY CLASSIFICATION
☐ UNCLASSIFIED/UNLIMITED ☒ SAME AS RPT. ☐ DTIC USERS	Unclassified

22a. NAME OF RESPONSIBLE INDIVIDUAL	22b. TELEPHONE (Include Area Code)	22c. OFFICE SYMBOL
Edward S. Kolesar, Associate Professor	(513) 255-3576	AFIT/ENG

DD Form 1473, JUN 86   Previous editions are obsolete.   SECURITY CLASSIFICATION OF THIS PAGE

Abstract

This research effort involved the design, fabrication and evaluation of a multiplexed robotic tactile sensor fabricated from polyvinylidene fluoride (PVDF) film. A 16x16 electrode array was designed, each electrode encompassing a 250 μm x 250 μm square area, separated by a distance of 150 μm. A resident analog multiplexer was designed to assist in the acquisition of electrical signals from the array. Inherent within the multiplexer were analog transmission gates which provided a bidirectional flow of charge to each electrode. This provided a means of initializing the bias state of the PVDF film prior to the application of a load.

Fundamental difficulties associated with coupling the PVDF film to the electrode array (and the analog transmission gates) prevented the successful fabrication of a functioning tactile sensor. A previously designed 5x5 electrode array sensor was modified with external TTL multiplexing circuitry. Characterization of the IC, configured with a 25 μm thick PVDF film, was accomplished using a circle, toroid, rectangle, and a hexagon over the load range of 3 g to 100 g. Final results included the development of an elementary pattern recognition algorithm. Recommendations for solving the obstacles faced in this research effort are discussed in the final chapter.